論文 / 著書情報
Article / Book Information

題目(和文)	
Title(English)	Two-dimensional near-surface soil profiling using time domain waveform inversion.
著者(和文)	AMROUCHEMOHAMED
Author(English)	MOHAMED AMROUCHE
出典(和文)	学位:博士(学術), 学位授与機関:東京工業大学, 報告番号:甲第10047号, 授与年月日:2016年1月31日, 学位の種別:課程博士, 審査員:山中　浩明,田村　哲郎,翠川　三郎,盛川　仁,海江田　秀志
Citation(English)	Degree:Doctor (Academic), Conferring organization: Tokyo Institute of Technology, Report number:甲第10047号, Conferred date:2016/1/31, Degree Type:Course doctor, Examiner:,,,,
学位種別(和文)	博士論文
Type(English)	Doctoral Thesis

Two-dimensional near-surface soil profiling using time domain waveform inversion.

Thesis written by:
Amrouche Mohamed

Supervised by:
Pr. Yamanaka Hiroaki

Departement of Environmental Science and Technology
Tokyo Institute of Technology

2015

Contents

THESIS SUMMARY

Near surface characterization start to gain huge importance from exploration geophysicists and many methods are being proposed to retrieve the 2D structures of shallow soils. Since most of these methods are based on the modal inversion of the surface-waves, they can only be applicable to laterally homogeneous or smoothly heterogeneous soil models. We are proposing a time domain waveform inversion for 2D near-surface exploration, which can offer an alternative approach to the existing surface-wave techniques for layered soils. Our method directly fits the input Rayleigh waveforms to retrieve the 2D soil structure without the need of any modal identification, allowing the inversion of soil models that can be challenging with the modal inversion based approaches. In our method, the forward problem formulated in the time domain is based on a 2.5D staggered finite difference scheme to simulate the P-SV wave field; soil modeling is achieved by dividing soil layers into specific number of blocks with discontinuous interfaces. A source deconvolution by a reference station was applied to both observed and calculated waveforms to make a waveform inversion free of the source signature. Numerical experiments showed that our method is able to sufficiently reconstruct soil structures with strong lateral velocity gradient or soils with a blind layer in noisy environments, using a single source and reasonable number of receivers. We have also proved the implementation of this method to real waveforms data, and succeeded in obtaining good correlation between the inverted 2D soil model and the existing borehole data. Finally, we applied our inversion to solve real geotechnical problem, where we successfully profiled the 2D soil structure and provide some evidences on the role played by shallow layers around the K-NET strong motion station MYG004 of Tsukidate (Miyagi prefecture) on amplifying high frequencies through numerical simulations.

Chapter 1

INTRODUCTION

1.1 Background:

Estimation of local site effects is one of major issues in the field of earthquake engineering. It has been well established that local geology significantly modifies strong motion and controls the irregular distribution of damage observed during large earthquakes. The most important parameter in local site amplification is S-wave velocity distribution in soil layers commonly referred to as the Average S-wave velocity (AVS). The AVS is derived from the total running time of the S-wave within the vertical direction, considering the layers as homogenous 1D entity with similar S-wave velocity and depth in the horizontal direction. One-dimensional soil profile can be obtain by different geophysical methods, using earthquake data or ambient noise recording to retrieve the vertical soil structure as well as borehole logging. The 1D assumption of the soil structure is widely accepted and easy to implement. In fact, seismic codes and current micro-zoning practices have almost exclusively relied on the one-dimensional analysis to predict surface motions at a site, thus overlooking any effect due to the horizontal soil variations.

This assumption can be correct if the soil layer velocities were indeed homogenous in the real world. However, in some cases important lateral variations occurs in the horizontal direction of soil layers, and the 2D and 3D effect can be more or less significant at the local site. The lateral heterogeneity in site effects, especially in small and shallow sedimentary basins has been recently observed (e.g.Coachella valley in California by Field, 1996; Colfiorito in Italy by Caserta et al., 1998). Since the engineering community became aware of the existence of such complex 2D effects and the need to taking them into account, the 2D characterization of the near surface ground structure started to gain huge importance from the exploration geophysicists.

As example of the 2D near surface effect, we can mention the observed case of the site located nearby the strong motion station K-NET Anamizu (ISK005) during the Noto-Hanto Earthquake in 2007 (Kobayashi et al.2009).

The Noto Hanto Earthquake (Mj=6.9) occurred on March 25, 2007, at Ishikawa prefecture in Japan. Strong ground motion over 100 cm/s of PGV was observed at the K-NET (ISK005) strong motion station at the town of Anamizu. However, the damage distribution in Anamizu town was not homogeneous. Hayashi et al. (2007) carried out shallow subsurface structure surveys, and suggested that the shallow subsurface structure with approximately 0m- 20m depth varied significantly in a horizontal direction around the K-NET Anamizu site. The relationship between this complex shallow structure and the site response was then analyzed by Goto al. (2009), where they numerically simulated the site response of the shallow subsurface structure in 2D and reported that amplification of the ground motions was mainly dependent on the depth of the layer boundary beneath the reference site. PGV at the site located 50m away from the K-NET strong motion station were about 80% of the observed PGV at the K-NET station.

This example illustrates the important role played by near surface lateral soil variations on seismic ground motions. Profiling the shallow layers and evaluating their effects on local site response can help to mitigate earthquake damage on constructions. A full profiling of the shallow soil may require 2D or 3D seismic exploration. Although many geophysical techniques are available to profile the shallow soil, each technique is subjected to advantages and disadvantages.

1.2 Two dimensional S-wave exploration methods:

1.2.1 SEISMIC REFRACTION METHODS:

The conventional seismic refraction method remains one of the cheapest and simplest methods for shallow soil investigations. In the seismic refraction, ground motion caused by an artificial impact is measured with receivers at a variety of distances from sources. Its efficient estimate of shallow soil velocities is routinely used in geotechnical engineering applications.

Refraction experiments are based on arrivals time of initial motion generated by a source recorded at a variety of distances. The data set derived from refraction experiments consists of series of travel times versus distances. They are then interpreted in terms of the depths to surface and the speeds at which motion travels through the subsurface within each layer. The method depends on the fact that seismic waves have different velocities in different types of soil. The waves are refracted when they cross a boundary between different layers.

Since this technique is based on the interpretation of the initial breaks of waves, it does not fully utilize waveforms contained in the data, and provides very basic information about the soil. The seismic refraction analysis, such as ‘The plus–minus Method’ (Hagedoorn,1959) and Conventional Reciprocal Method (D.Palmer 1980), originated as simple approaches allowing the grasp of a two-dimensional profile of soil: simple assumptions about the velocity structure are made, and a large velocity contrast between layers is assumed. The most important restriction of the conventional seismic refraction methods is its limited application to various types of soils. For example, these methods do not perform in the case of a velocity reversal soils as known as hidden layer problem.

One of the major developments in the seismic refraction survey is the application of travel time tomographic inversion. Recent developments had provided a geophysical tool able to perform where traditional refraction techniques fail. It can be used for models with velocity gradients, lateral velocity changes, and may be applied in settings that cannot be explored using the conventional seismic refraction method, such as areas of compaction, karsts, and fault zones (e.g., Zhang and Toksoz. 1998). However, the travel time tomography may suffer from resolution efficiency when it comes to determine sharp-layers interfaces, since it tends to smooth the layers interfaces (Sheehan.J.R 2005), and can be relatively expensive for routine application in practical domains.

1.2.2 SURFACE WAVES METHODS:

Active and passive surface wave techniques are relatively new seismic methods for the determination of shear wave velocity profiles. The basis of surface wave techniques is based on the dispersive feature of Rayleigh waves when it travels through a layered medium. Rayleigh wave phase velocity is determined by the material proprieties (primarily shear wave velocity) of the subsurface.

The active surface wave exploration became very popular in the last ten years for a shallow 2D soil exploration. Allowing more detailed exploration than the seismic refraction methods and less costly measurement than borehole explorations. Surface waves exist only in media with free surface. In the same medium, waves of different wavelengths affect different depths; if the medium is not homogenous they propagate with different velocities and different attenuations at frequency. As shown in Figure 1.1, longer wavelengths penetrate deeper and their velocity is affected by the material properties at greater depth. The phase velocity can be strongly frequency-dependent according to the material proprieties (primarily shear wave velocity and layer thickness) of the subsurface.

Active surface wave techniques measure surface waves generated by dynamic sources such as hammers, weight drop, etc. The impact excites the surface waves and most near-surface seismograms are mainly the Rayleigh waves which contains information about the soil S-wave velocity.

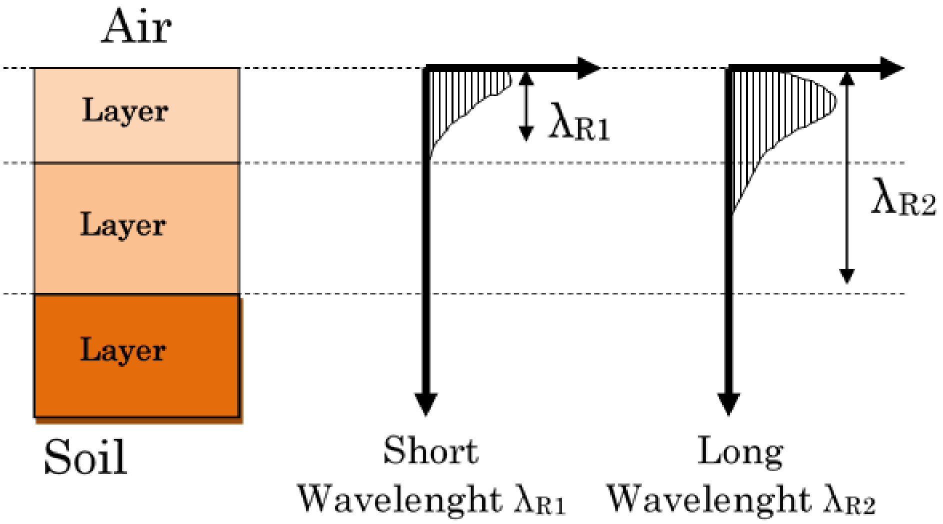

Figure 1.1: Schematic representation of geometric dispersion of Rayleigh waves: The vertical displacement associated with a short and a long wavelength.

Many approaches based on the dispersive characteristics of the surface waves have been reported in literature. Since the eighties, the spectral analysis of surface waves (SASW) initiated by Nazarian and Stokoe (1984), has been widely used in geotechnical engineering applications. The SASW method uses a dynamic source to generate surface waves of different wavelengths which are monitored by two or more receivers to sample the desired frequency range. Data are analyzed in the frequency domain to produce a dispersion curve by calculating the phase difference between each deployment of receiver’s pair. The phase velocity can then be inverted to a 1D soil profile.

The Multi-channel analysis of surface waves (MASW) (Park et al., 1999a; Xia et al., 1999) is considered as an upgraded method of the SASW. The field layout is similar to that of the seismic refraction technique. Several receivers are laid out in a linear array and connected to a multi-channel seismograph. The source is offset at a predetermined distance from the near geophone usually determined by field testing. Rayleigh wave dispersion curve is obtained by a wave field transformation of the seismic records, which allow isolating surface waves energy from that of body waves.

This technique is ideally suited to 2D Vs imaging, for reconstruction of a pseudo 2D S-wave velocity structure by aligning 1D S-wave velocity profiles at the midpoint of receivers, opening a new perspective on the two-dimensional surface wave exploration. When smoothed lateral variations are presumed at a site, the processing is usually performed assuming local 1D system by neglecting lateral variations on each dispersion. Nevertheless, this assumption is not always true and depends on the nature of the lateral variations and the processing technique used (Boiero et al, 2011). Some soil structures (layers with strong lateral heterogeneity) generate a jump of the Rayleigh wave's energy from the fundamental mode to higher modes, as well as a generation of unwanted non-surface waves making the inversion technically challenging. Several authors considered a multi-modal inversion of the surface waves (Strobbia and Foti 2006, Socco et al., 2010), including both fundamental mode and higher modes in the inversion. But all of them reported the complexity to retrieve the dispersion curve for the two-dimensional surface wave approaches. Since the major difficulty of the MASW comes from the proper determination of the dispersion curves in 2D, it could be overcome if the inversion relies on time series instead of the dispersion analysis.

1.2.3 FULL WAVE FORM INVERSION (FWI):

In 1984 Albert Tarantola presented an inversion solution for seismic reflection data by waveform fitting, which is known as the Full Waveform Inversion (FWI) technique. The FWI is the last procedure for extracting information from seismograms; it can offer a very good alternative for two-dimensional near surface exploration.

In this method waveforms of seismic records are directly used as an input for the inversion, giving the possibility to invert complex soil model with lateral heterogeneity by exploiting both travel time and waveform attributes such as phase and frequency content. The elastic properties of the geological layers are directly estimated, resulting in a property image of the subsurface. This is accomplished by minimizing the difference between the simulated and the recorded seismic data.

The full elastic wave equation that calculates the simulated waveforms must be solved through volumetric modeling methods such as the finite-differences or finite-elements methods, allowing calculation of required travel time and waveform information for all events within the wave field. Hence, the efficiency of the process closely depends on the realism of the associated forward solution to account for the characteristics of the medium.

Although the theory of the FWI was developed in the eighties, the waveform fitting imaging was quite computer demanding at that time even for 2D geometries. In the late 90's, Pratt et al. (1999) started developing waveform inversion in the frequency domain. Pratt suggested that by using single discrete frequency one can reduce the computation cost significantly, starting with low frequencies and then successively invert higher frequency data. Since then, developments on computing hardware allowed two dimensional FWI (e.g.Thierry et al., 1999; Sears et al., 2008), it became a key tool in exploration geophysics, and it has only recently been successfully applied for elastic 3D inversion to a full-scale field data set in oil exploration industry (Guasch et al.,2012). Since the FWI is mainly used in petroleum geophysics, only few studies related to the wave-form inversion have been conducted for near surface investigations, some results of these studies are summarized in Figure 1.2.

In an attempt to invert the 2D shallow soil structure, a primary study was initiated by Takekoshi and Yamanaka (2009), where they used inversion of SH waves to retrieve a two-dimensional soil structure with a blind layer using numerical experiments. Comparison between the target model in Figure 1.2a and the averaged model from 10 different inversions in Figure 1.2b shows that the blind layer and the slope of the interfaces have been well reproduced through the waveform inversion process.

A similar study was carried out by Yamanaka and Yamauchi (2010), where they successfully applied this method to real acquired SH waveforms to retrieve a 2D layer structure on field. In this method, the authors added pre-processing of the observed data by introducing deconvolution using reference station in order to eliminate the effects of the source. The authors succeeded to determine the 2D soil model using a single shot and only 4 receivers (Figure 1.2c), and compared their inverted model with a soil model obtained with the conventional seismic refraction method.

Zeng et al. (2011) also discussed the numerical feasibility of the waveform inversion of Ralyleigh waves for shallow shear-wave velocity using genetic algorithm inversion. The authors performed successful waveform inversion of Rayleigh waves for different 2D soil configurations with a simplified lateral heterogeneities: a soil consisting of a tunnel inside a homogeneous half-space, a two layer single step-shaped soil model and a soil model with a single dipping interface illustrated in Figure 1.2d and its inverted model in Figure 1.2e.

A more complex numerical example was achieved by Romdhane et al. (2011), where they evaluated the potentiality of a 2D elastic FWI approach when applied to shallow 2D structures in the presence of a complex topography. The authors used an elastic forward modeling based on a Galerkin approach, and assumed a priori known source wavelet in their tests. Synthetic study successfully inverted Rayleigh waves of a complex geological setting, modeled from real land slid, illustrated in Figure 1.2f , The FWI process in the frequency domain succeeded to reconstruct the geological model as in Figure 1.2g.

Tran and McVay (2012) discussed synthetic and field data application of the FWI, where they inverted surface waves up to 20Hz to image the subsurface structure down to 20m depth. The authors applied elastic FWI in the time domain including elastic forward modeling. In their synthetic tests they succeeded to fully reconstruct low and high velocity layers in the 2D S-wave velocity for both, noise-free and noisy data. The authors also succeeded to resolve a low velocity layer model using field data. The S-wave velocity model obtained is compared to a standard penetration test (SPT) analysis, showing consistent comparative results.

Laboratory experiments were conducted by Bretaudeau et al. (2013), proving the applicability of 2D elastic FWI for a layered medium with an inclusion, which are obtained by small scale physical modeling. The used inversion scheme is formulated in the frequency domain and considers anelastic propagation.

More recently, Kallivokas et al. (2013) discussed the progress in the full-waveform based imaging and succeeded the first attempt of 2D geotechnical site characterization using FWI technique to real data, shown in Figure 1.2h.

Most of these works remains experimental, and not many of them were successful on real data. Further research and developments are still needed are needed to promote the new field of full wave-form inversion for 2D near surfaces.

Authors	2D Target Model	2D inverted model
Takekoshi Yamanaka (2009)	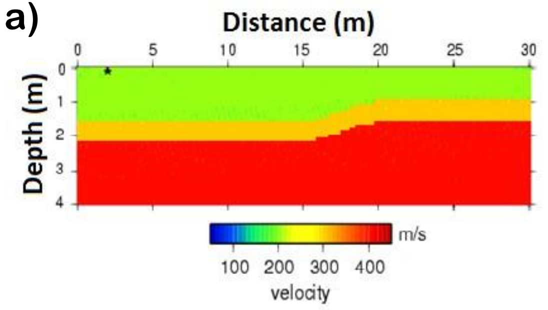	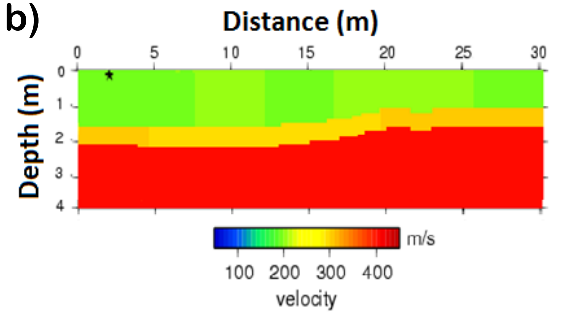
Yamauchi Yamanaka (2011)	**Field Data**	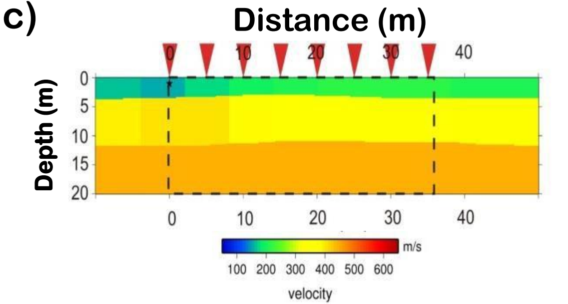
Zeng et al. (2011)	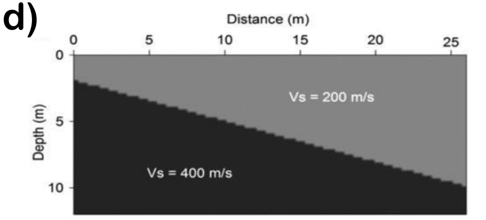	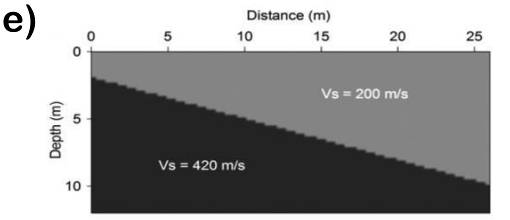
Romdhane et al. (2011)	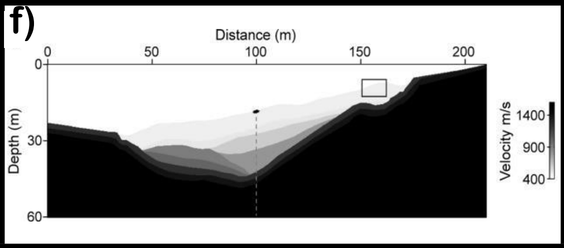	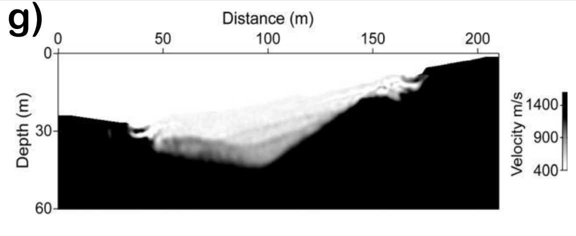
Kallivokas et al. (2013)	**Field Data**	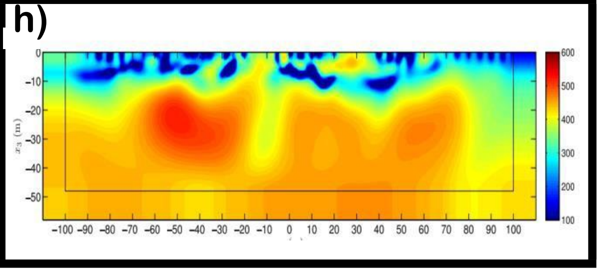

Figure 1.2: Results from near-surface 2D waveform inversion reported in literature.

1.3 Objectives of this research:

Most of man-made constructions involve some structural element with direct contact with ground, and the understanding of the two-dimensional physical proprieties of soils can be very important for site response and seismic wave amplification analysis in irregular basins (Semblat, 2005), for earthquake engineering purposes such as soil-structure interaction studies (Jaramillo, 2014), or near surface exploration purposes (Hayashi et al., 2009).

The objective of this research is to propose an alternative approach to the preexisting 2D near-surface exploration methods, which can profile a shallow 2D soil structure that other conventional near-surface methods have difficulties to properly retrieve. The method we are proposing is based on the time domain waveform inversion of waves acquired from conventional seismic refraction survey, similar to the one proposed by Takekoshi and Yamanaka (2009) and Yamanaka and Yamauchi (2010) for SH wave inversion.

The motivation behind furthering our research to P-SV waveform, is because of the difficulty of SH wave acquisition on filed. Special disposition is required to properly generate horizontal waves (Franklin, 1979), if the impact of the hammer is not precisely aligned in horizontal direction, unwanted P and SV waves will be generated along the line of the survey interfering with the SH waves. Another limitation of the SH wave inversion is the inability to properly underline the P wave arrivals, since the SH wave field do not include Vp, it won’t be able to represent the Poisson’s ratio of the soils. For this reasons, it was important to implement this technique for P-SV waveforms inversion.

This method uses the model acquired by an active source as input; it is based on the numerical soil modeling and the waveform inversion of the P-SV waves. The inversion process consists of calculating the difference between the target waveforms, and the waveforms computed from the numerically generated soil models.

While most of the FWI methods presented in the literature are based on the local least-square optimization formulation, our inversion is based on a heuristic approach that retrieves the soil model without the need to predefine an appropriate starting model. We will try to prove its applicability using different numerical experiments and field data experiments.

1.4 Thesis organization:

This thesis summarizes the different aspects of the 2D inversion method we are proposing, from its conception, to its implementation for real engineering problems.

Chapter 1 is an introduction where we explained the background and the motivations behind proposing an alternative 2D near- surface exploration method. We presented a general overview of the current near-surface exploration methods, explaining their advantages and pitfalls, and illustrated with some results from recent literature.

Chapter 2 describes the methodology utilized to achieve a 2D waveform inversion. We first explained the inversion strategy in our method, and the theoretical aspect of seismic wave propagation. Then we detailed the forward modeling of our method to simulates the behavior of waves in 2D model, the subsurface layer modeling that materialize the numerical soil model, to the inversion algorithms utilized to retrieve a 2D soil model from waveforms. This chapter also explains the waveform deconvolution procedure utilized in our method that allows a source effect free inversion.

Chapter 3 discusses the numerical tests of our method. We estimated the feasibility of our 2D inversion for different soil configurations that might be more or less challenging to retrieve using the conventional near-surface exploration methods, using both noise-free and noisy data. We also conducted a parametric study where we underlain the effect of the different parameters on our 2D inverted model, and compared our method with the conventional refraction method.

Chapter 4 aims to prove the applicability of our method to real seismic data acquired on field. We tried to retrieve a 2D soil model for a given area inside our university campus, where borehole data were available. We then compared our results with the borehole data and other exploration results conducted within the area of interest to confirm the performance of our method.

Chapter 5 illustrates the usefulness of our method on solving real earthquake engineering problems, in a case study where near-surface layers were responsible of abnormal site amplifications during the 2011 off the Pacific Coast earthquake of Tohoku. We applied our method to obtain a 2D shallow soil structure, and compared our results with other geophysical studies previously carried out in the same area. We also conducted numerical earthquake motion simulations that show the effect of the shallow soil layers and local topography on the local site amplification.

Chapter 6 concludes our work underlying the advantages and disadvantages of our technique, as well as the possible further developments to upgrade our method for more challenging soil configurations.

Chapter 2

METHODOLOGY

2.1 Inversion strategy:

In our waveform inversion, we use seismic waves generated at the surface to profile a 2D soil structure. These waves are the result of interfering P and SV waves with the elastic proprieties of the medium. In a layered elastic model, the P-SV waves consist of both compressive and shear motions which are coupled by the vertical gradient of the material proprieties, and the surface waves of the P-SV system are called Rayleigh waves. During the propagation of the Rayleigh waves the soil inhomogeneities undergo complex oscillations, it will be possible to assume that the scattered field is excited by force sources and their dependence on time is determined by the shape and internal structure of the inhomogeneity as well as the spatial distribution of the incident wave field (Razin, 2010). The scattering of the Rayleigh waves can then be utilized to solve inverse problems and retrieve internal structure of the two-dimensional shallow soils.

Our inversion method uses the vertical component of Rayleigh waves generated in a P-SV wave field by sledge hammering. These waveforms are inverted in the time domain in order to reconstruct a numerical equivalent of a two-dimensional soil structure that can fit the observed waveforms. The inversion is based on the numerical modeling of the soil structure: observed seismograms are compared to synthetic waveforms calculated from a numerically generated soil model.

The numerical soil is structured by several blocks with specific physical parameters. The parameters to be inverted are the shear wave (S-wave) velocities of each block, and the depth parameter that defines the layer interfaces. Other parameters such as P wave velocities or densities can either be assumed, or provided by other exploration method.

The inversion strategy consists of finding an optimal 2D numerical model with the appropriate block velocities and interface depth. This operation will be achieved by calculating the difference between the observed and calculated waveforms in an iterative trend, until a satisfactory match is obtained between synthetics and real data accordingly to the scheme illustrated in Figure 2.1.

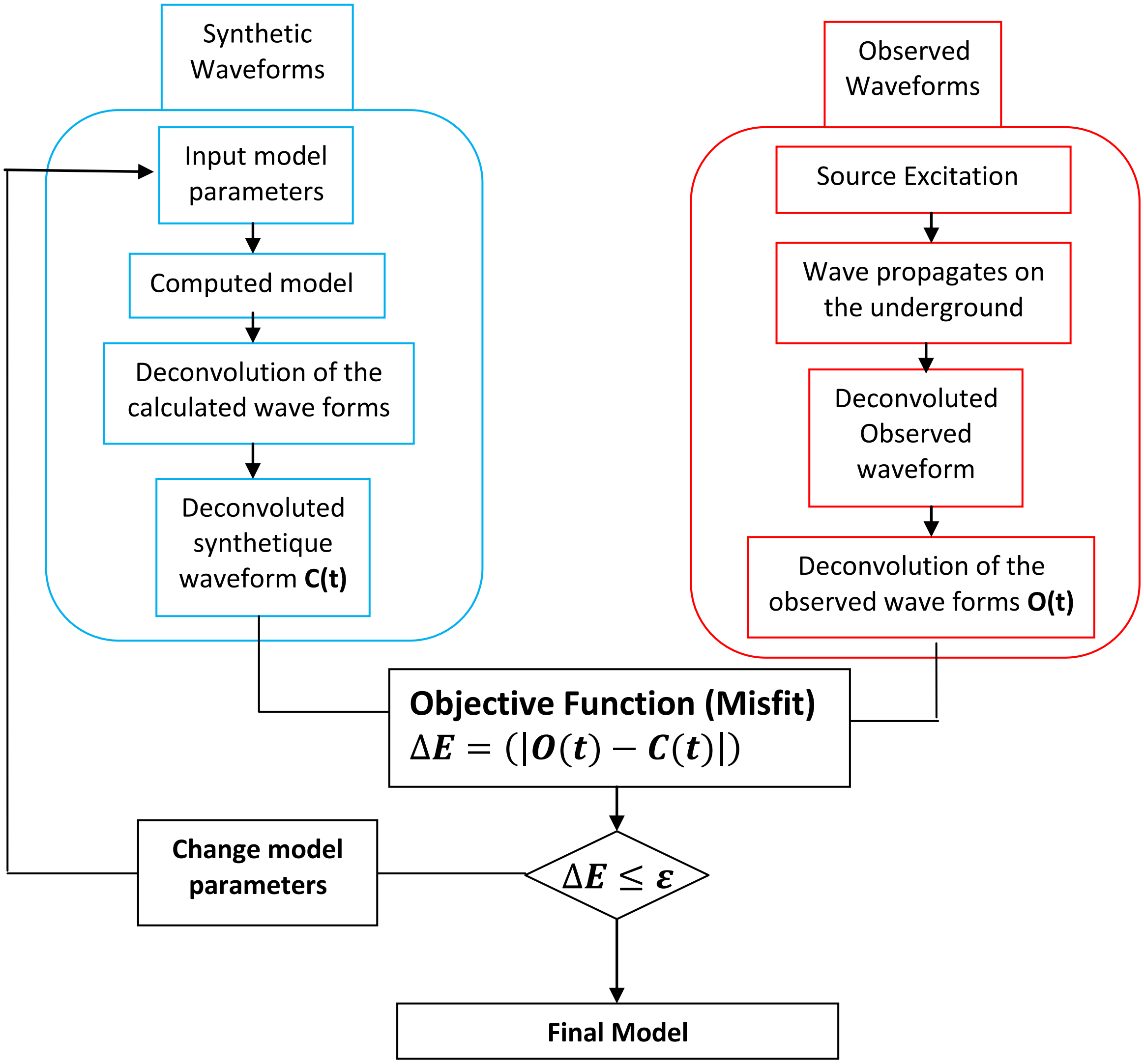

Figure.2.1: Flowchart of the inversion strategy used in our method.

2.2 Forward modeling:

The technique of forward modeling consists of the numerical solution of the equation of motion for seismic waves, or more specifically, the numerical computation of the theoretical seismograms for a given geological model of the subsurface. The forward modeling is the opposite operation of the inverse modeling approach in which the parameters of the geological model are computed from the acquired real data.

To build the forward model that simulates the behavior of waves inside a soil model, we used the Finite Difference method (FDM). The FDM is a numerical approach for solving partial differential equations; the main idea behind the FDM is to compute the wave-field at a discrete set of closely-spaced grid points. It can be applied to the wave equation of P-SV motion to compute ground velocity at any point in a given geological model. In our inversion method, we used the staggered formulation for P-SV equation proposed by Virieux (1984), adopting the 4th order approximation for space and the 2nd order approximation for time.

For a more realistic simulation, the classical 2D P-SV equations of motion implemented in the FD scheme are upgraded to the 2.5D P-SV equations in order to include the three-dimensional spreading in a 2D plan (Narayan 1998). The 2.5D equations of motion were derived from the 3D equations in a cylindrical coordinate system (r,z,θ), where r,z and θ are radial, vertical and tangential coordinates. The 2.5D simulation consists of setting all the derivatives on the θ plane to zero, and the 2.5D P-SV equations of velocity v_i and stress τ_{ij} can then be written, respectively as follows:

$$\frac{\partial v_r}{\partial t} = \frac{1}{\rho}\left(\frac{\partial \tau_{rr}}{\partial r} + \frac{\partial \tau_{rz}}{\partial z} + \frac{\tau_{rr}}{r}\right); \qquad (1.1)$$

$$\frac{\partial v_z}{\partial t} = \frac{1}{\rho}\left(\frac{\partial \tau_{rz}}{\partial r} + \frac{\partial \tau_{zz}}{\partial z} + \frac{\tau_{rz}}{r}\right); \qquad (1.2)$$

$$\frac{\partial \tau_{rr}}{\partial t} = (\lambda + 2\mu)\frac{\partial v_r}{\partial r} + \lambda\frac{\partial v_z}{\partial z} + \lambda\frac{v_z}{r} \qquad (1.3)$$

$$\frac{\partial \tau_{zz}}{\partial t} = (\lambda + 2\mu)\frac{\partial v_z}{\partial z} + \lambda\frac{\partial v_r}{\partial r} + \lambda\frac{v_r}{r} \qquad (1.4)$$

$$\frac{\partial \tau_{zr}}{\partial t} = \mu\left(\frac{\partial v_r}{\partial z} + \frac{\partial v_z}{\partial r}\right); \qquad (1.5)$$

where λ and μ are Lamé parameters of elasticity, and ρ is the density. The models are pure-elastic mediums where the Q value doesn't have big effect on the calculated waveforms.

The equations of motions are solved through a discrete set of closely spaced grid points, by approximating their derivatives using the horizontal *(U)* and the vertical *(W)* components of the P-SV wave velocity, as well as the normal stress τ_{rr}, τ_{zz} and shear stress τ_{xz}. A schematic representation of the FD grid can be seen at Figure 2.2a, distribution of the horizontal (U) and vertical (W) velocities is depicted by circles and squares, while normal stress τ_{rr}, τ_{zz} and shear stress τ_{xz}, are represented by regular and reversed triangles. The Figure 2.2b shows the approximation of stress equations. All parameters are set to 0 everywhere in the medium at the initial stage of calculation, and it is said to be at equilibrium.

Time marching process starts from the source, propagates through the grid and progress in time after each time step 'dt' as illustrated in Figure 2.2c.

The equations to approximate the solution inside the finite difference grid for velocities and stress can be written as follow:

$$\rho_{i,j}\frac{\partial \dot{w}_{i,j}^{t}}{\partial t}=\frac{\partial \dot{w}_{i,j}^{t+1}}{\partial t}+\frac{9}{8}\left(\frac{\tau zr_{i,j}^{t+1}-\tau zr_{i-\frac{1}{2},j}^{t+1}}{\Delta r}\right)-\frac{1}{24}\left(\frac{\tau zr_{i+\frac{1}{2},j}^{t+1}-\tau zr_{i-\frac{3}{2},j}^{t+1}}{\Delta r}\right)+\frac{9}{8}\left(\frac{\tau zz_{i,j+\frac{1}{2}}^{t+1}-\tau zz_{i,j}^{t+1}}{\Delta z}\right)+\frac{1}{24}\left(\frac{\tau zz_{i,j+\frac{3}{2}}^{t+1}-\tau zz_{i,j-\frac{1}{2}}^{t+1}}{\Delta z}\right)$$
$$+\frac{1}{r}\left[\frac{9}{16}\left(\tau zr_{i,j}^{t+1}+\tau zr_{i-\frac{1}{2},j}^{t+1}\right)-\frac{1}{16}\left(\tau zr_{i+\frac{1}{2},j}^{t+1}+\tau zr_{i-\frac{3}{2},j}^{t+1}\right)\right]\qquad(2.1)$$

$$\rho_{i,j}\frac{\partial \dot{u}_{i,j}^{t}}{\partial t}=\frac{\partial \dot{u}_{i,j}^{t+1}}{\partial t}+\frac{9}{8}\left(\frac{\tau rr_{i+\frac{1}{2},j}^{t+1}-\tau rr_{i,j}^{t+1}}{\Delta r}\right)-\frac{1}{24}\left(\frac{\tau rr_{i+\frac{3}{2},j}^{t+1}-\tau rr_{i-\frac{1}{2},j}^{t+1}}{\Delta r}\right)+\frac{9}{8}\left(\frac{\tau zr_{i,j}^{t+1}-\tau zr_{i,j-\frac{1}{2}}^{t+1}}{\Delta z}\right)+\frac{1}{24}\left(\frac{\tau zr_{i,j+\frac{1}{2}}^{t+1}-\tau zr_{i,j-\frac{3}{2}}^{t+1}}{\Delta z}\right)$$
$$+\frac{1}{r}\left[\frac{9}{16}\left(\tau zz_{i+\frac{1}{2},j}^{t+1}+\tau zz_{i,j}^{t+1}\right)-\frac{1}{16}\left(\tau zz_{i+\frac{3}{2},j}^{t+1}+\tau zz_{i-\frac{1}{2},j}^{t+1}\right)\right]\qquad(2.2)$$

$$\frac{\partial \dot{\tau} rr_{i,j}^{t}}{\partial t}=\frac{\partial \dot{\tau} rr_{i,j}^{t+1}}{\partial t}+\frac{dt}{\Delta r}\left(\lambda_{i,j}+2\mu_{i,j}\right)\left[\frac{9}{8}\left(u_{i,j}^{t}-u_{i-\frac{1}{2},j}^{t}\right)-\frac{1}{24}\left(u_{i+\frac{1}{2},j}^{t}-u_{i-\frac{3}{2},j}^{t}\right)\right]+\frac{dt}{\Delta r}\lambda_{i,j}\left[\frac{9}{8}\left(w_{i,j}^{t}-w_{i,j-\frac{1}{2}}^{t}\right)+\frac{1}{24}\left(w_{i,j+\frac{1}{2}}^{t}-w_{i,j-\frac{1}{2}}^{t}\right)\right]$$
$$+\frac{dt}{r}\lambda_{i,j}\left[\frac{9}{16}\left(u_{i,j}^{t}+u_{i-\frac{1}{2},j}^{t}\right)-\frac{1}{16}\left(u_{i+\frac{1}{2},j}^{t}+u_{i-\frac{3}{2},j}^{t}\right)\right]\qquad(2.3)$$

$$\frac{\partial \dot{\tau} zz_{i,j}^{t}}{\partial t}=\frac{\partial \dot{\tau} zz_{i,j}^{t+1}}{\partial t}+\frac{dt}{\Delta r}\left(\lambda_{i,j}+2\mu_{i,j}\right)\left[\frac{9}{8}\left(w_{i,j}^{t}-w_{i-\frac{1}{2},j}^{t}\right)+\frac{1}{24}\left(w_{i+\frac{1}{2},j}^{t}+w_{i-\frac{3}{2},j}^{t}\right)\right]+\frac{dt}{\Delta r}\lambda_{i,j}\left[\frac{9}{8}\left(u_{i,j}^{t}-u_{i-\frac{1}{2},j}^{t}\right)-\frac{1}{24}\left(u_{i+\frac{1}{2},j}^{t}-u_{i-\frac{2}{3},j}^{t}\right)\right]$$
$$+\frac{dt}{r}\lambda_{i,j}\left[\frac{9}{16}\left(u_{i,j}^{t}+u_{i-\frac{1}{2},j}^{t}\right)-\frac{1}{16}\left(u_{i+\frac{1}{2},j}^{t}+u_{i-\frac{2}{3},j}^{t}\right)\right]\qquad(2.4)$$

$$\frac{\partial \dot{\tau} zr_{i,j}^{t}}{\partial t} = \frac{\partial \dot{\tau} zr_{i,j}^{t+1}}{\partial t} + dt\mu_{i,j}\left(\frac{9}{8}\frac{w^{t}_{i+\frac{1}{2},j} - w^{t}_{i,j}}{\Delta r} + \frac{1}{24}\frac{w^{t}_{i+\frac{2}{3},j} - w^{t}_{i-\frac{1}{2},j}}{\Delta r} + \frac{9}{8}\left(u^{t}_{i,j+\frac{1}{2}} - u^{t}_{i,j}\right) + \frac{1}{24}\left(u^{t}_{i,j+\frac{2}{3}} + u^{t}_{i,j-\frac{1}{2}}\right)\right) \quad (2.5)$$

$$r = \sqrt{[(i-(nqx+0.5))*\Delta r]^2 + [(j-(nqz+0.5))*\Delta z]^2} \quad (2.6)$$

Where ρ is the density of the medium, *nqx* and *nqz* are source position and *(i,j)* are the grid coordinates, Δr and Δz are the cells size in both horizontal and vertical direction respectively.

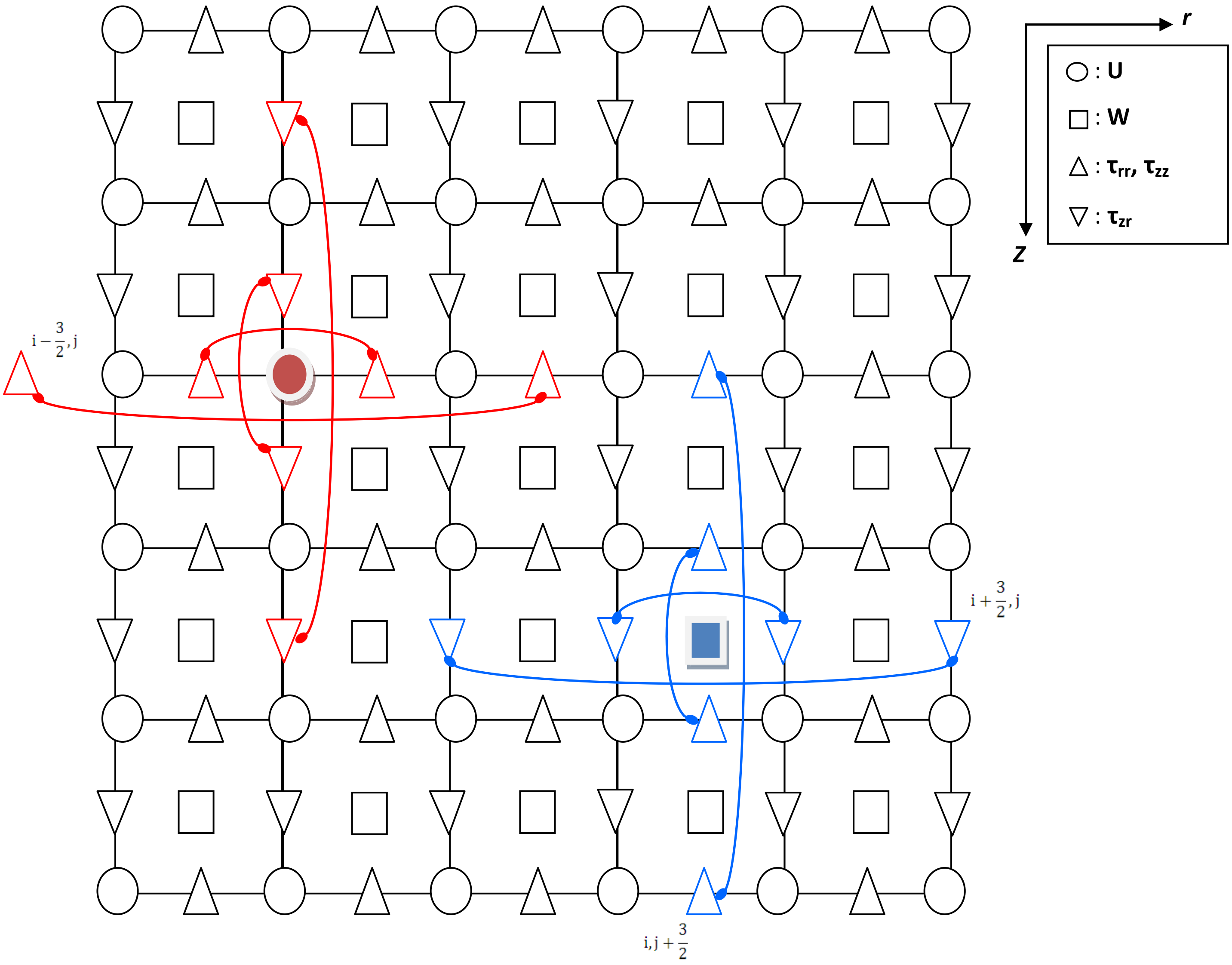

Figure.2.2a: 4th order approximation for velocity.

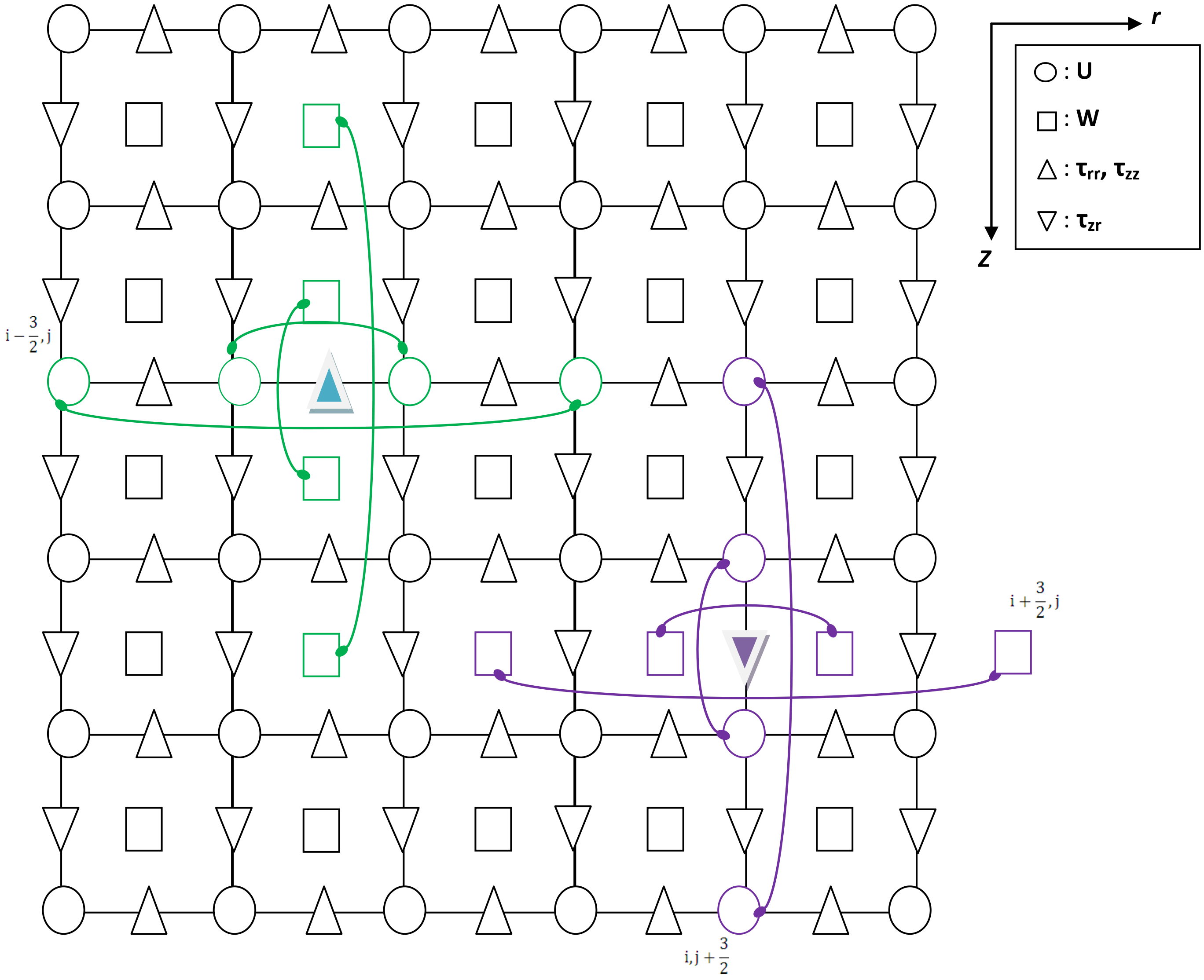

Figure.2.2b: 4th order approximation for stress.

🟥 : Source excitation.

🟩 : 1st approximation for stress.

🟦 : 1st approximation for velocity.

🟨 : 2nd approximation for stress.

🟫 : 2nd approximation for velocity.

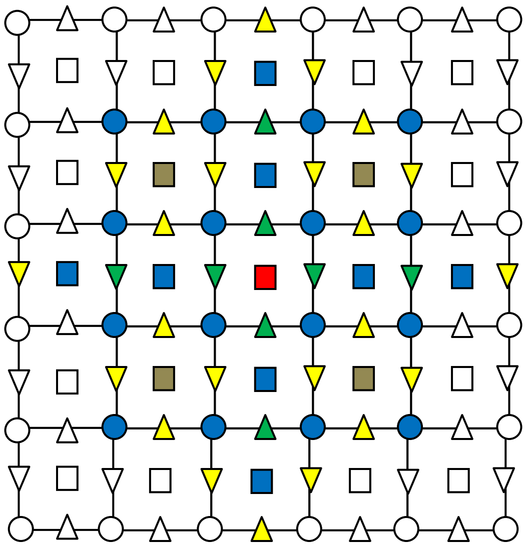

Figure.2.2c: Representation of the time marching process at each time step ‘dt’.

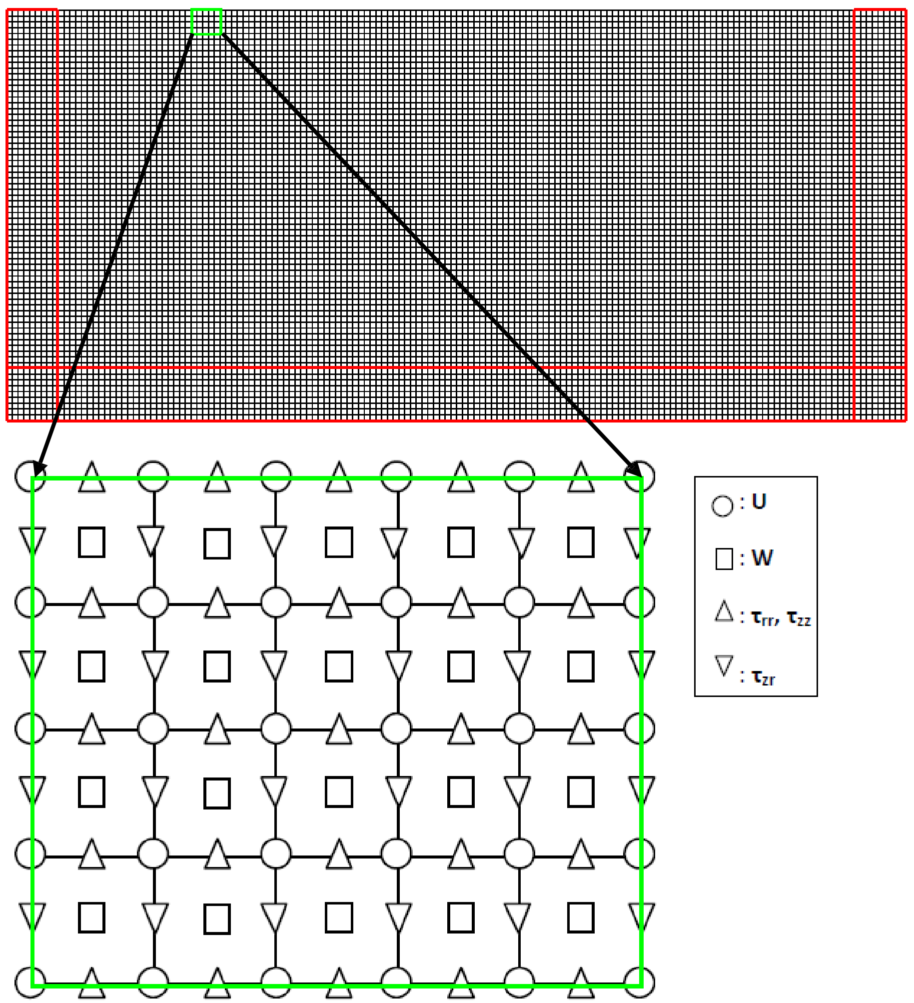

Figure.2.2d: Illustration of the FD grid used for forward modeling, with absorbing buffer area in red, and magnificence of the staggered grid in green square box.
U: Horizontal velocity. W: Vertical velocity.
τ_{rr}, τ_{zz} : Normal stress. τ_{xz} : Shear stress.

The most persistent problem in the numerical wave simulation is the artificial reflections engendered by the edges of the computational grid. To reduce these reflections, absorbing boundaries were introduced in our numerical model. The absorbing boundary proposed by Clayton and Enquist (1977) was implemented at the right, left and bottom edges of the numerical model to reduce the reflections. We also add a buffer region to the edges of the model (Cerjan et al., 1985) of 3m that plays the role of a 'sponge' area, eliminating the unwanted reflections, borders of these buffer areas are highlighted by red color in the grid of Figure 2.2d. Although the absorbing boundary conditions have been applied, we made a computational area sufficiently large to avoid any wave reflection artifacts during the computation. We assumed a horizontal surface boundary on the top of the model, which means that we neglected wave scattering induced by local topography. The free surface was implemented by stress free condition at the top of the computational grids.

One of the pitfalls of the FD simulation is its limited range of performance; the stability of the numerical schemes is closely related to the numerical error. The stability condition used for the time marching calculation according to Levander (1988) is:

$$\Delta t < \frac{6}{7\sqrt{2}} \frac{dx}{V_{pmax}} \qquad (3)$$

Where Δt and dx are the time step and the grid spacing, and $Vpmax$ is the maximum P wave velocity.

To minimize the effects of the truncation error due to the mesh size, we should also consider the ratio between the grid spacing and the minimum S-wave velocity, considering at least 16 grids per minimum wave length in this study. A vertical point source of the Ricker wavelet was generated near the surface to simulate plank hammering and virtual receivers on the surface recorded vertical response of the medium.

2.3 Data processing before inversion:

One of the major difficulties to overcome in the waveform inversion is the source effect on the recorded signals, making the full-waveform inversion technically difficult to apply (Lee. et al., 2003). Since we are not supposed to know the shot frequency of the plank hammering during the data acquisition, it is very important to get rid of the source effects from the raw signals. For this purpose, we applied a source deconvolution to both observed and calculated waveforms in order to perform a waveform inversion free from source signature (Yamanaka et al. 2010).

Let's consider a given soil model where we input a vertical excitation with a source function *S(t)*, the waves travel through the medium where they interact with the physical soil proprieties and undergo a convolution with the Green function of the soil. The vertical signal $O_j(t)$ recorded at each station *j* can then be written as:

$$O_j(t) = G_j(t) * S(t) \qquad (4)$$

Where $G_j(t)$ is the vertical component recording the Green function from the P-SV wave field at each station *j* and *S(t)* is the input source function. The asterisk stands for the convolution between the source function and the Green function.

In order to execute the deconvolution, we need to transform the equation (4) to the frequency domain, and divide all the spectrum of the recorded waves for each station *j* by a reference station *r*, the division in the frequency domain can be applied as follows:

$$D_j^O(\omega) = \frac{O_j(\omega)}{O_r(\omega)} = \frac{G_j(\omega)S(\omega)}{G_r(\omega)S(\omega)} = \frac{G_j(\omega)}{G_r(\omega)} \qquad (5)$$

Where $D_j^o(\omega)$ is the spectral ratio of the division in the frequency domain, and $O_r(\omega)$ is the spectrum at the reference site. In equation (4), the source spectrum cancels out, so that the signal will only include the Green's function of the soil. The instruments response can be dropped by assuming that all the geophones have the same calibration which is already known, and would disappear during the deconvolution. After the deconvolution in the frequency domain, a cosine band-pass filter is applied to keep only the frequencies of our interest. All we need to do is to transform the deconvoluted filtered spectra $D_j^o(\omega)$ back to the time domain for the data free from source effects. However, to ensure numerical stability the following equation is used in actual processing:

$$D_j^o(t) = F^{-1}\left[\frac{O_j(\omega)O_r^*(\omega)}{O_r(\omega)^2+\varepsilon}\right], \quad (6)$$

where F^{-1} is the inverse Fourier transform and * denotes the complex conjugate. ε is a small value set to 0.1% of averaged amplitude of the observed data.

2.4 Subsurface modeling:

We often see that geological discontinuities in soils are one of the important features of soil model. In seismic tomography inversion, subsurface is often parametrized using many cells. However, one of the difficulties of refraction tomographic imaging is to properly underline layer interfaces (Sheehan et al. 2005). To materialize geological discontinuity in our numerical model, we use the combination of the tomographic cell and the layer interface modeling proposed by Aoi et al. (1995), similarly to Takekoshi and Yamanaka (2009). Compared to tomographic imaging, this technique has advantage to reconstruct a geological discontinuity using a low number of parameters to be inverted with lateral inhomogeneity. Each interface boundary is materialized using a linear combination of basis functions $C_x(x)$, coefficients P_k, and interface depth $d(x)$ as shown in the following equation:

$$d(x) = \sum_{k=1}^{L} P_k C_k(x), \qquad (7)$$

where L is the number of the basis functions. Each basis function is defined in Equation (8), where Δ is the function dimension and x_k is the distance of the function k at the x direction along the surface.

$$C_k(x) = \begin{cases} \frac{1}{2} + \frac{1}{2}\cos\left(\frac{\pi}{\Delta(x - x_k)}\right) & x_{k-1} \le x \le x_{k+1} \\ 0 & otherwise. \end{cases} \qquad (8)$$

Each layer is divided into several blocks with different depth and velocities. The inversion process consists of attributing suitable values for the depth parameter and S-wave velocities to each block simultaneously in order to determine an appropriate soil model that matches our targeted waveforms. For a better understanding of the interface function system implemented in equation (7) and (8), an illustrated example is provided in Figure 2.3.

The model is a 15m x 9m size, and consists of two layers separated by an irregular interface at depths of 3m to 6m. In our study we set the number of the basis function equal to number of blocks, the first layer is divided into 15 blocks of 1m width and constant S-wave velocity of 250m/s, delimited by dark grey lines, and 15 basis functions (L=15) illustrated by white trigonometric curves defined in equation (8). The interface boundary shape *d(x)* in equation (7) is overlain by a white dashed line in Figure 2.3, this interface is built by the white trigonometric functions $C_k(x)$ and depth parameter P_k.

In order to stabilize the inversion, we increase the lateral dependency between the blocks by using a smoothing factor for the velocities and depth parameters within the same layer. The smoothing was applied by simple averaging of the velocity of each block and Pk with the adjacent ones. We assumed a homogeneous S-wave velocity for the basement layer in the bottom of the model.

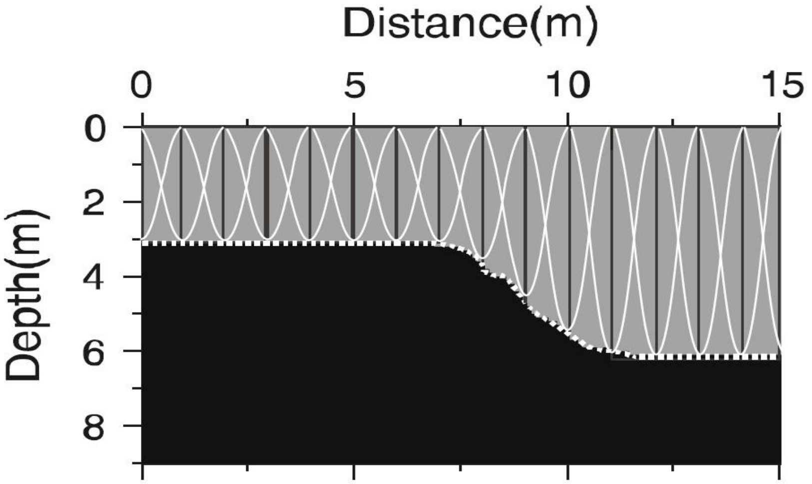

Figure.2.3: Numerical example of the soil block modeling.
Blocks are delimited by the solid black line, basis functions shown as white trigonometric curves, and the interface boundary shape as the white dashed line.

2.5 Nonlinear inversion algorithms:

Stochastic optimization methods, also referred to as Monte Carlo search methods are based on a purely random search process. In contrast to the linear least square optimization methods that search for the minima of the misfit function near a given initial model, Monte Carlo methods search for the global minimum of the misfit function even in the absence of an appropriate initial model. Among the Monte Carlo optimization methods, the Genetic Algorithm (GA) (e.g. Yamanaka and Ishida, 1999), and the Simulate Annealing (SA) (e.g. Yamanaka, 2001) became increasingly popular for the inversion of geophysical data.

The GA simulates the principles of biological evolution such as mutation and crossover to find the most appropriate models from a set of data in an iterative trend, with an increase in solution efficiency over the random walk strategy. Three genetic operations are applied to the genetic type parameter of the model through selection, crossover and mutation (Yamanaka and Ishida, 1999). The selection process consists of choosing the individuals with the best misfit for the next generation of computation; the selected models are then subjected to crossover and mutation. Although the crossover and mutation might generate a model with a large model, such a model has a low possibility to be chosen in the selection for the next generation. Thus, only models with small misfits will survive in many generations.

One of the pitfalls in GA computation, is its big computational demand. Another problem frequently found in the GA optimization is the premature convergence: the dominance of crossover can result in stagnation as the population becomes more homogeneous and the mutation rate is too low to move search to other areas (Alder, 1993). In an attempt to improve these deficiencies, several authors have proposed a hybrid approach merging the GA with the SA to minimize the misfit function more efficiently (e.g. Sen et al, 1991, Li et al, 2002).

The SA is based on the idea of thermodynamics whereby molten metal reaches to a low energy state with gradual decrease of temperature. The parameter perturbation is controlled by a cooling schedule that is characterized by a decrease rate of temperature. With this analogy, a model can be gradually modified toward the optimal solution.

The inversion algorithm used in our method is the hybrid heuristic search method proposed by Yamanaka (2007). This algorithm is one of the hybrid heuristic search methods, combining the GA and the SA. The robustness of the hybrid heuristic search algorithm comes from its non linear stochastic behavior that can find an optimal solution independent from an initial model, with less computational efforts than those of the conventional GAs or SAs. This method had shown excellent results on inverting phase velocities of Rayleigh waves for one dimensional soil profiles (e.g., Zaineh et al., 2012), as well as 2D soil profiles inversion using the SH waves inversion (e.g., Takekoshi and Yamanaka, 2009).

The basic search engine of the hybrid algorithm is principally based on the GA utilized by Yamanaka and Ishida (1999) with three genetic operations of selection, crossover and mutation, detailed algorithm flow chart is shown in Figure 2.4. Initial population of models is generated randomly at the beginning of the inversion. The selection process consists of choosing individuals with the best misfit among the population, and generates a new offspring for the next generation. The selected models are then subjected to crossover where individuals of the new generation are randomly paired and exchange a part of their bit string corresponding to each model parameter. The newly generated population undergoes a mutation, where genes of each model are randomly changed to a different value. In the hybrid heuristic search method, the offspring models generated from the parents crossover do not remain automatically in the next generation.

A generation dependent probability is introduced in the crossover to choose new models from current model *(X)* and offspring model *(Y')*. The difference ΔE between the misfits of the offspring and the current models is calculated by:

$$\Delta E = E(Y') - E(X), \qquad (9)$$

This operation principally selects which of the parent model or the offspring has smaller misfit: If the difference of the two misfits is negative, the offspring model survives in the next generation. On the other hand, if the difference is positive, there is a probability P that an offspring model with a large misfit will still be selected in the next generation. The probability is defined by a cooling schedule as similar manner as the SA using temperature that should be decreased with increasing generations as follows:

$$P = exp(-\Delta E/T_g), \qquad (10)$$

Where T_g is the temperature variable at the g^{th} generation based on a cooling schedule. The initial temperature is defined using the simulated annealing relation in equation (11), where c and a are the rates of decrease defined by the user. The rate of the temperature decrease used in our study is similar to that in the SA of Yamanaka (2005) and Takekoshi and Yamanaka (2009) using initial temperature T_0.

$$T_g = T_0 exp(-cg^a), \qquad (11)$$

As the temperature decreases along the computation, the probability of acceptance varies so that only models with a large misfit can frequently be selected in the early stages of the calculation, while such models find it hard to survive in the later iterations.

The difference between the synthetic and the observed waveforms is minimized using the following misfit function:

$$E = \frac{1}{M-1}\sum_{j=2}^{M}\left\{\frac{\sum_{i=1}^{N}\left[D_j^0(t_i)-D_j^c(t_i)\right]^2}{\sum_{i=1}^{N}\left[D_j^0(t_i)\right]^2}\right\}, \qquad (12)$$

where $D_j^0(t_i)$ and $D_j^c(t_i)$ are the observed and calculated waves after the deconvolution. *M* is the number of stations and *N* is the number of data at each station.

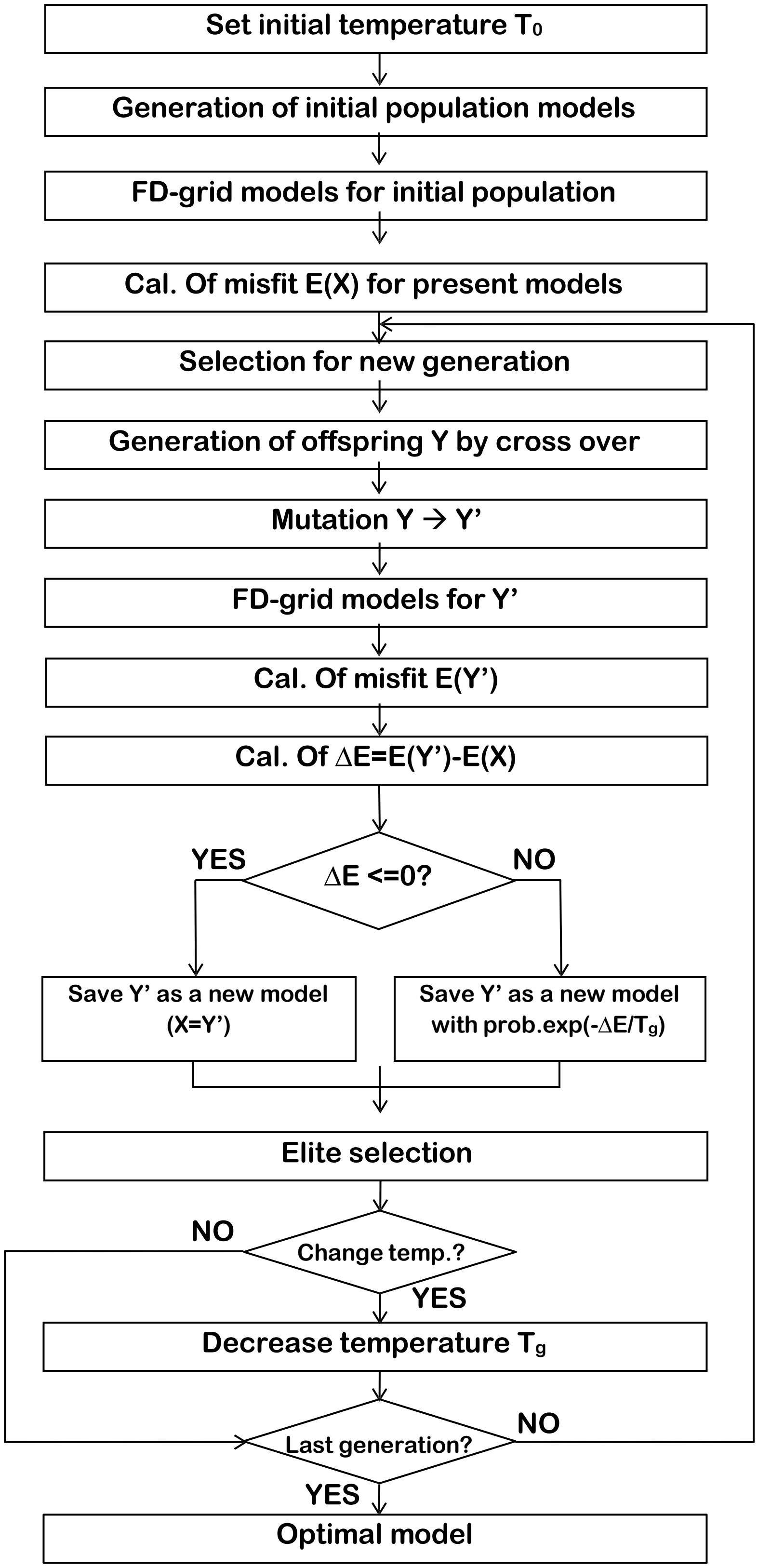

Figure 2.4: Computational flowchart of the hybrid heuristic inversion.

Chapter 3

NUMERICAL EXPERIMENTS

3.1 Proposed numerical models and synthetic data observation:

In order to assess the feasibility of our proposed method, we conducted some numerical experiments in which we prove the effectiveness of our inversion method to properly retrieve 2D shallow soils. Three numerical examples of the inversion representing different soil configurations are conducted. The models are pure elastic soils illustrated in Figure 3.1. The first model (A) is a two layers soil with an irregular layer interface. The model (B) have a lateral shear wave velocity within its surface layer, and the third model (C) is a three layers soil with a blind layer. The aim of these experiments is to assess the ability of our methods to properly determine complex 2D soil profiles which may be difficult to be retrieved using the conventional travel time analysis.

The synthetic data sets are calculated using the FD scheme described above with a meshing of 0.1m and a buffer size of 30 grids, other physical parameters are described at tables of each experiment. The vertical component of the P-SV waves was recorded at 20 receivers covering the whole surface of interest at 1m interval from 0m to 19m from the source point. A point source Ricker wavelet with a central frequency of 50Hz simulates the plank hammering near the surface. The source location is materialized by a black star at location 0m in Figure 3.1. The black dashed box in Figure 3.1 delimits the surface covered by receivers, and areas outside the black dashed line including the lateral absorbing boundaries do not enter the scope of the inversion, and are out of discussion.

Rayleigh wave propagation is significantly related to the medium shear wave velocity, but less influenced by the P wave velocities and densities. Since we focus on the inversion of the S-wave velocities and layer interfaces in our study, we assume the P-wave velocities and densities to be known during the waveform inversion. With these simplifications, only the S-wave velocities and the depth parameters of the interface making each layer of the soil remain unknown. P wave velocity is then calculated by multiplying S-wave velocity at each block by 1.7, and the basement velocity by 2.0.

Considering the parametric study of the algorithm by Yamanaka (2007), and the inversion results of Takekoshi and Yamanaka (2009), the initial population is set to 20, the crossover rate and mutation are 0.7 and 0.01 respectively. For the SA parameters, the initial temperature of inversion is 100, the temperature decline function are respectively c=1.0 and a=0.7.

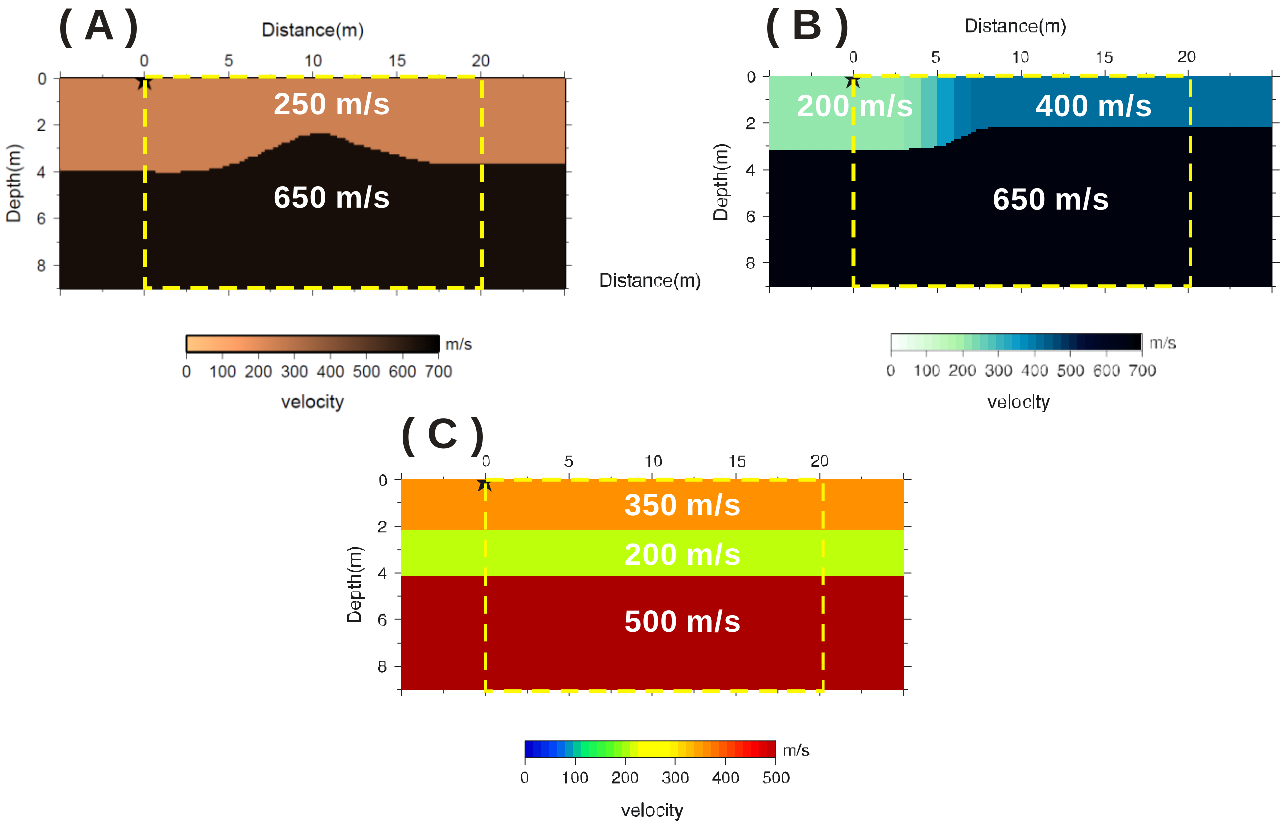

Figure 3.1: Numerical models used in experiments.

Model A, two-layers soil with irregular interface.

Model B, two-layer soil with strong lateral velocity gradient.

Model C, three-layer soil with blind layer.

3.2 Inversion of the two layers model with irregular interface:

The soil model with an irregular interface in Figure 3.1A consists of a surface layer with a constant shear wave velocity of 250m/s, laying over a basement with a shear wave velocity fixed to 650m/s. The model includes a smoothed irregular interface uplifting the basement at depths from 4m to 2m along a 10m distance as shown in Figure 3.1A. The physical parameters of the soil model are detailed in Table 3.1. The surface layer was divided into 30 blocks with unknown velocities and 30 depth parameters. However only 22 blocks covered with the receivers on our survey line of 20m will be considered in our interval.

Table 3.1. Physical proprieties and inversion settings of the model A.

Layer	**True values of the model**			**Inversion Search Limits**		**Inversion parameters**
	Vp(m/s)	*Vs(m/s)*	*ρ(kg/m^3)*	*Vs (m/s)*	*Depth parameter (m) 'Pk'*	
1	425	250	1600	100-400	1-5	Generation = 100 Population= 20 Mutation Rate= 0.01 Crossover rate= 0.7 Initial temperature= 100
2	1300	650	2000	650 (fixed)	-	

The data processing for the observed waveforms are shown in Figure 3.2. The raw observed time series recorded at 20 stations for a duration of 0.15s are illustrated in Figure 3.2a. In order to perform the source deconvolution previously described, we transform our signal to the frequency domain, as shown in Figure 3.2b. The Fourier spectrum of each station is divided in the frequency domain by that of the reference station (first station) displayed in the figure in black. The resulting from the division in frequency is the spectral ratio illustrated in Figure 3.2c, and filtering was used to keep only frequencies of interest. A cosine-type band-pass filter of 10Hz-200Hz was applied to the spectral ratio at Figure 3.2c, and we transformed back the whole signal to the time domain in order to obtain the deconvolved filtered waveforms in Figure 3.2d.

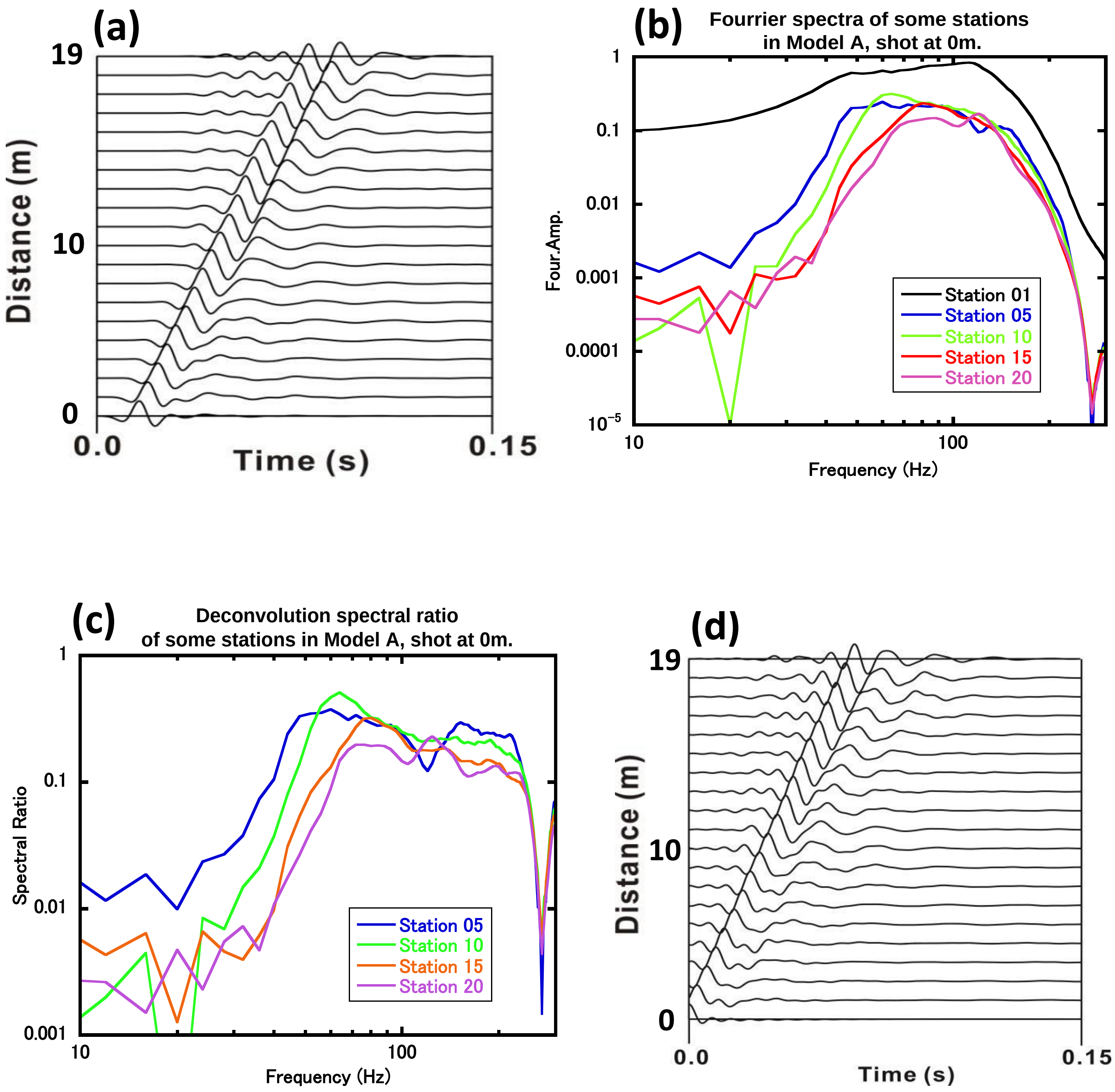

Figure 3.2: Pre-processed observed data.

(a): Observed waveforms recorded at 20 stations in Model A.

(b): Fourier spectra of some recordings from Model A.

(c): Spectral ratio of some stations issued from the division in frequency of Model A recordings.

(d): Deconvolved filtered waveforms of Model A.

Since many random numbers are used in the hybrid heuristic search inversion, the final results of the misfit function and the inverted parameters can be more or less dependent on the random numbers used for each execution. In order to avoid effects related to the random numbers, we conduct 30 different inversions with different random values generated for each execution, where 100 iterations (generations) were considered for each inversion. Then, we averaged the results from all inversions to obtain a final optimal model.

The results of the inversion are illustrated in Figure 3.3. Comparison between the observed waveforms and the inverted ones is shown in Figure 3.3a. The comparison shows successful results, with a good similarity between the objective waveforms in black solid lines and the final inverted waveforms with dashed lines, and this similarity shows that information about the soil structure and shear wave velocity of the surface layer encrypted in the signal were well reproduced through the inversion process. The final averaged model issued from the 30 different inversions in Figure 3.3c has significant similarities with the target model in Figure 3.3b: The surface layer velocity is attributed an averaged S wave velocity of 251m/s, while the model standard deviation (MSD) of the blocks velocities of the final averaged model is 2.52m/s underlying a homogeneous velocity distribution in the layer. The shapes of the layers interface indicate a clear uplifting of the basement from a depth of 4m to 2m.

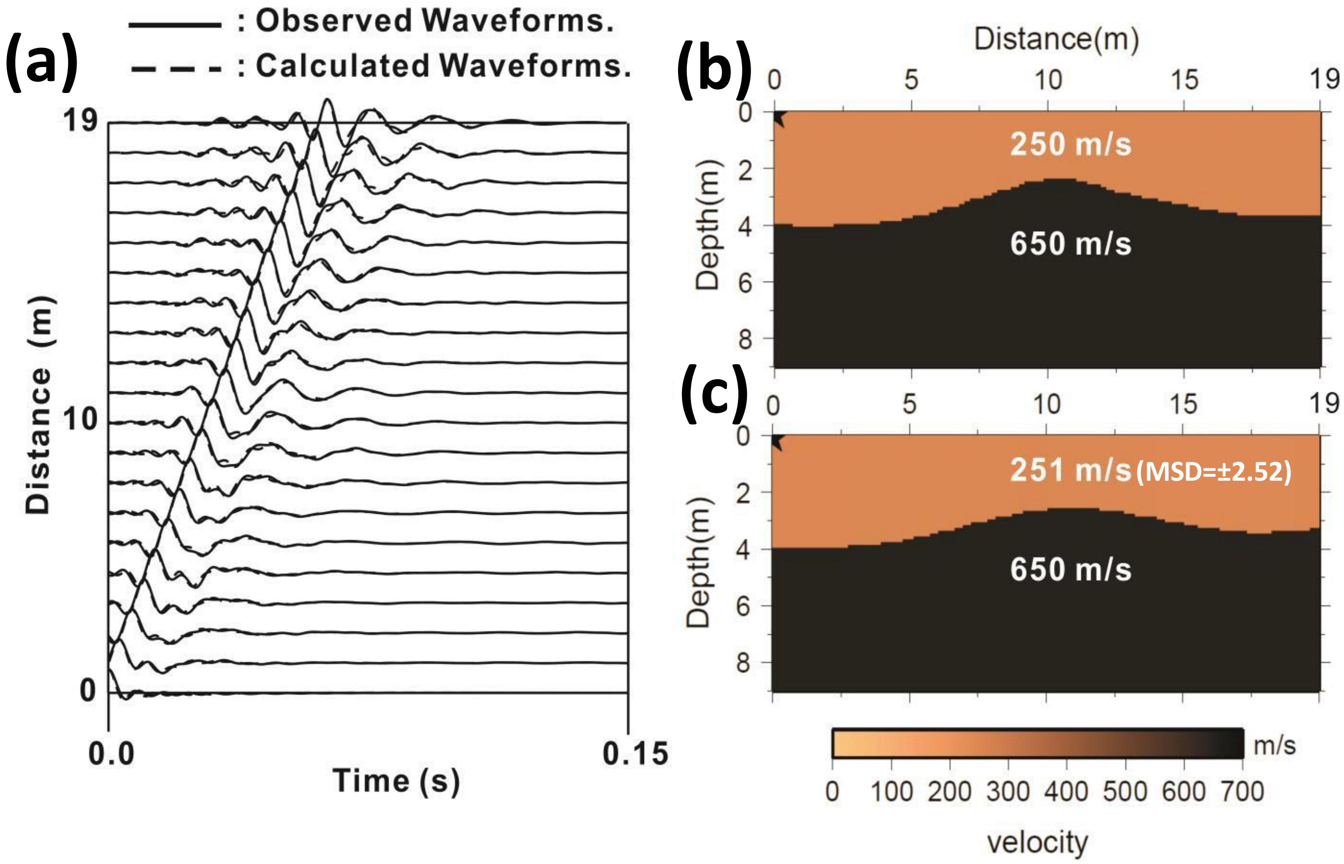

Figure 3.3: Inversion results of Model A.

(a): Comparison of the observed waveforms (solid line),

and the inverted waveforms (dashed lines). (b): Target Model A.

(c): Averaged inverted soil model from 30 inversions.

3.2.1 Error estimation of inversion:

For a more significant analysis of the inverted results, we estimated the variation of the inverted depth parameter and the velocities at each block from the 30 different inversions. This block standard deviation (BSD) is different from the model standard deviation (MSD) previously stated, the BSD estimate the velocity variation of each block from the different inversions, while the MSD estimates the velocity variation between the blocks in the final averaged model. From MSD we can see inhomogeneity of the layers, and BSD can be used to estimate stability of the inversion results. The values of the depth and the velocity standard deviations from the 30 inversions are shown at Figure 3.4.

Comparison between the inverted layer interface in a dashed line and the target model layer interface in a black solid line shows a faithful reproduction of the basement irregularity. The depth and the slopes of the smoothed interface were reproduced with a satisfactory level of similarity with a small standard deviation of the interface depth, except for the part located at the opposite side of the source at distance from 15m to 19m, where the exact depth is slightly distorted. This inaccuracy can be due to the inexistence of receivers beyond 19m.

The variation coefficients of the block velocities from these 30 inversions have values smaller than 0.01 along the profile, while the blocks located far from the source have slight velocity inaccuracies. The small standard deviation values from the 30 inversions for each block along the profile reflect the stability of our algorithm on properly retrieving the two-dimensional irregular soil profile with a single shot to a certain extent. The experiment also revealed a small loss on accuracy at the areas located far from the source, resulting in some inaccuracies on properly identifying the exact block velocities and depth parameter at the far field.

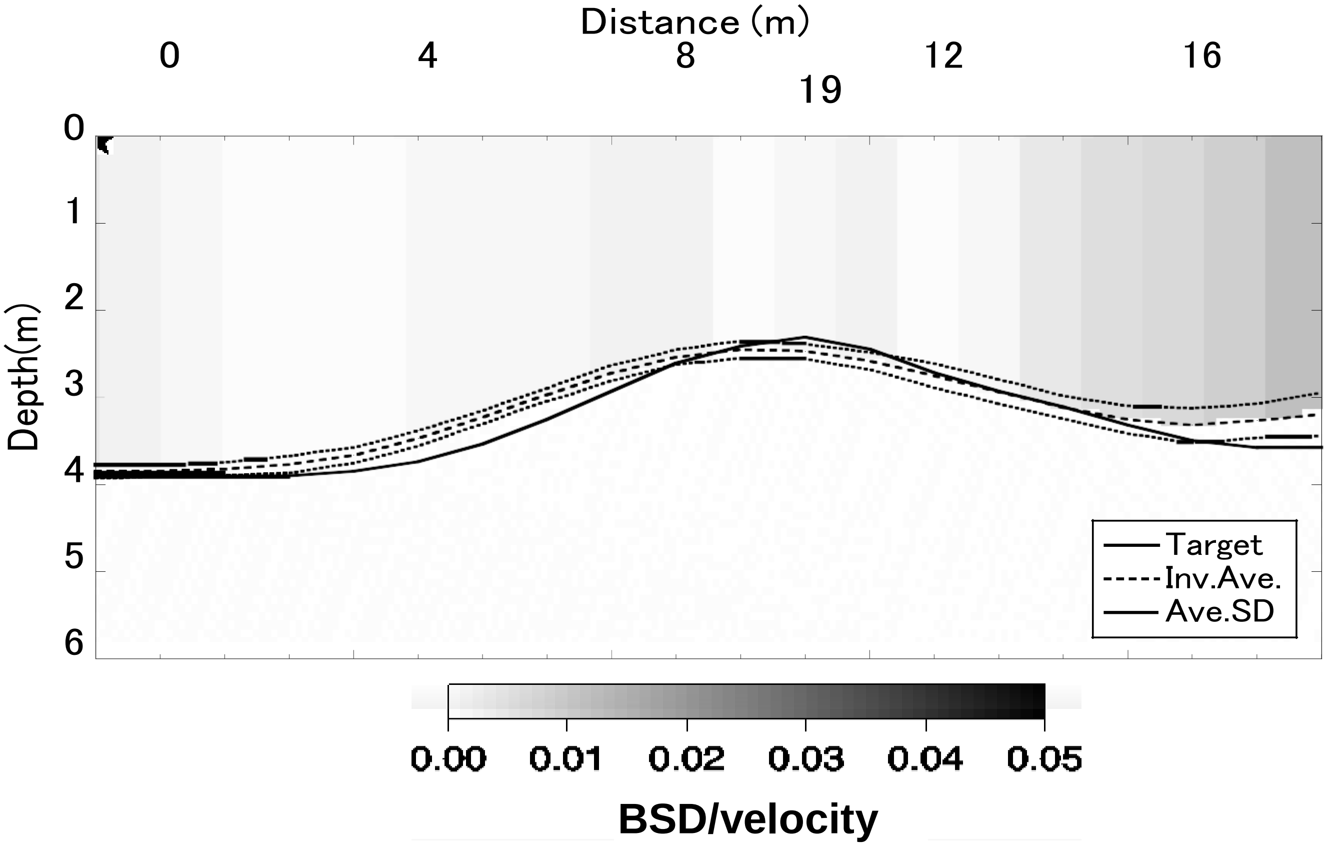

Figure 3.4: Error estimation for depth and velocity determination at each block from 30 inversions.

The target layer interface is shown by solid black line, the inverted averaged layer interface as a dashed line, and the standard deviation of the depth parameter as a dotted line.

3.2.2 Number of inversions effect on the final averaged model:

In order to assess the stability of the inversion, and choose appropriate number of inversions to be considered as the final averaged model, we conducted a quantitative analysis for the block parameters from the 30 inversions. Figure 3.5 shows the cumulative values of the inverted velocities and the depth parameters located at 5m, 10m and 20m along the profile. The block velocities in Figure 3.5a show constant values in the 30 different inversions for the blocks located at 5m and 10m with the values very close to the target velocity of 250m/s from the first inversion. However, the block located at the extremity of the profile has some difficulties in convergence until the 10th inversion, where the velocity value settles at 250m/s. Similar observation can be pointed out for the depth parameters in Figure 3.5b, where the depths at 5m and 10m are unchanged between the first and the last inversions, while the block at the opposite side of the source (20m) requires at least 10 inversions to properly reach a stable depth value.

From this analysis we conclude that the number of inversions for final model by averaging does not have a big influence on the inverted parameters except for the blocks located very far from the source if we execute more than 10 inversions for average. Thus, ten inversions are sufficient to average a final optimal model through this research.

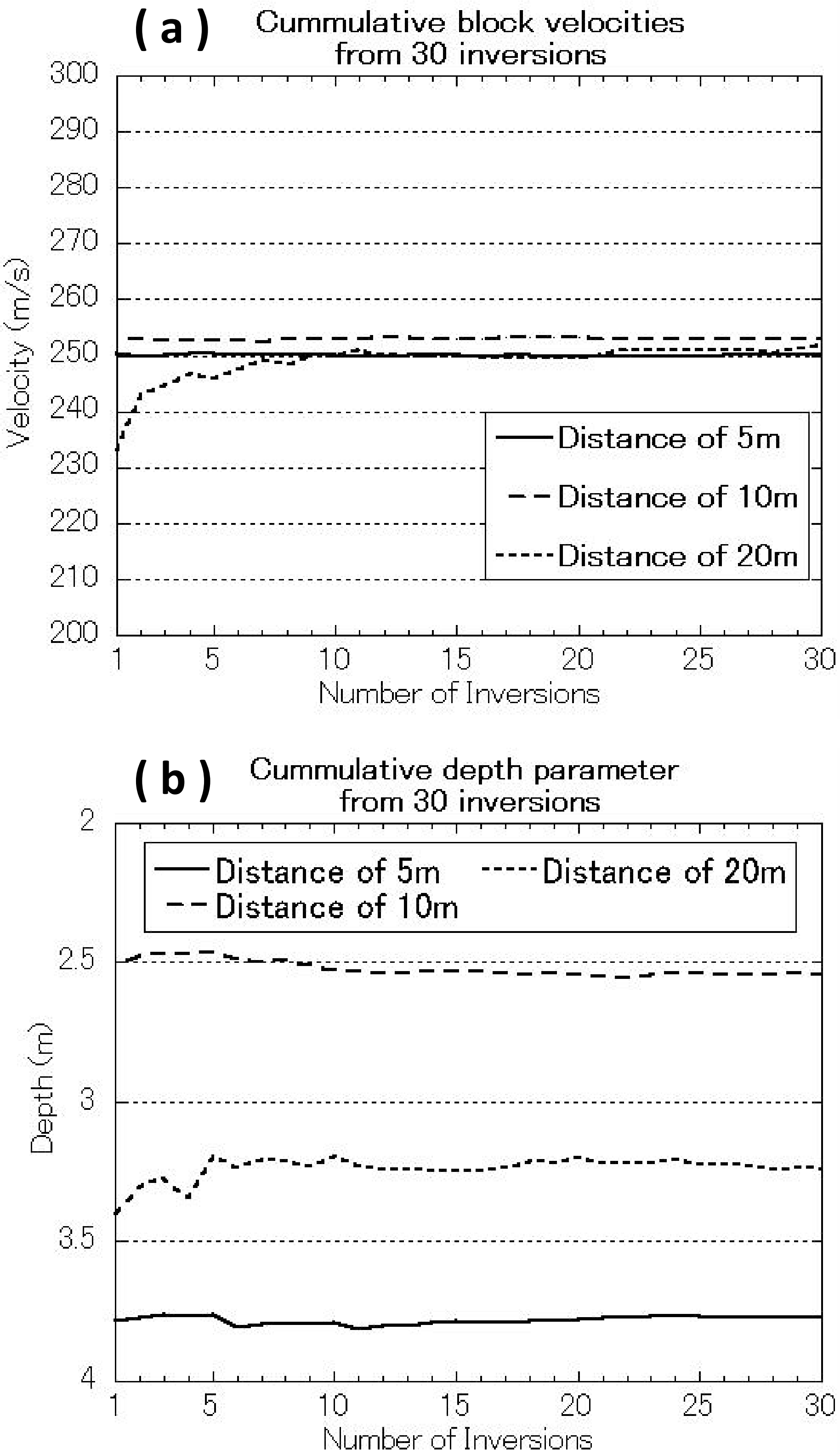

Figure 3.5: Quantitative analysis of the inverted parameters.
(a): Cumulative velocities from 30 inversions at distances of 5m, 10m, and 20m.
(b): Cumulative depth from 30 inversions at distances of 5m, 10m, and 20m.

3.3 Parametric study of inversion:

In order to underline the effect of the different parameters that can influence results of the inversion, we conducted a parametric investigation considering Model A. We estimated the effect of velocity impedance ratio, block numbers at each layer, and inversion without fixing the basement velocity.

3.3.1 Velocity impedance ratio:

The propagation of the surface waves in a vertically heterogeneous medium is particularly sensitive to S-wave velocity contrast in the propagated medium. The dispersive character of Rayleigh waves becomes more or less prominent depending on to the velocity impedance ratios between soil layers. Soil models with high velocity contrast enhance the dispersion of Rayleigh waves, while low velocity contrast models restrict it.

To assess the robustness of our method on properly inverting irregular shallow soil with different velocity impedance ratios between layers and basement, we conducted similar experiments using different layer velocities. In the first experiment, we inverted the model A using a shear wave velocity of 250m/s at the surface layer and a basement velocity of 650m/s. The basement velocity is 2.6 higher than the surface layer velocity.

In this experiment, we decreased the velocity contrast between the surface layer and the basement to 1.3 by increasing the velocity of the surface layer to 500m/s as illustrated in Figure 3.6b. We conducted 10 different inversions using similar parameters to the previous experiment, except for the velocity search limits that we changed to: 400m/s – 700m/s.

The final averaged model from 10 different inversions is illustrated in Figure 3.6c. Inversion shows a good correlation between the target model and the inverted model despite the very low velocity contrast between layers, proving the ability of our method to correctly retrieve layer interfaces in low velocity contrast mediums.

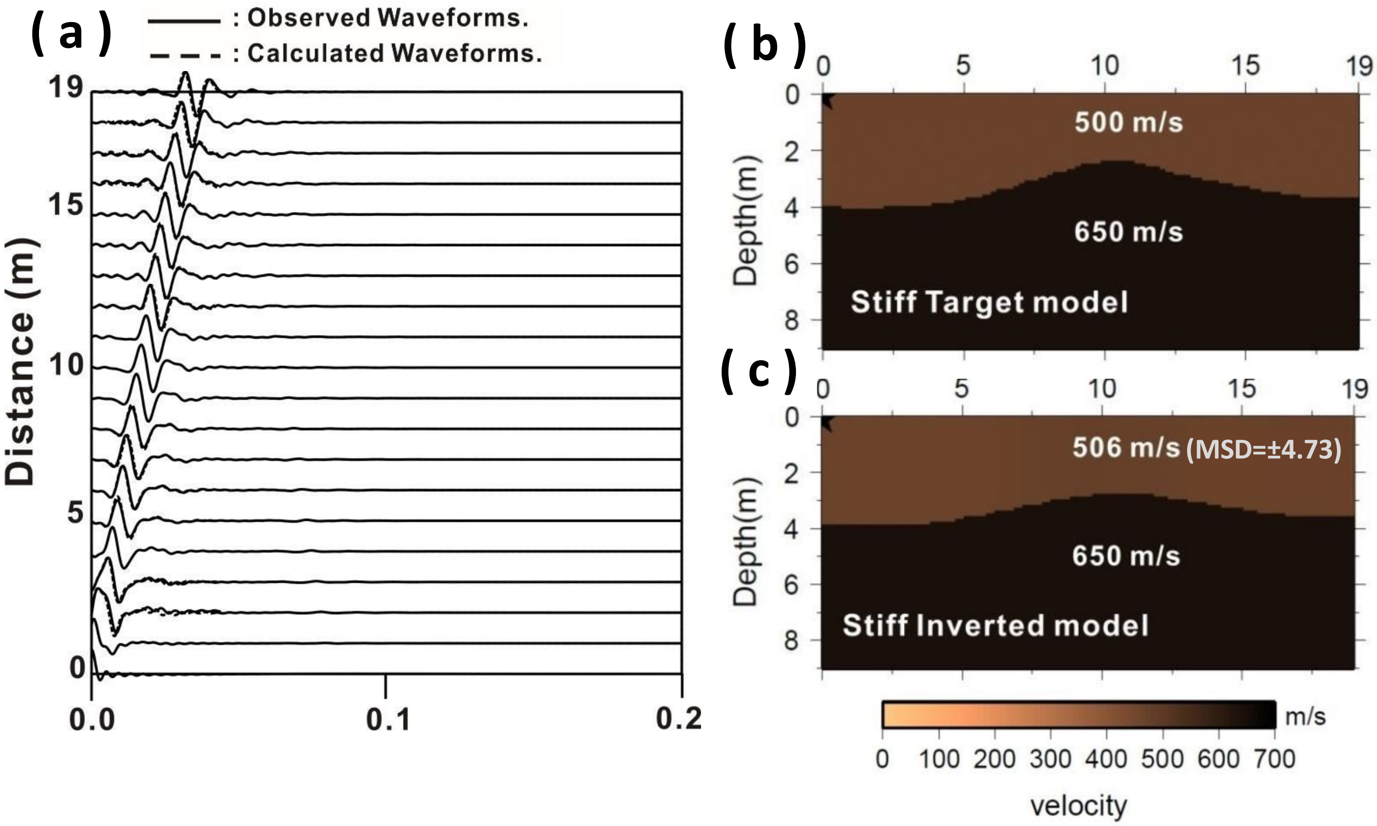

Figure 3.6: Inversion results of the stiff Model A.
(a): Comparison of the observed waveforms (solid line),
and the inverted waveforms (dashed lines). (b): Stiff target Model.
(c): Averaged inverted soil model from 10 inversions.

3.3.2 Block size and number:

As explained in the methodology, our numerical soil model is built by specific blocks determined by the users. Tuning the numerical model with inappropriate block number, may influence the inversion results for models with irregular interfaces. In order to illustrate and estimate the effects of assumed block numbers upon the inversion, we compared inverted results from the same numerical experiment of model A with an irregular interface using different blocks configuration. We divided the target model to 10 and 60 blocks and basis functions, and used the same inversion parameters previously described in Table 3.1. Ten inversions and a single shot at 0m were considered for each case.

The results of the inverted 2D soil models are summarized in Figure 3.7. The inversion results show that increasing the block number to 60 in Figure 3.7e did not affected the inversion results, where the model has very similar interface shapes to the original model. However, using a smaller number of blocks (10 blocks) in Figure 3.7d lead to a significant distortion in the shapes of the layer interface between 5m and 15m of the inverted model, this inaccuracy is due to the large size of the blocks with respect to the dimensions of the interface irregularity.

Another important observation is that the block number had a small effect on properly retrieving the shear wave velocity in all three cases. Regardless of the number of unknown parameters to be inverted, the S-wave velocity of the layer was properly inverted. Thus, the block number is more likely to affect the estimation of layer interfaces rather than of the shear wave velocity when the block size is exaggerated.

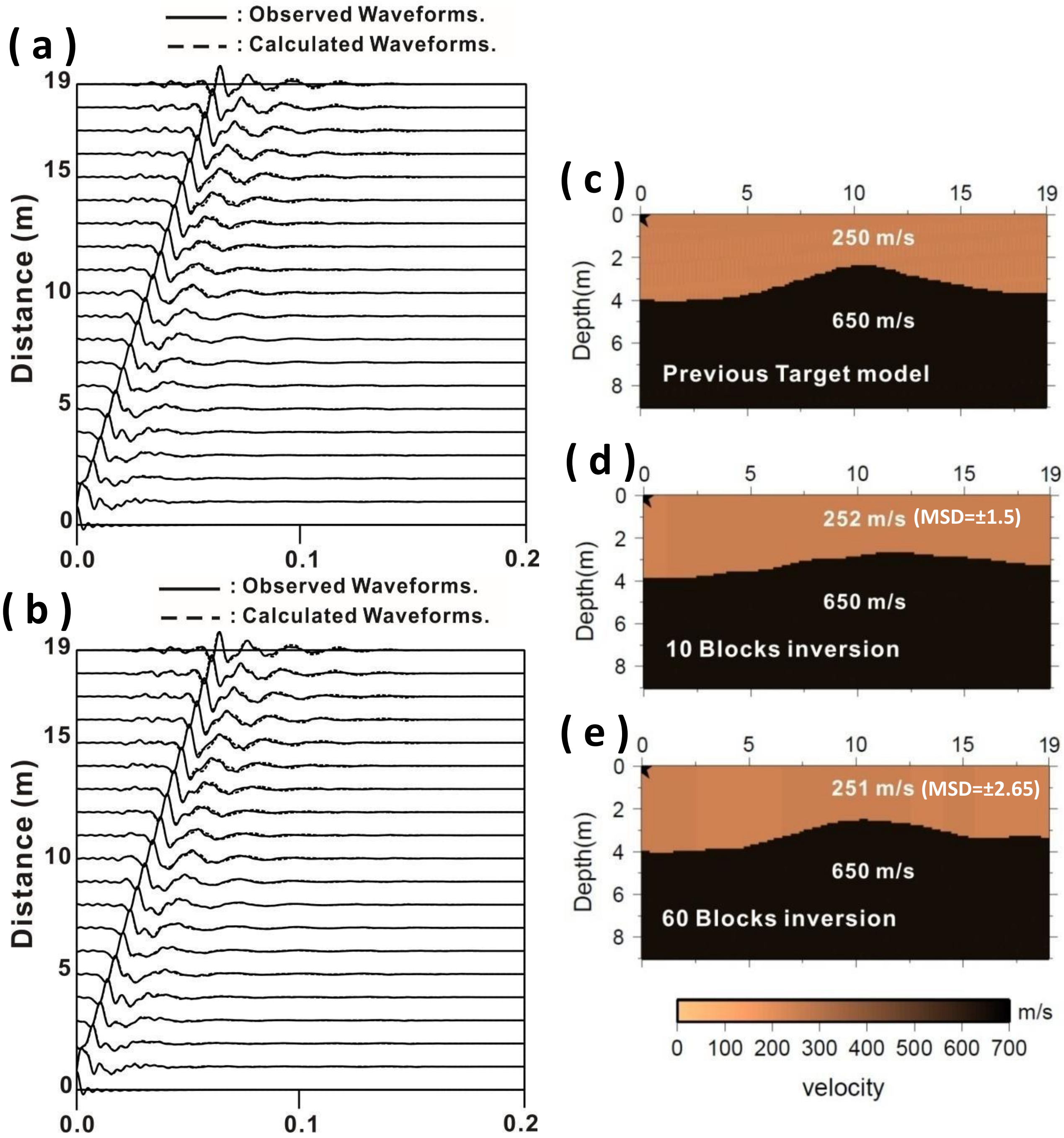

Figure 3.7: Inversion results of the Model A with different block sizes.

(a): Comparison of the observed and inverted waveforms of the 10 blocks model.

(b): Comparison of the observed and inverted waveforms of the 60 blocks model.

(c): Target model.

(d): Averaged inverted model using 10 blocks.

(e): Averaged inverted model using 60 blocks.

3.3.3 Input layers misidentification:

Another parameter that needs to be considered is the number of layers considered for model tuning. During the inversion of the Model A, we explicitly chose the same number of layers as the target model. However, we would like to evaluate the performance of our inversion when we input different number of layers for a given soil model. For this purpose, we used the observed waveforms acquired on Model A, and attempted to obtain a 2D soil profile including a thin layer near the surface.

In other words, we try to invert waveforms of the two layered Model A with an assumption of three layers. Each layer was divided into 30 blocks with the velocity search limits set to: 150m/s-400m/s. The depth search parameter of the first layer interface was 0.5m-1.5m, while that of the second layer interface was 2m-5m. An averaged model from 10 different inversions is shown in Figure 3.8d. In the inverted model, the velocity of the first layer was estimated to 265m/s with a flat interface at around 1m depth, while the second layer had a velocity of 251m/s, clear basement irregularity can be noticed in the inverted model. However, the shapes of the basement are not very accurate. This result shows that despite using different layers input, the velocity of both layers can be averaged to a simple layer with a shear wave velocity of 258m/s, which is not very far from our target velocity of 250m/s.

From this experiment, we understand that tuning our inversion with an inappropriate number of layers will not have a significant effect on velocities; it can however corrupt the real shapes of the layer irregularities.

Therefore, it remains important to tune the model with an appropriate number of layers using existing data of the area of interest, or other one-dimension geophysical exploration technique, for misidentifying the layer configuration influences the inversion results and their effect may differ depending on the soil configuration.

3.3.4 Inversion with unknown basement velocity:

Fixing appropriate basement velocity is a common problem for both active and passive surface wave methods. In all experiments conducted so far, the basement was assumed to be known and fixed to 650m/s. In the next experiment, we assessed the potential of our inversion when both the target layer and basement velocities were unknown. Model A was inverted with some modifications of the inversion settings of Table 3.1. The velocity search limits for both basement and the velocity were set to: 150-700m/s, while the depth search limits were kept between 1m to 5m. We increased the number of generations from 100 to 300 for each inversion, to give the algorithm plenty of time to find an optimal model. Figure 3.8e shows the final averaged model from 10 different inversions, where the layer interface was successfully reconstructed and the basement velocity was slightly underestimated to 632m/s.

The miss-approximation of the basement velocity was counterbalanced by an over-estimation of the surface layer at 267m/s. This difference in the velocities between the basement and layer is a common problem known by the FWI community as the non-uniquness of the solution. The FWI is an ill-posed problem, meaning that an infinite number of models matches the data (Virieux et al, 2009). For this reason, we always use fixed values for the basement in our method to reduce the non-uniqueness of our solution. As for earthquake engineering, bed rock is fixed for a layer with Vs between 400m/s to 700m/s.

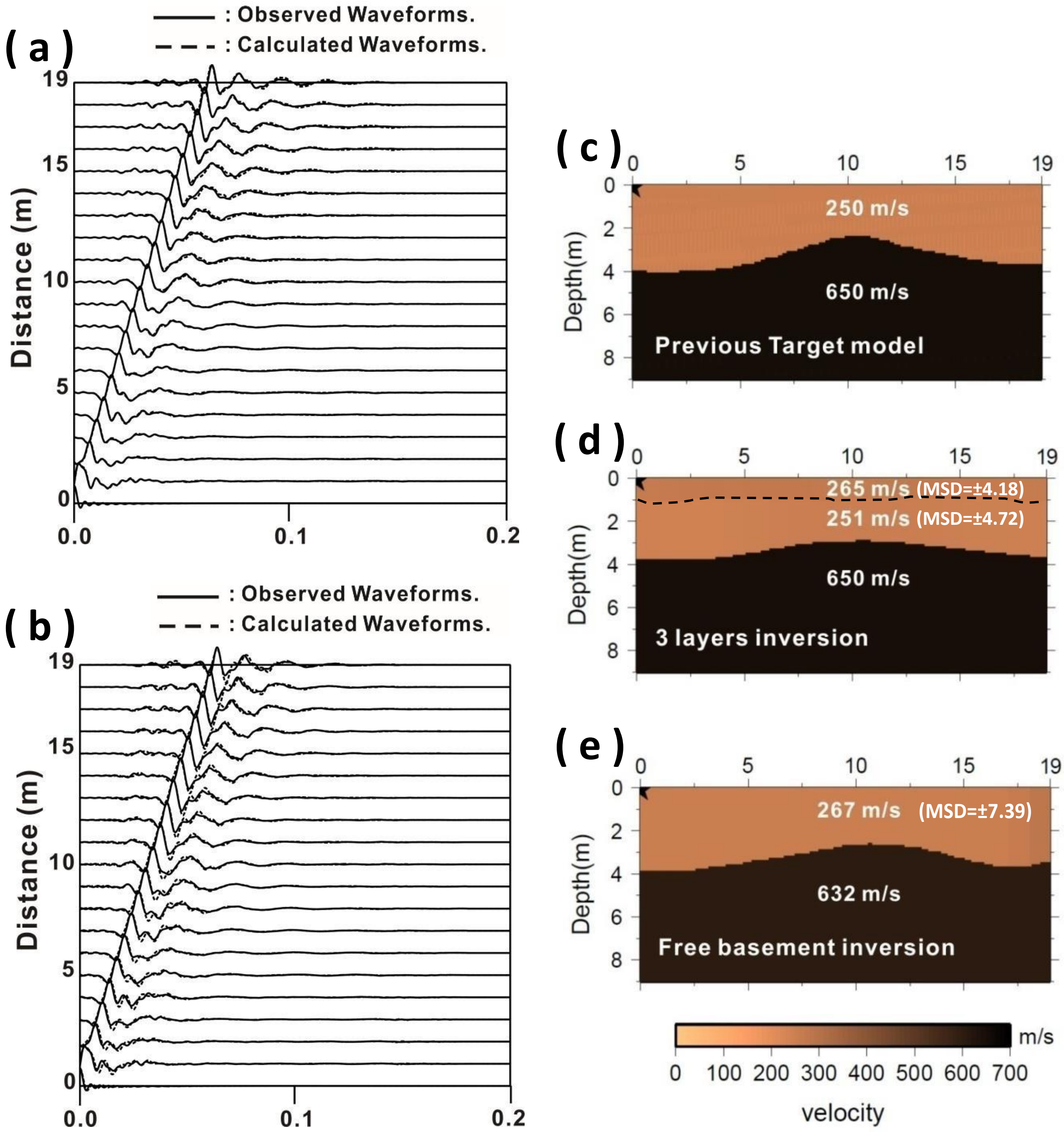

Figure 3.8: Inversion results of the Model A with different layer numbers and unknown basement velocity.

(a): Comparison of the observed and inverted waveforms of the 3layers model.

(b): Comparison of the observed and inverted waveforms of the undetermined basement velocity model.

(c): Target model.

(d): Averaged inverted model using 3 layers.

(e): Averaged inverted model including basement inversion.

3.4 Inversion of the two layer model with strong lateral velocity difference:

The role of lateral variation along the propagation path can be particularly relevant and deserves special attention, if the wave path is horizontally heterogeneous, it can cause perturbations on the observed phase velocity of the surface waves (Strobbia and Foti, 2006). Thus, the 1D assumption can be misleading if the lateral velocity is not accounted for (Lin and Lin, 2007). Several authors proposed methods to remedy the presence of lateral variations in the targeted soil model (Shitvelman, 2003., Strobbia and Foti, 2006., Boiero et al, 2011), but the lateral variation in surface-wave analysis still represents a problem and still remains an important target for exploration applications (Socco et al, 2010).

3.4.1 Noise-free inversion:

The soil model in Figure 3.9b is composed of a surface layer with a strong shear wave velocity variation from 200m/s to 400m/s at 5m distance, laying over a basement of 650m/s. The model also has a small slope between 4m and 7m raising the basement depth from 3m to 2m. The physical parameters of the soil model are shown in Table 3.2. We will prove the efficiency of our method to a 2D shallow soil with a strong lateral velocity.

Table 3.2. Physical proprieties and inversion settings of the inhomogeneous velocity model.

Layer	**True values of the model**			**Inversion Search Limits**		**Inversion parameters**
	Vp(m/s)	*Vs(m/s)*	*ρ(kg/m³)*	*Vs (m/s)*	*Depth parameter (m) 'Pk'*	Generation = 200 Population= 20 Mutation Rate= 0.01 Crossover rate= 0.7
1	340-680	200-400	1600	150-500	1-4	Initial temperature= 100
2	1300	650	2000	650 (fixed)	-	

Because of the complexity of the model, we gave the algorithm plenty of time to find the most adequate solution by increasing the number of generations to 200. Ten inversions with different random numbers were conducted, and the inversion results are summarized in Figure 3.9. The inversion shows very good fit between the observed waveforms and the inverted waveforms in Figure 3.9a. The inverted 2D model in Figure 3.9c highlights a successful reconstruction of the lateral velocity gradient at 5m and the good reproduction of the interface slope at the same distance, rising the basement from 3m depth to 2m.

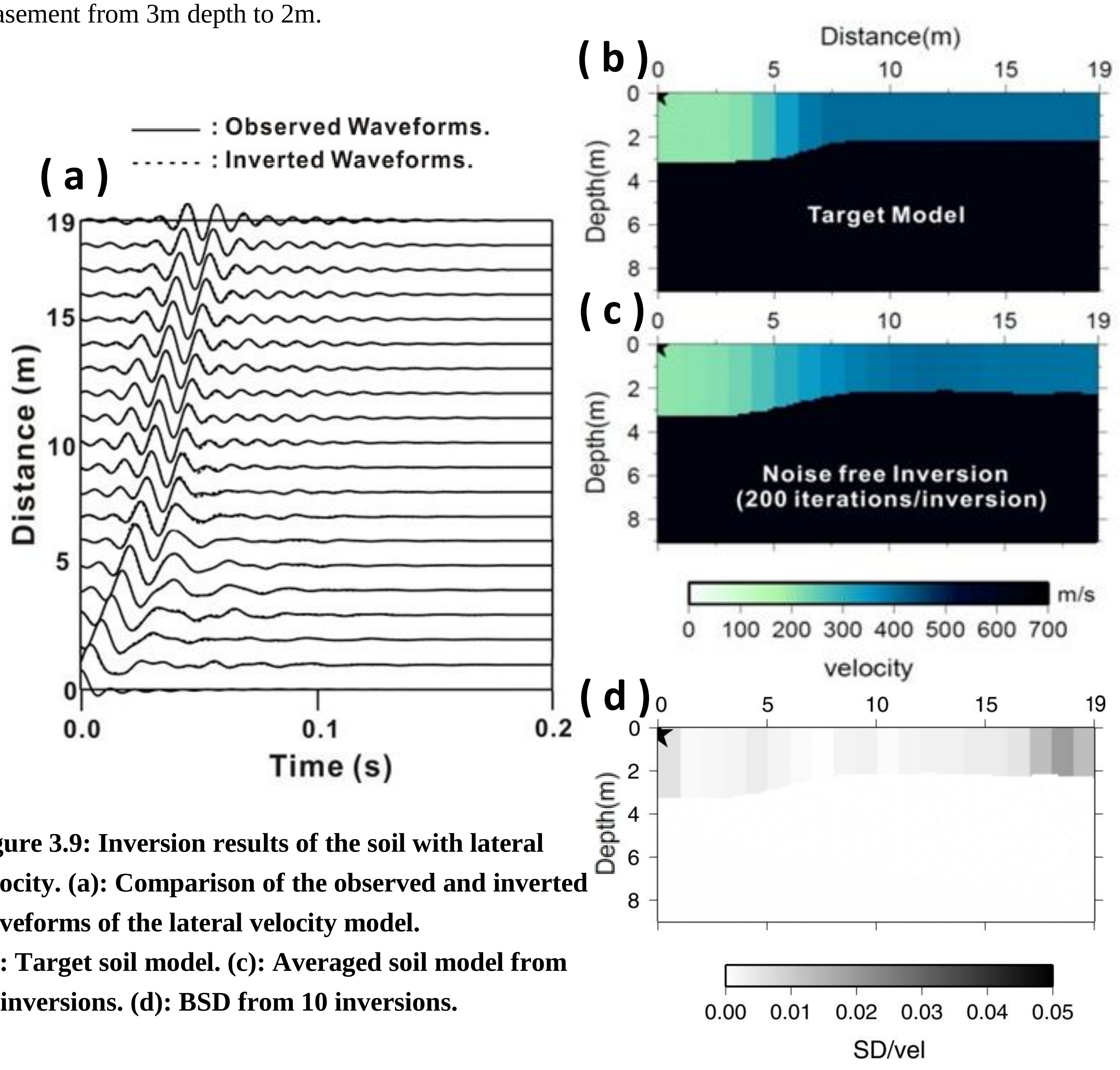

Figure 3.9: Inversion results of the soil with lateral velocity. (a): Comparison of the observed and inverted waveforms of the lateral velocity model. (b): Target soil model. (c): Averaged soil model from 10 inversions. (d): BSD from 10 inversions.

3.4.2 Parameters evolution along Inversion:

To understand the correlation between the models updating with respect to the evolution of the misfit along inversion, we plotted the minimum misfits at each generation from 10 inversions obtained on the noise free experiment of the Model B. The minimum misfit corresponds to the difference between the observed waveforms and the waveforms issued from the best model at each generation along the inversion.

The minimum misfits derived at each generation from the 10 inversions are shown in Figure 3.10a. It should be noted that the minimum misfits have different evolutions from each other because of different details in the convergence with increasing generation (Yamanaka et al, 2009). All inversions start with different initial models generated randomly, and converge to an optimal solution with small misfits at the end of iterations.

To illustrate the 2D soil modeling according to the decrease in the misfit function, we showed the soil model at different stages of inversion number 5. The initial model randomly generated is shown with corresponding waveforms in Figure 3.10b, the block depth and velocities of this model are very chaotic generating a model with a misfit of 1.98. After 100 generations, the misfit is brought down to 0.014 and the soil model starts to take shape with a clear lateral velocity gradient at 5m, as illustrated in Figure 3.10c, however some imperfections remains in the basement slope shape. Finally the model takes its most optimal shape in Figure 3.10d, at generation 200 where the velocities as well as the basement slope was successfully resolved, giving very similar model to the target with a misfit of 0.011.

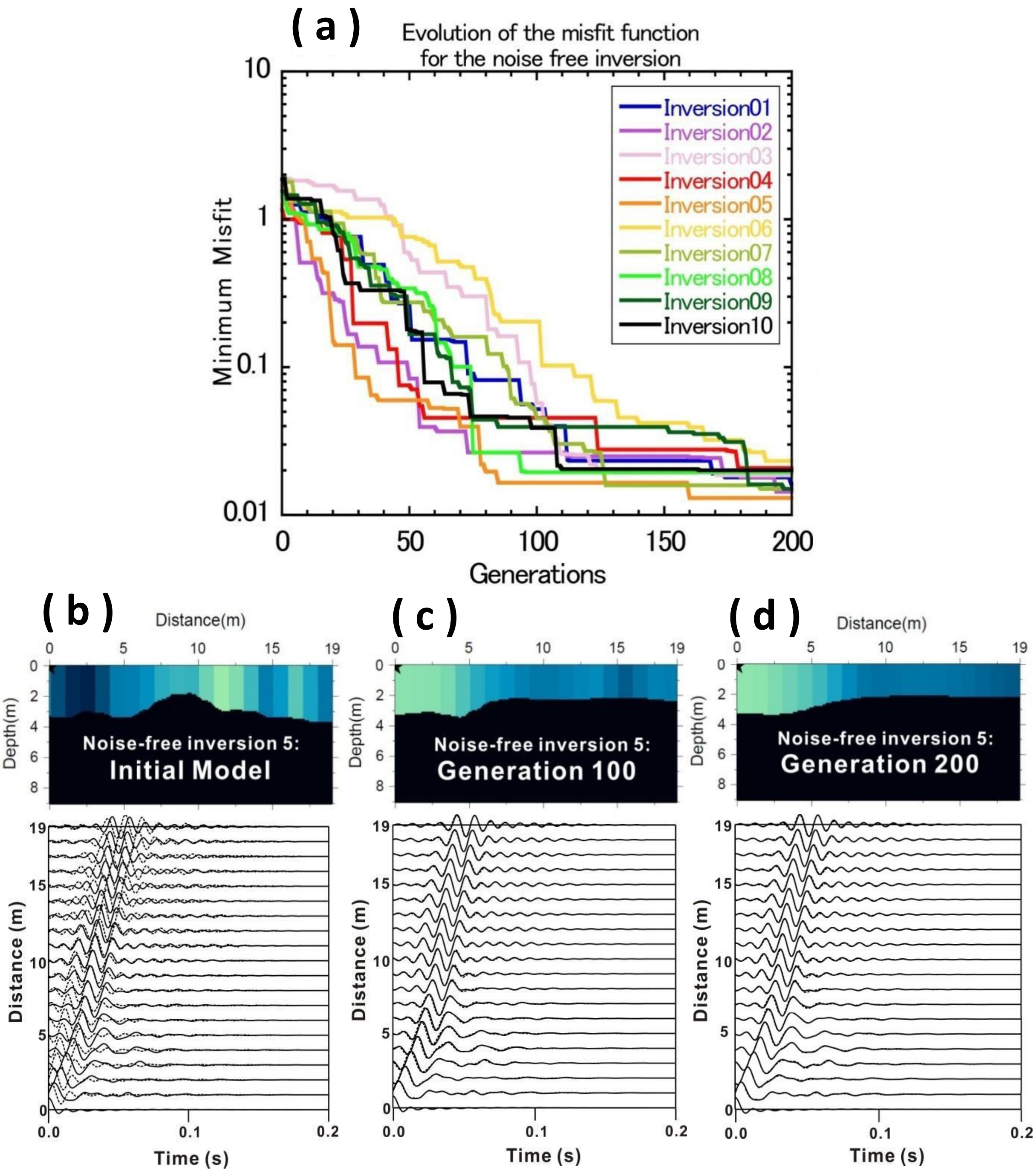

Figure 3.10: Inversion details of the noise-free soil Model B.
(a): Variation of the minimum misfit at each generation from 10 inversions.
(b): 2D initial model randomly generated at inversion 5 and corresponding waveforms.
(c): 2D soil model at generation 100 of inversion 5 and corresponding waveforms.
(d): 2D soil model at generation 200 of inversion 5 and corresponding waveforms.

3.4.3 Block size and number:

To underline the effect of block size on layers with inhomogeneous velocity, we conducted similar experiment previously described for the Model A, where we inverted noise free waveforms using soil configuration of 10 and 60 blocks and basis functions. Ten inversions were considered for each configuration, and results were compared in Figure 3.11. Figure 3.11b shows averaged inverted model considering 10 blocks from the 10 inversions, the inversion shows that despite the large block size, the velocity transition zone at 4m was reproduced, however similarly to the previous model; the basement irregularity was significantly distorted due to the large block size with respect to the slope irregularity. The inversion using 60 blocks in Figure 3.11c also show a good reconstruction of the lateral velocity transition, as well as good reconstruction of the basement irregularity.

For a better understanding of the velocity transition reconstruction from the different models, we compared the target block velocities with the block velocities obtained from the 10, 30 and 60 blocks models in Figure 3.11a. This comparison show that the velocity transition zone was well reproduced with the 30 blocks and the 60 blocks inversion model, respectively in red and blue dashed lines. However, the 10 blocks inversion, alters the interface irregularity and significantly distorts the velocity transition because of the block size. From this comparison we understand that unlike homogeneous velocity layer models, using large block sizes can affect inverted model for soils with strong inhomogeneous velocity variation.

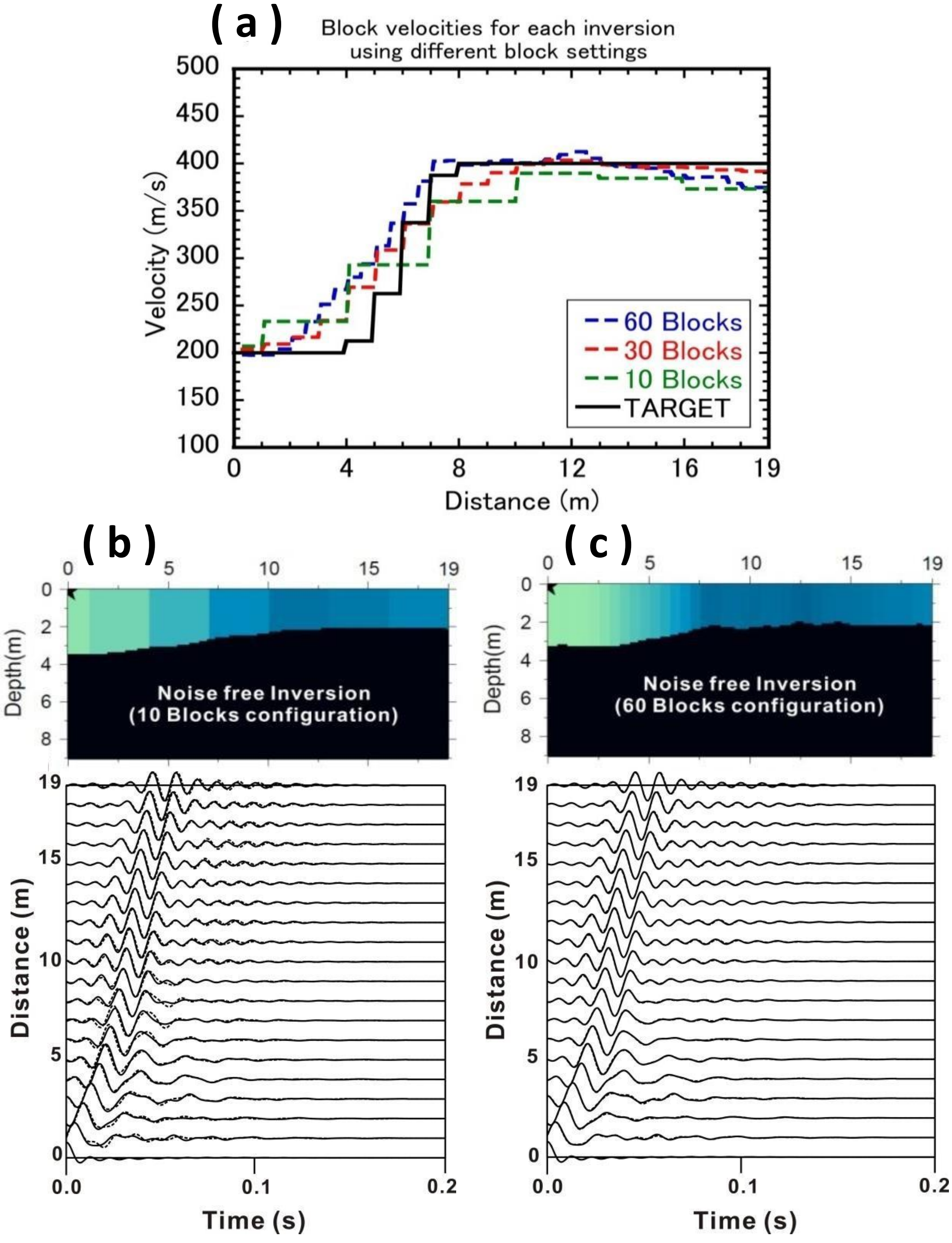

Figure 3.11: Block dimension analysis for Model B.
(a): Comparison of the interface reconstruction from the different block settings,
Where the target model is represented by a black solid line, 60 blocks model in blue dashed line, 30 block model in red dashed line, and the 10 blocks model in green dashed line.
(b): Averaged inverted model using 10 blocks with respective waveforms comparison.
(c): Averaged inverted model using 60 blocks with respective waveforms comparison.

3.4.4 Noisy inversion:

The numerical experiments discussed previously were all conducted in a noise free synthetic data, the target waveforms were free from any perturbation liable to affect the inversion. For a more realistic approach, it is very important to evaluate our inversion in noisy environments. A synthetic white noise was calculated in the frequency domain using the spectral amplitudes of each station. In this experiment we calculated white noise with spectral amplitudes of 3% from the maximum spectral amplitudes for each station, and included it in the signal in time domain before the source deconvolution.

To illustrate the noise implementation on the waveforms at a given station, we plotted the signal including 3% of white noise in Figure 3.12a showing a significant noise to signal ratio. The comparison between the deconvolved waveforms of the noisy signal (black solid line) and the deconvolved noise free signal at station 6 in Figure 3.12b shows that distortions due to noise implementation remains in our signal despite the deconvolution and filtering.

Results of the noisy inversion are summarized in Figure 3.13. Comparison of the noisy waveforms with the inverted waveforms in Figure 3.13a also shows a good correlation between the main arrivals in the signal. The 2D model from these noisy data is illustrated in Figure 3.13c. Despite the noise corruption of our signal, the lateral variation of the velocity was detected and the lateral velocity gradient clearly appeared in our profile at 5m distance. However, the slope at the interface was reconstructed with some inaccuracies due to the noise ripples in the signal. Thus, the noise can more or less affect the reconstruction of the interface shapes rather than the velocities.

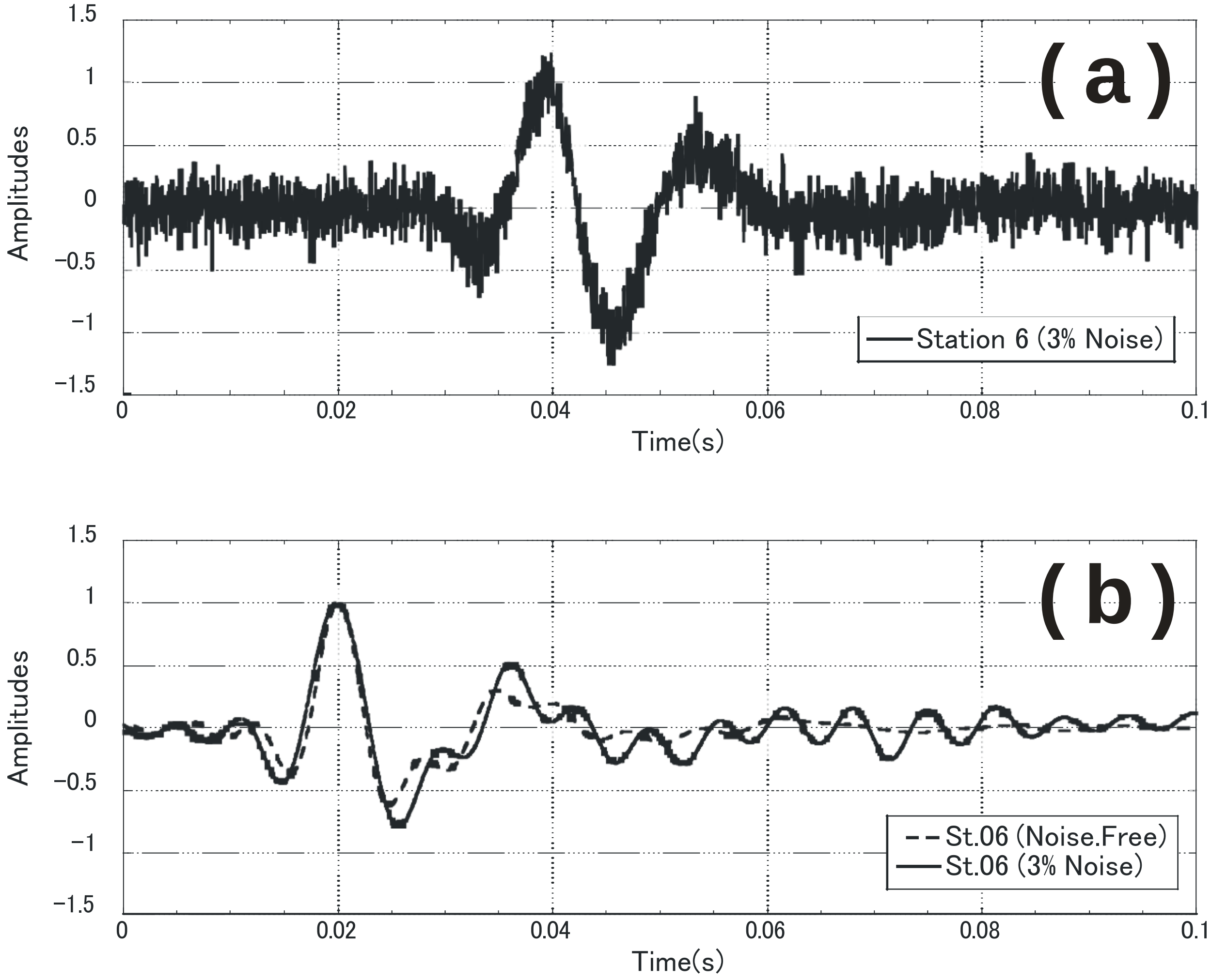

Figure 3.12: White noise implementation in station 6.
(a): Noisy raw signal at the station 6.
(b): Comparison between noisy (solid line), and noise free (dashed line) deconvolved and filtered signal at station 6.

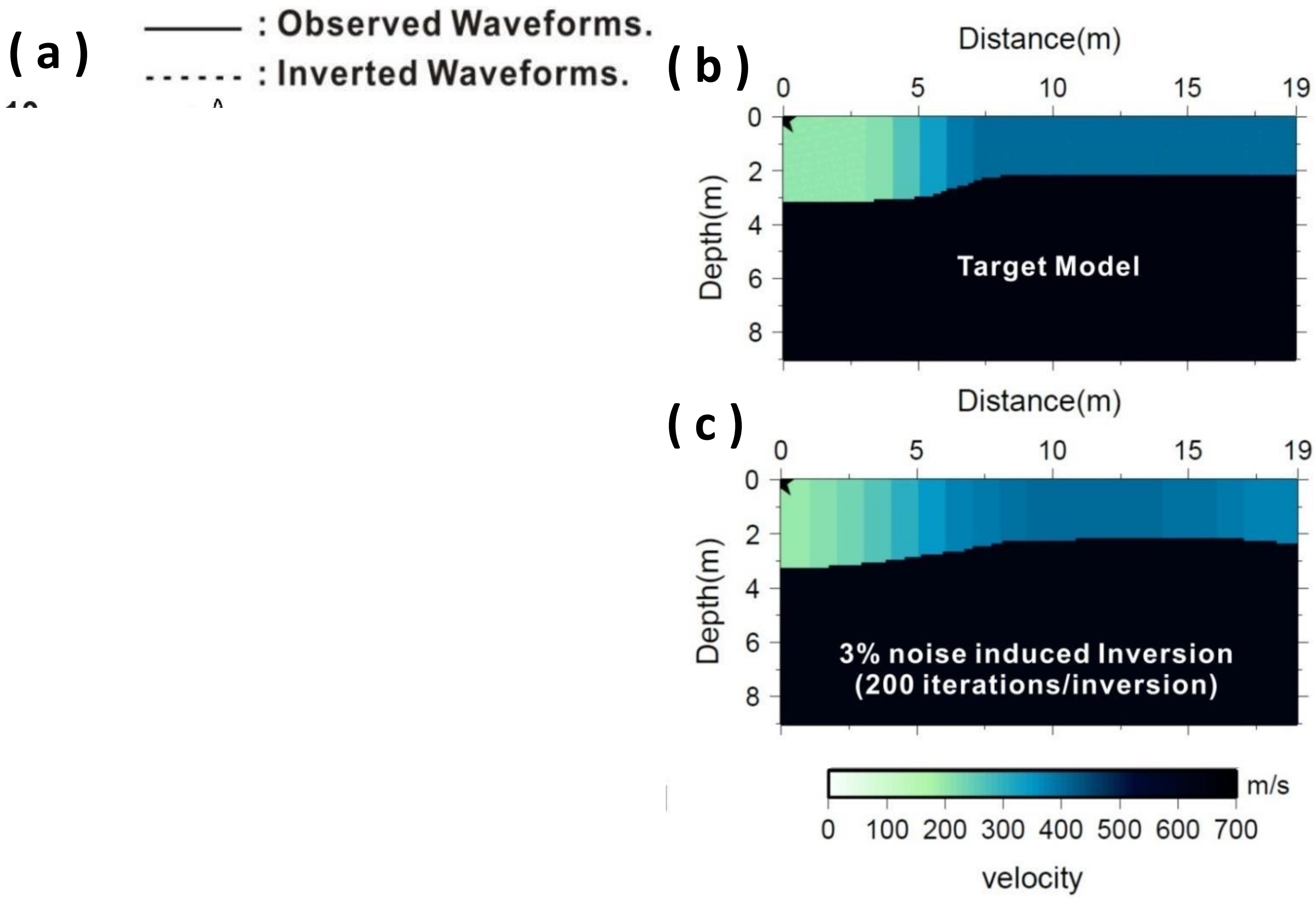

Figure 3.13: Inversion results of the soil with lateral velocity in noisy environment. (a): Comparison of the observed and inverted waveforms of the lateral velocity model. (b): Target soil model. (c): Averaged soil model from 10 inversions from the noisy data.

3.5 Inversion of the blind layer model:

In conventional travel time analysis of seismic refraction methods, it is explicitly assumed that the velocity of each layer is smaller than the layer immediately below it. When this assumption is no longer valid, results from conventional seismic refraction exploration can be misleading. The velocity reversal problem can arise whenever a geological layer has a lower velocity than that of the overlaying layer. Existence of blind layers is one of the most common sources of error in conventional refraction interpretation methods (Palmer, 1980).

The blind layer can also be challenging to be retrieved using modal inversion of surface waves because it requires the incorporation of higher modes during the inversion (O’Neil et al, 2005). We will try to overcome this problem using the waveform inversion. The model C consists of a three-layer soil with a velocity reversal in the second layer. The shallowest layer, referred to as the ‘surface layer’, has a shear wave velocity of 350m/s. The second ‘blind layer’ has a velocity of 200m/s lying over a basement with a velocity of 500m/s, as shown in Figure 3.14b. Detailed model proprieties are listed in Table 3.3.

Table 3.3. Physical proprieties and inversion settings of the blind layer model.

Layer	**True values of the model**			**Inversion Search Limits**		**Inversion parameters**
	Vp(m/s)	*Vs(m/s)*	*ρ(kg/m^3)*	*Vs (m/s)*	*Depth parameter (m) 'Pk'*	Generation = 100 Population= 20 Mutation Rate= 0.01
1	595	350	1700	150-400	1.0-3.0	Crossover rate= 0.7
2	320	200	1800	150-400	3.5-6.0	Initial temperature= 100
3	1000	500	2100	500 (fixed)	-	

Unlike the previous models, we do not discuss lateral irregularities of the layer interfaces, so we just consider flat interfaces between the layers at 2m and 4m depths, respectively, and divide each layer to 10 blocks. The inversion parameters are similar to the previous experiment, using 200 generations and a population of 20 models for each single inversion. Ten inversions were considered for both noise-free and 3% noise corrupted waveforms.

The inversion results for Model C are shown in Figure 3.14. A good fit between the noisy waveforms (black solid line) and the inverted ones (dashed lines) in Figure 3.14a shows that the inversion succeeded in reproducing the observed features in the signal despite the noise corruption. The average model from 10 inversions of the noisy data in Figure 3.14d was able to reconstruct the interfaces of the blind layer at depths of 2m and 4m, with average block velocities of 212m/s.

However, the surface layer velocity was slightly underestimated; the average inverted velocity between the blocks of the final averaged model was 315m/s, while the target model had a velocity of 350m/s. This mis-approximation may be explained by the contamination of the signal by small noise ripples that can corrupt the information included in the signal. In fact, the noise free inverted model in Figure 3.14c is more accurate, with velocity values closer to the target model.

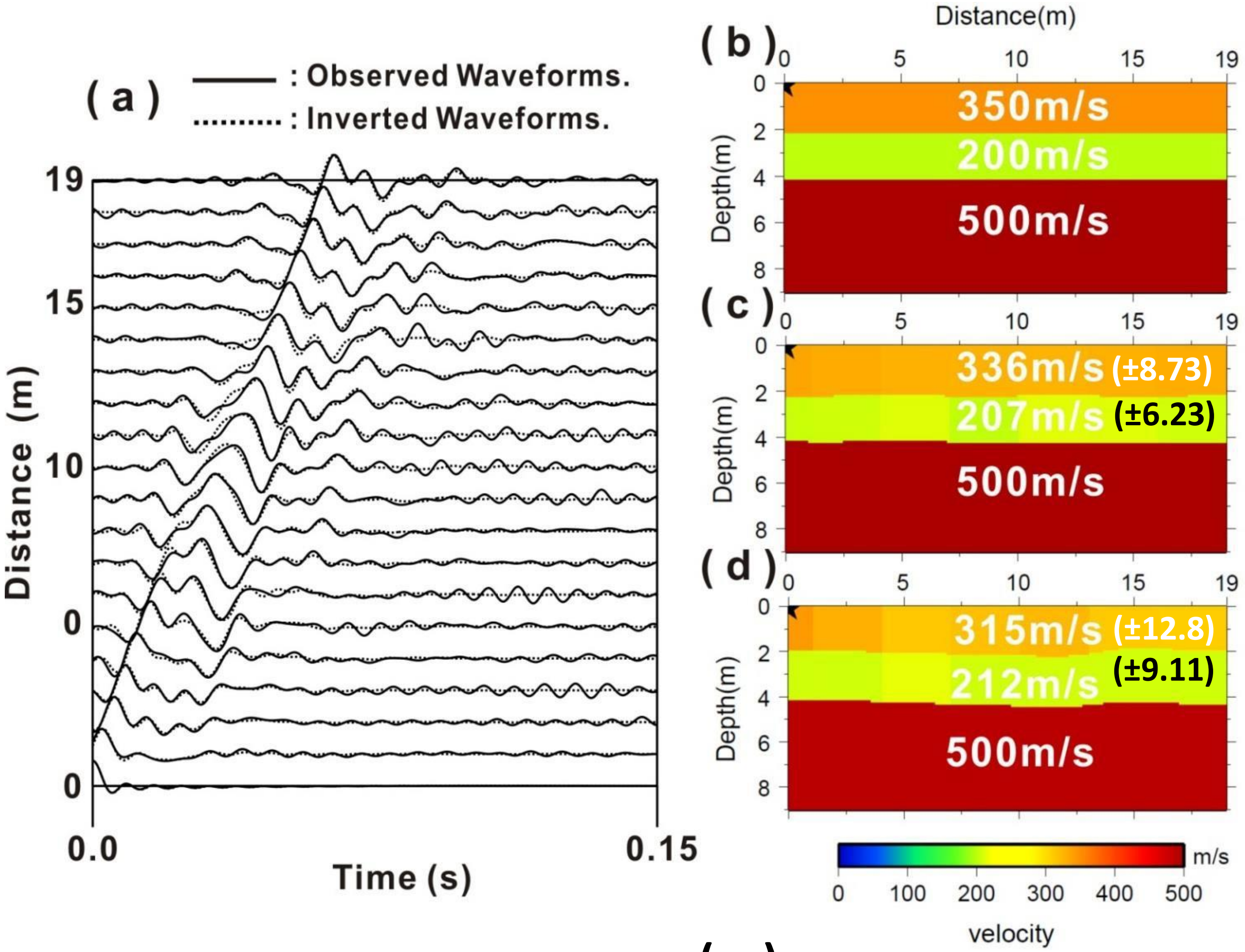

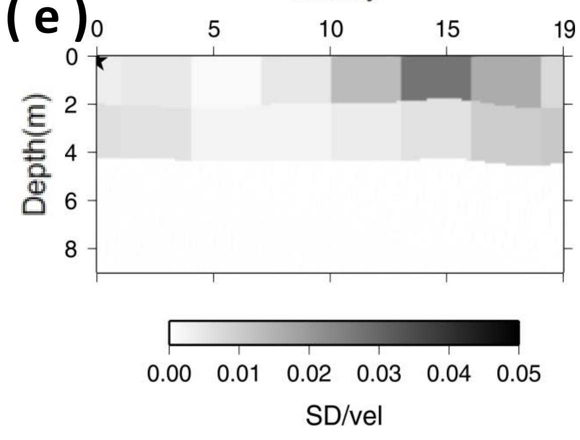

Figure 3.14: Inversion results of the soil with a blind layer.
(a): Comparison of the observed noisy waveforms (black solid line), and the inverted waveforms (dashed line).
(b): Target soil model.
(c): Averaged soil model from 10 inversions of the noise-free data.
(d): Averaged soil model from 10 inversions of the noisy data.
(e): BSD from 10 inversions of the noisy data.

3.6 Computation time:

One of the most common restrictions in FWI is its computational time and the need of a high performance CPU to succeed inversion in a reasonable time. Since it is based on the full wave field modeling, the inversion might be time consuming depending on the model size and the performance of the computer utilized. In fact, in our method, each generation of the inversion requires the modeling of several soil models and this process can be quite time consuming using a single CPU.

In our experiments we parallelized 4 CPU's Intel® Xeon® of 3.33 Ghz, and used a total random memory of 16Gb. The forward modeling of the numerical models discussed in this chapter (300 x 90 grids) requires an average calculation time of 3 seconds to be solved for a single source shot. A single inversion considering a population of 20 individuals for 100 generations, takes approximately 88 minutes regardless of the soil structure or the number of layers, and 10 inversions can easily be done in a couple of work days, which is quite affordable time.

The FD formulation is the part of the algorithm that requires most of the computation time. The computation speed is dependent on the size of the formulated soil and its repetition through the number of models and generations for each inversion. While other operations such as deconvolution or temperature decrease function are very straight forward and can be achieved very quickly.

Another parameter that can influence the computation speed is the number of simultaneous shots for each inversion. To encode multiple sources inversion, each source needs to be modeled independently and the FD formulation of each source increase the computation significantly.

3.7 Comparison with other near surface exploration method:

In order to compare our method with regard to another near surface exploration method, we tried to retrieve the 2D soil structure of the numerical Model A, using the conventional seismic refraction method.

For our analysis we used the seismic refraction method proposed by Hagiwara and Omote (1939). This method is based on the calculation of time depth and velocity function values from forward and reverse times of arrival at different geophones separations along the seismic line. The time section produced by plotting of the time depths provides the basic data or depth determinations and forms a convenient separation point between the data processing and interpretation stages.

First, the layer velocities are estimated from the Hagitori time points beneath each station 'R' from both sides hodochrones, using the following equations:

$$T'_{AR} = T_{AR} - \frac{T_{AR}+T_{BR}-T_{AB}}{2} \qquad (13)$$

$$T'_{BR} = T_{BR} - \frac{T_{AR}+T_{BR}-T_{AB}}{2} \qquad (14)$$

T'_{AR} and T'_{BR}: Hagritori points for 'R' station.
T_{AR} and T_{BR} : Time traveled in the apparent velocity for 'R' station.
T_{AB} : Total time traveled time along the seismic line.

The layer interface is then estimated by calculating the depth beneath each station using the following equation:

$$Z_R = \frac{V_0(T_{AR}-T'_{AR})}{cos\theta} \qquad (15)$$

$$\theta = \sin^{-1}\frac{V_0}{V_1} \qquad (16)$$

Z_R : Depth of the layer interface at 'R' station.
V_0 : Velocity of the first layer.
V_1 : Velocity of the second layer.

We calculated the seismographs from two sources located at the ends of the survey line for the numerical models previously discussed. The first challenge we encountered was the difficulty to pick-up the first arrivals from the seismographs. Despite the use of numerical data, the manual pick up of the initial wave motion at each station was quite challenging and easily misleading, so we decided to consider both upward and downward shot polarities for each source. Combining both polarities on the same trace make the pick of the initial motions more affordable.

3.7.1 Model A:

The waveforms at each source are illustrated in Figure 3.15b, the first motions pick are highlighted by solid circles at each station.

The Figure 3.15c show the travel time hodochrones plotted from the first arrivals. The time-distance curves bends at a distance of 3m from both sides of the seismic line, where the refracted waves arrives at 0.0128s, the first layer velocity is approximated by direct wave arrivals to 234m/s.

Velocity of the second layer was then calculated by averaging the velocities calculated from the Hagitori lines illustrated in Figure 3.15c. The second layer velocity was averaged to 710m/s.

The obtained 2D soil structure is illustrated in Figure 3.15d. This model show a clear irregular layer interface in triangular shape, this model is not very different from the target model in figure 3.15a, with some inaccuracies on depth interface as well as the basement velocity which was exaggerated to 710m/s.

These inaccuracies are probably due to the manual interpretation nature of the method, where the user pick-up the first arrivals and measure their time arrival manually, any small inaccuracies on reading appropriate arrival time can cause significant alterations on model reconstruction, since the model is calculated based on these values.

While the conventional seismic refraction method needed multiple-shots, and suffered from some inaccuracies related to the reading of the first arrivals, the wave form inversion method we are proposing required only a single shot and provide more accurate result than the conventional seismic refraction method.

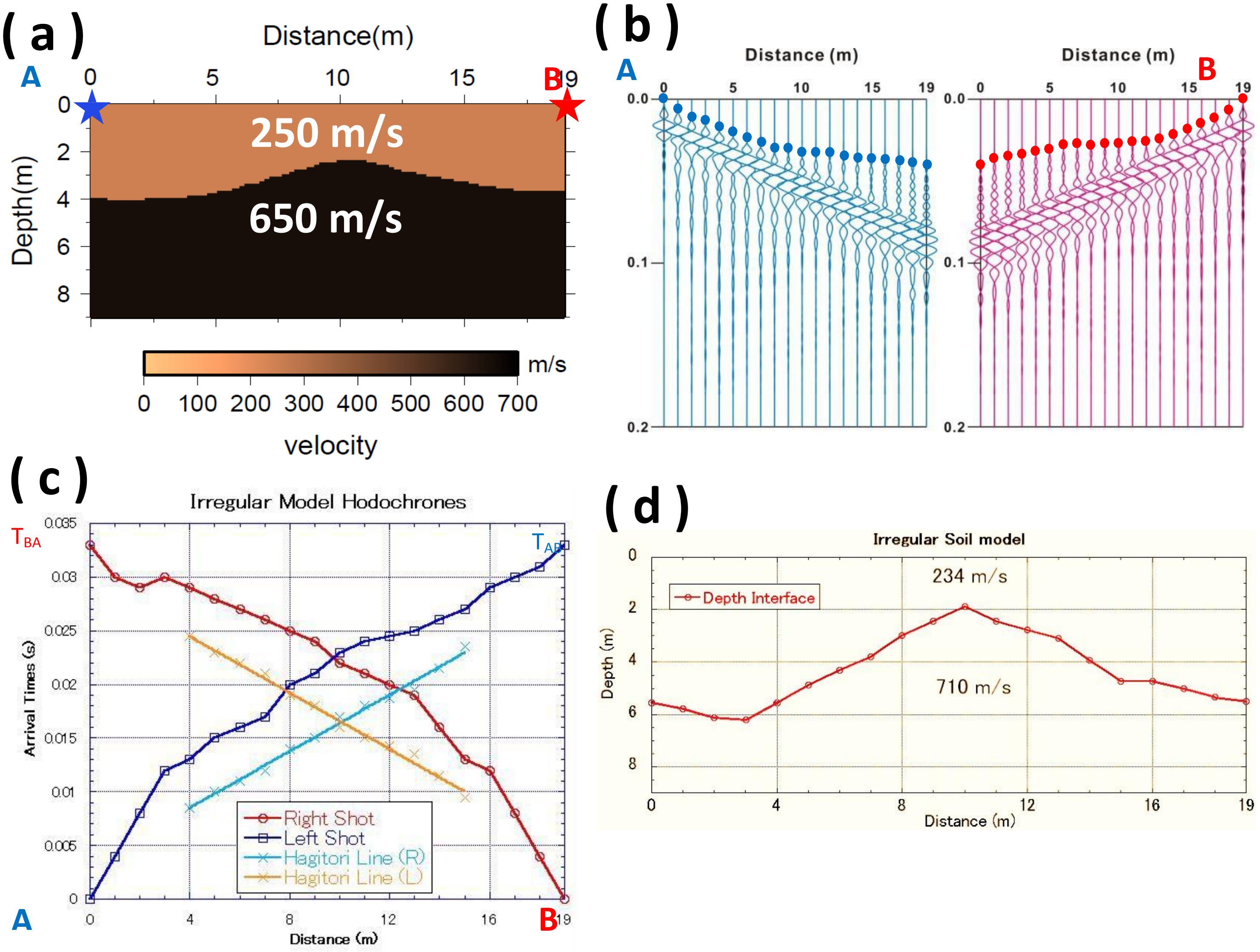

Figure 3.15: Model estimation using the conventional seismic refraction method. (a) Target Model. (b) Recorded waveforms from the two sources. (c) Travel time hodochrones. (d) Estimated soil structure.

3.7.2 Model B:

The waveforms of the model with the lateral velocity variation in Figure 3.16b shows irregular arrival times. The travel time hodochrones in Figure 3.16c. Gives difference velocities of the direct wave arrivals between the left and right sides of the profile. The left shot hodochrone have a velocity of 215m/s, while the right shot shows a velocity of 422m/s. Since this method requires a constant velocity for each layer, we averaged both velocities to obtain the first layer velocity to 318.5m/s, and the basement layer velocity estimated to 900m/s.

The soil model was reconstructed as in Figure 3.16d. The layer interface show a slope at distance of interface model show a clear slop at 6m distance.

Since this method requires homogeneous layer velocity, we had to average the different velocities obtained for the first layer. By doing so, we will lose the velocity difference in the profile, and cannot reconstruct the lateral velocity difference at the same layer, while using our inversion method we successfully determined the different velocities as well as the transition between the low velocity and high velocity within the same layer.

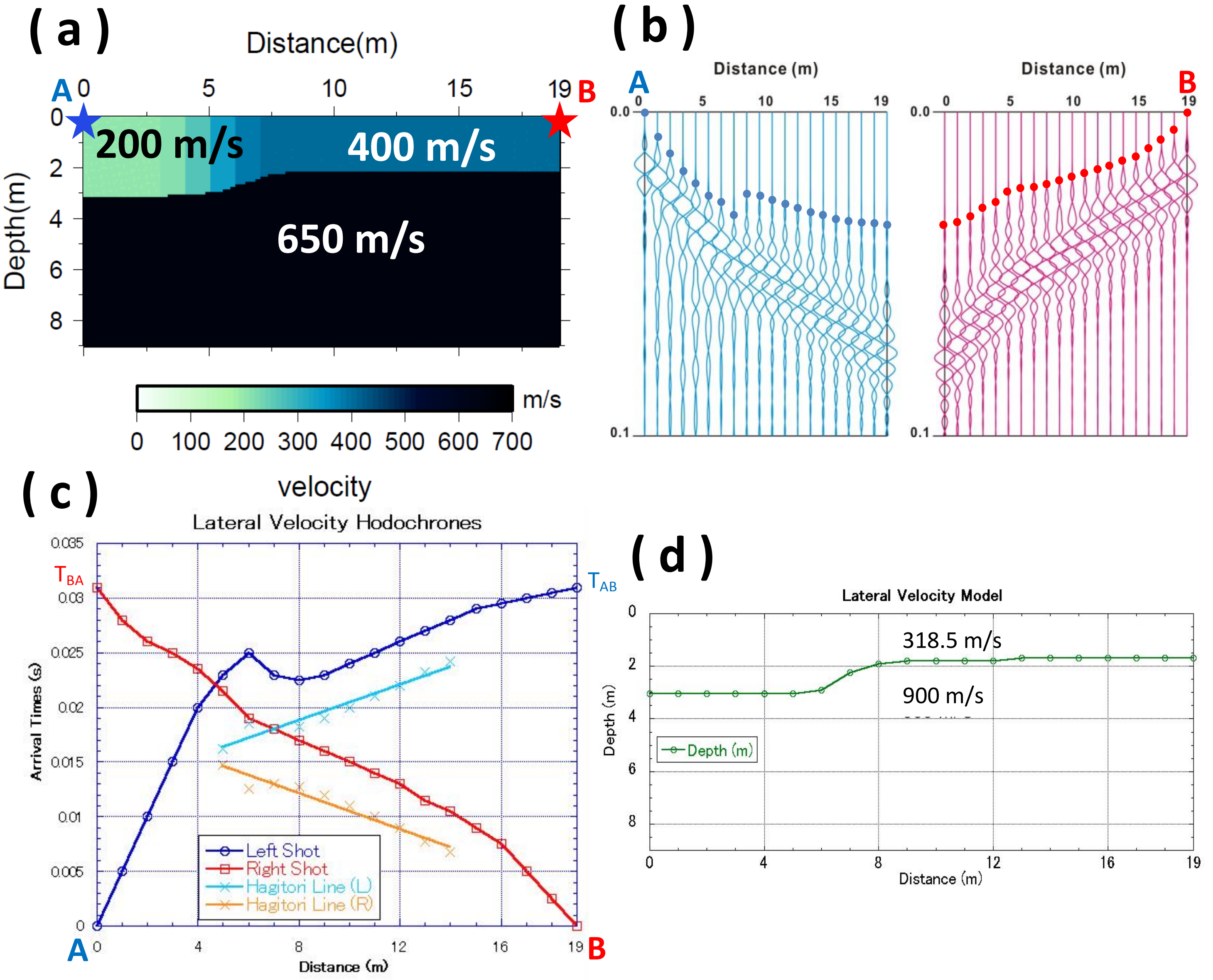

Figure 3.16: Model estimation using the conventional seismic refraction method.

(b) Target Model. (b) Recorded waveforms from the two sources.

(c) Travel time hodochrones. (d) Estimated soil structure.

3.7.3 Model C:

As discussed previously, the blind layer model is one of the restricted models using the conventional seismic refraction method. To underline the limits of this method we will try to retrieve the model c using the Hagiwara and Omote method (1939).

The time travel hodochrones in Figure 3.17c. Shows the direct wave arrivals up to 3m distance from both shots with a velocity of 333m/s of the surface layer. Beyond the direct wave arrival, a faster arrival is recorded from the bottom basement with a velocity of 440m/s. The Hagitori lines calculated with these conditions intersects with the travel time hodochrones making the method impossible to apply as it gives negative values for depth.

For this reason we just considered the direct wave arrivals and the basement velocity to estimate a simple layer depth as illustrate in Figure 3.17d. The obtained model is very different from the target model as the blind layer couldn’t be seen from the conventional refraction method. Using the waveform inversion we succeeded to overcome the blind layer problem, and successfully reconstructed the soil layer.

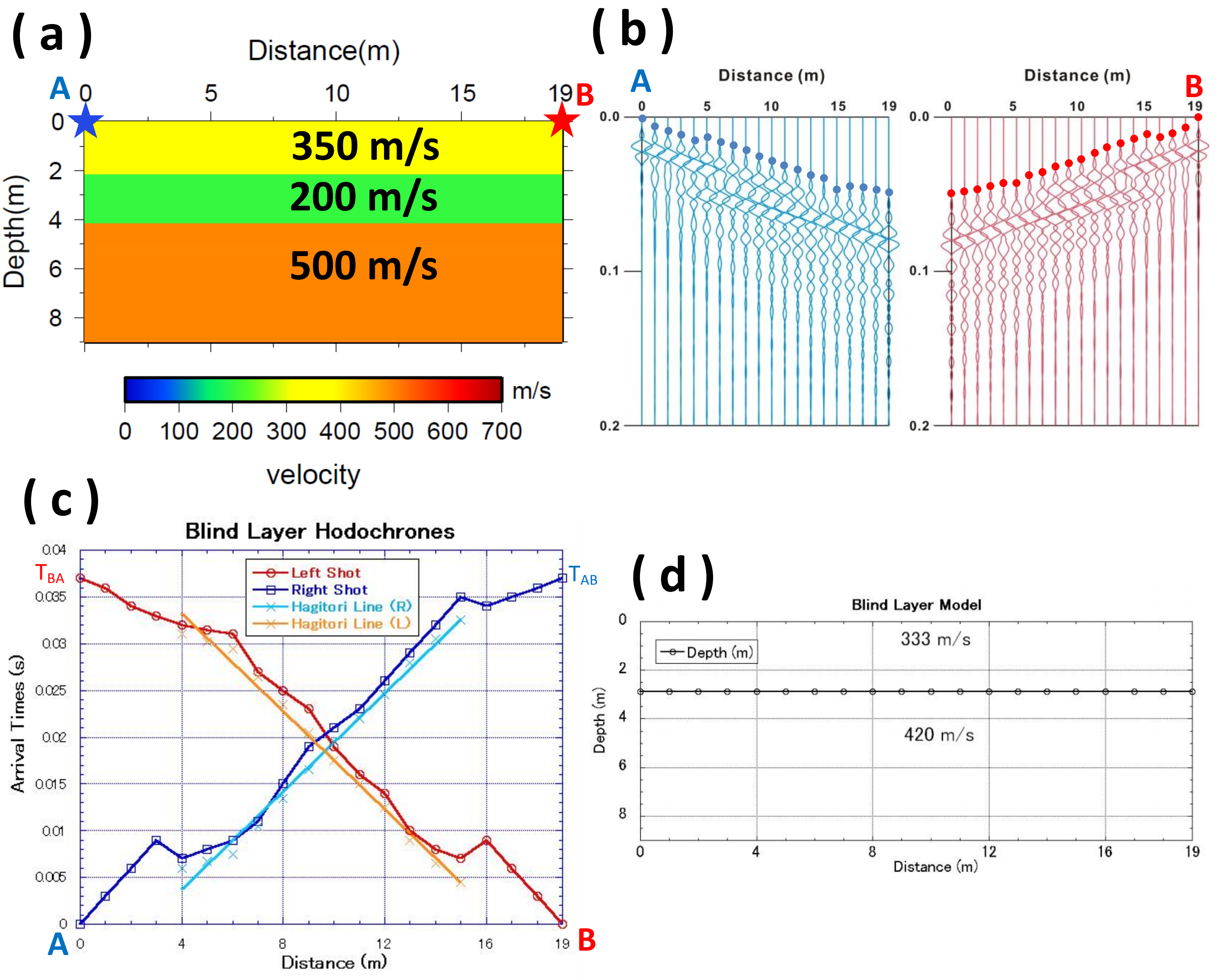

Figure 3.17: Model estimation using the conventional seismic refraction method.
(c) Target Model. (b) Recorded waveforms from the two sources.
(c) Travel time hodochrones. (d) Estimated soil structure.

Chapter 4

APPLICABILITY OF THE METHOD FOR FIELD DATA INVERSION

4.1 Site location:

In the previous chapter we have proven the efficiency of our method using numerical experiments of different soil models. In the current chapter, we will try to prove the applicability of our method to real data acquired on field, and retrieve a 2D soil profile from seismic data.

For this purpose we conducted a field survey at Suzukakedai campus, Tokyo Institute of Technology in Kanagawa prefecture - Japan, located in Figure 4.1a. We selected a newly constructed parking lot as the investigation area (Figure 4.1b) because of the availability of borehole data including S-wave velocity logging carried out previously. The availability of the borehole data allowed correlation of our 2D inverted soil model with the existing one-dimensional S-wave velocity profile.

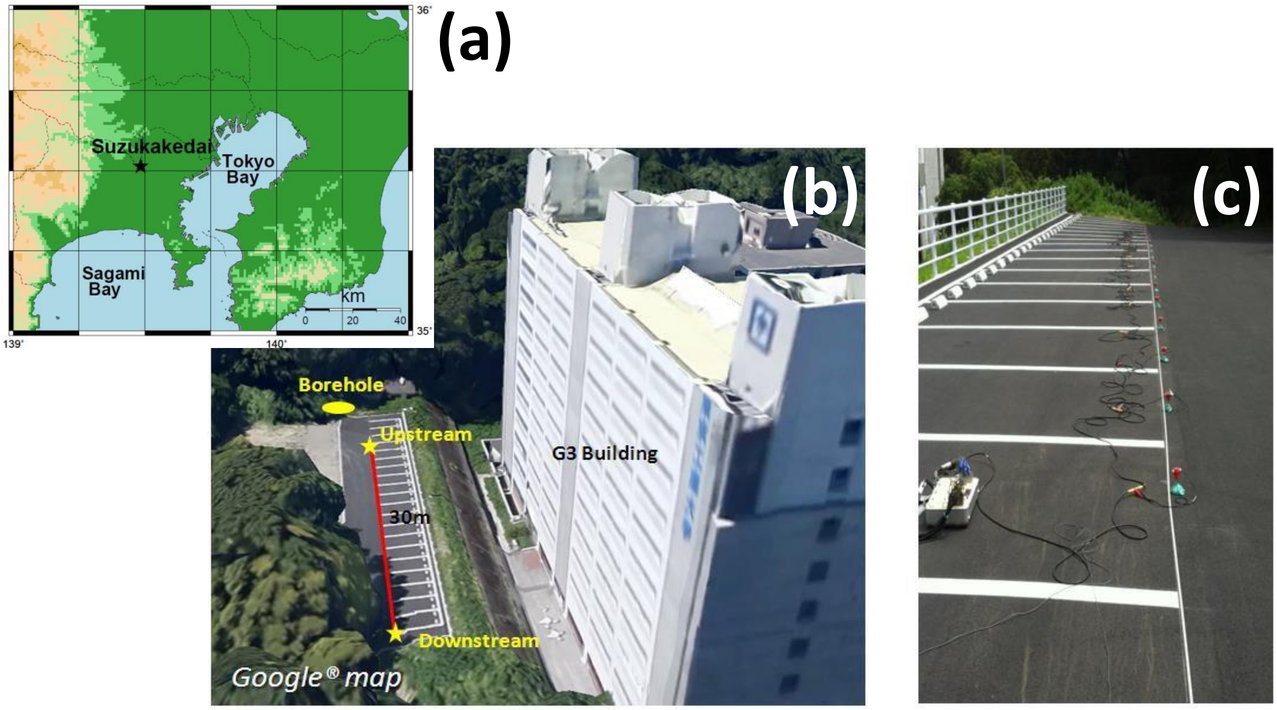

Figure 4.1: Location of the field data acquisition.

(a) Location of investigated site.

(b) Areal view of the investigated area after parking constructions.

(c) Picture taken at the upstream side of seismic line.

Conventional seismic refraction survey was used to acquire the P-SV waves generated by sledge hammering on the surface. Since the position of the borehole was covered by heavy bushes, the survey was almost impossible to perform across the borehole. The survey line was spread along the pavement as shown in Figure 4.1c. For polarity distinction, we will use the term ‘upstream’ for the offset near the borehole side, and ‘downstream’ for the opposite side of the survey line.

It should be noted that the investigation area was modified after drilling the borehole. The left satellite image in Figure 4.2a shows the state of the area before the construction of the parking lot, while the right image in Figure 4.2b shows the same location during the seismic survey. The shallowest layer was improved and a pavement was constructed on the surface.

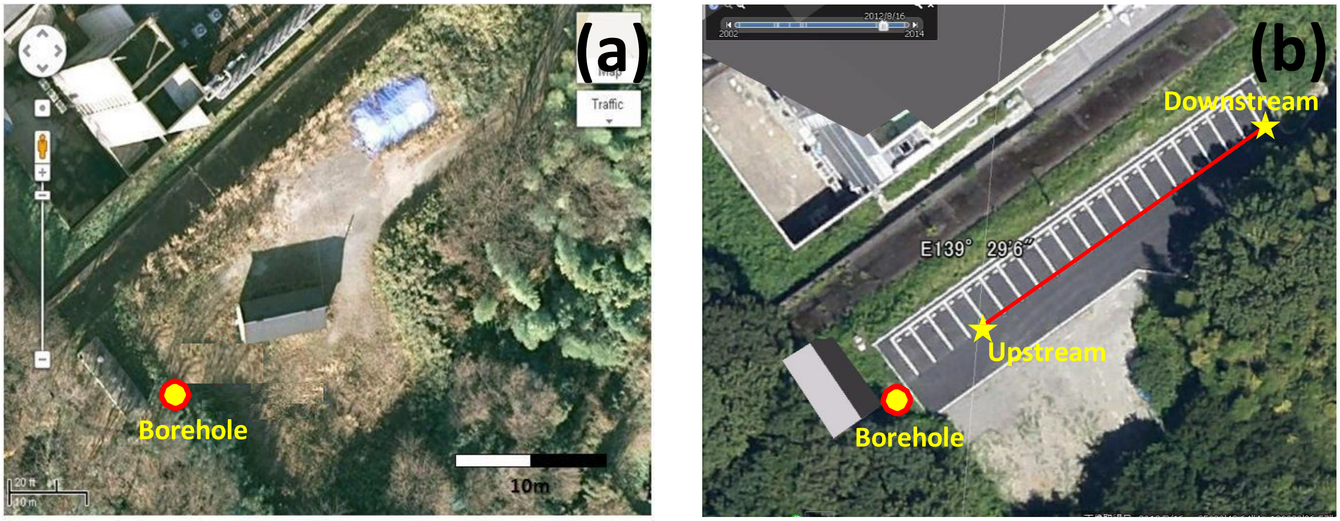

Google® map Google® map

Figure 4.2: Satellite images of the investigated area.
(a) Area before the construction of the parking lot (2010).
(b) Area after the construction of the parking lot (2013).

4.2 Data acquisition:

A line of 16 receivers recorded the vertical component of the ground motion. The recording of the P-SV wave field was carried out using 4.5Hz vertical geophones with a spacing of 2m covering the surveying line within 30m of the investigation area. Since we performed the survey over a pavement, the geophones were fixed to the ground using artificial clay to ensure a correct transmission of energy and to reduce the coupling effect between geophones and ground. Two vertical shots using a 5kg hammering excited the surface at both ends of the survey line. A wooden plate doubled with a sponge cushion was used to generate impacts without damaging the newly constructed pavement. An auto-triggering system allowed acquisition after the detection of the first motion at the nearest station from the impact, this station was considered as the trigger station and was not included in the inversion.

Geophones were connected to an amplificator illustrated in Figure 4.3a, allowing us to tune the appropriate amplifications of the analog records. The acquisition was performed using a 16 channels data logger KEYENCE® Data mark NR-2000 illustrated in Figure 4.3b, with a sampling rate of 20KHz for an acquisition window of 0.2s.

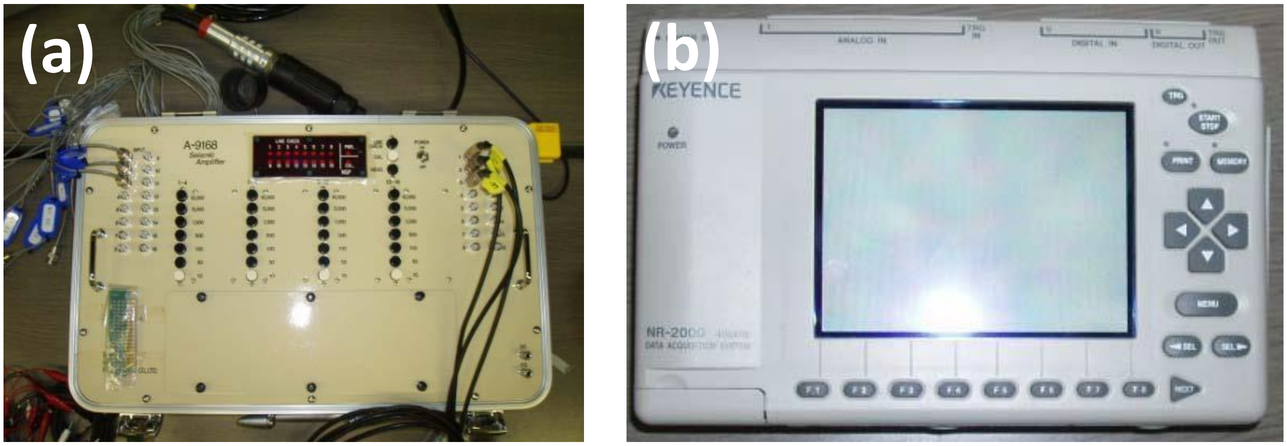

Figure 4.3: Instruments used for acquisition.
(a) Amplificator. (b) Data Logger KEYENCE®.

4.3 Data processing and inversion:

We inverted the data from the two shots at the upstream and downstream ends of the survey line simultaneously by summing the individual misfits from the two shots. Figures 4.4a and 4.4b show the raw signals obtained from the upstream and the downstream shots. We divided the raw signal by the closest station to the source for each trace in order to obtain the source-free deconvolved waveforms. The spectral ratios of records at some stations to the reference one are displayed in Figure 4.4e for the upstream shot, and Figure 4.4f for the downstream shot. The frequency range utilized in the inversion for both shots is 20Hz to 70Hz. The final deconvolved and filtered waveforms that will be used in the inversion are plotted in Figures 4.4c and 4.4d. A finite difference mesh of 400 by 200 grid points in the x and y directions, respectively, with a 0.1m grid spacing was constructed to invert the two-dimensional soil, each layer was divided into 20 blocks.

For real data inversion, it is very important to refer to existing 1D soil profiles of the area of interest, which allow fixing the number of layers to be inverted, as well as their depth and velocities search limits. In our case we use the borehole data available in the area to tune our inversion with the appropriate number of layers and search limits. According to the borehole profile, a three-layer model was assumed in the inversion with the search limits for our inversion as in Table 4.1. P wave velocities also obtained from the borehole PS logging were used in the inversion because our interest was the S-wave velocities. The P wave velocities, densities as well as search limits were defined from the borehole PS logging as in Table 4.1.

Table 4.1. inversion parameters (search limits) of the real data.

	P-wave velocity *(m/s)*	**S-wave velocity search limits *(m/s)***	**Depth parameter *(m)* 'Pk'**	**Density *(kg/m³)***
Layer 01	480	100 - 450	0.2 - 4.0	1600
Layer 02	725	100 - 450	4.5 - 7.0	1700
Layer 03	1100	Fixed (500)	-	1900

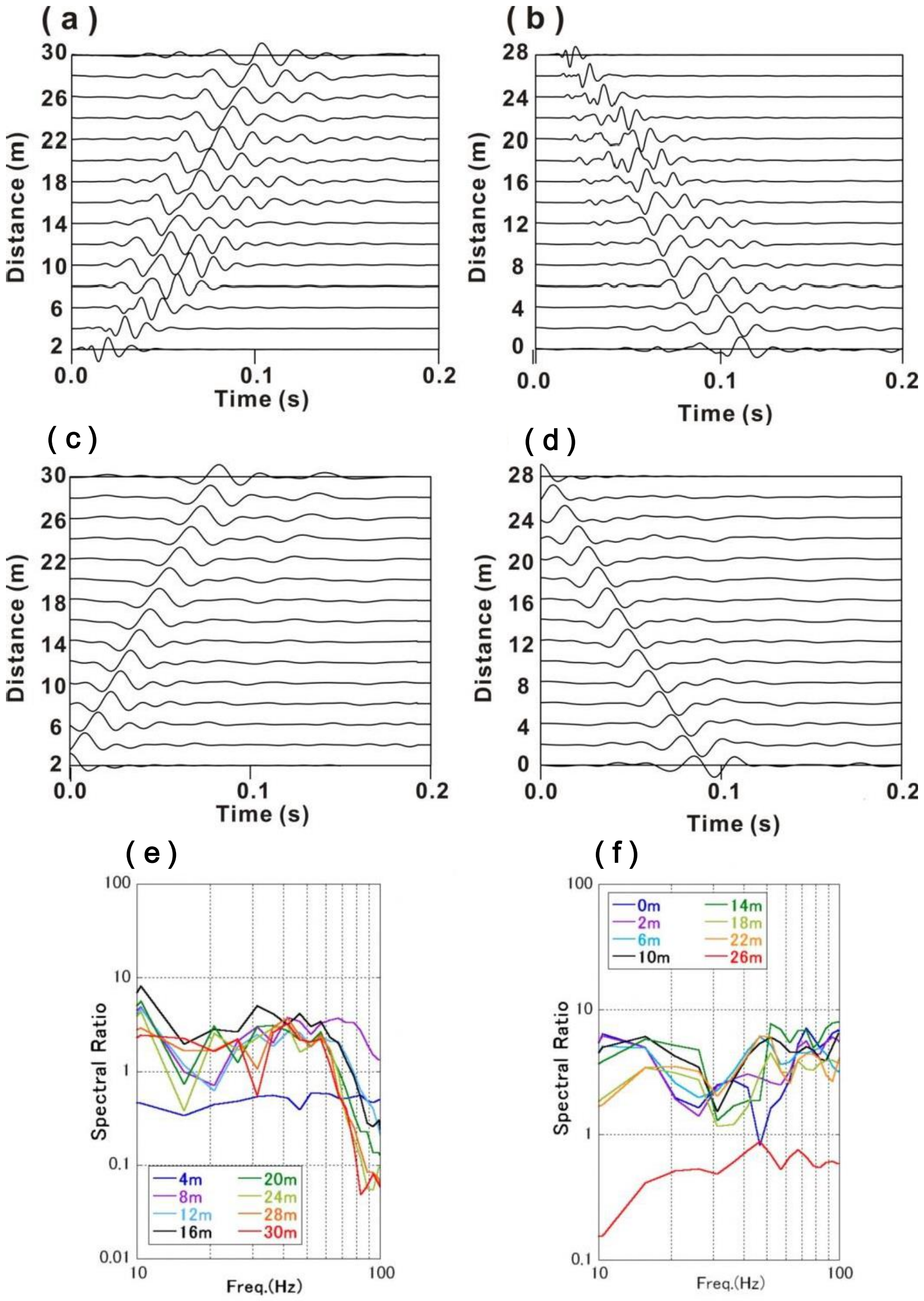

Figure 4.4: Raw data and results of deconvolution.

(a): Raw acquired ground velocities at the upstream shot.
(b): Raw acquired ground velocities at the downstream shot.
(c): Deconvolved and filtered waveforms of the upstream shot.
(d): Deconvolved and filtered waveforms of the downstream shot.
(e): Spectral ratio with respect to reference station of some stations from the upstream shot.
(f): Spectral ratio with respect to reference station of some stations from the downstream shot.

Ten inversions were carried out using the records from both upstream and downstream simultaneously, and similar inversion parameters to the numerical experiments were used for the real data.

The results of the inversion are summarized in Figure 4.5. The inverted waveforms for both upstream and downstream shots in Figures 4.5a and 4.5b show acceptable fitting with the observed waveforms. The main phase arrivals at each station were well reproduced. The two-dimensional averaged model of 10 inversions for the simultaneous upstream and downstream shots is displayed in Figure 4.5c, where the shot locations were indicated with black stars at 0m and 30m. The final inverted soil model have a top layer velocity of 284m/s with a velocity standard deviation between blocks of the final averaged model of ±14.9m/s, while it has an approximate thickness of 1m,

The second layer lays over the basement at 6m depth. This layer underlines a notable velocity variation from 258m/s at 4m distance, to 345m/s at 15m distance, with a large velocity standard deviation between the blocks of the final inverted model of ±21.5m/s, underlying a clear variation of the velocity within the same layer, as illustrated in Figure 4.5c.

The standard deviation for each block velocity from ten inversions (BSD) is illustrated in Figure 4.6. The velocities standard deviation shows values not higher than 0.05 along the 2D profile, indicating the likelihood of the blocks between the independently inverted models.

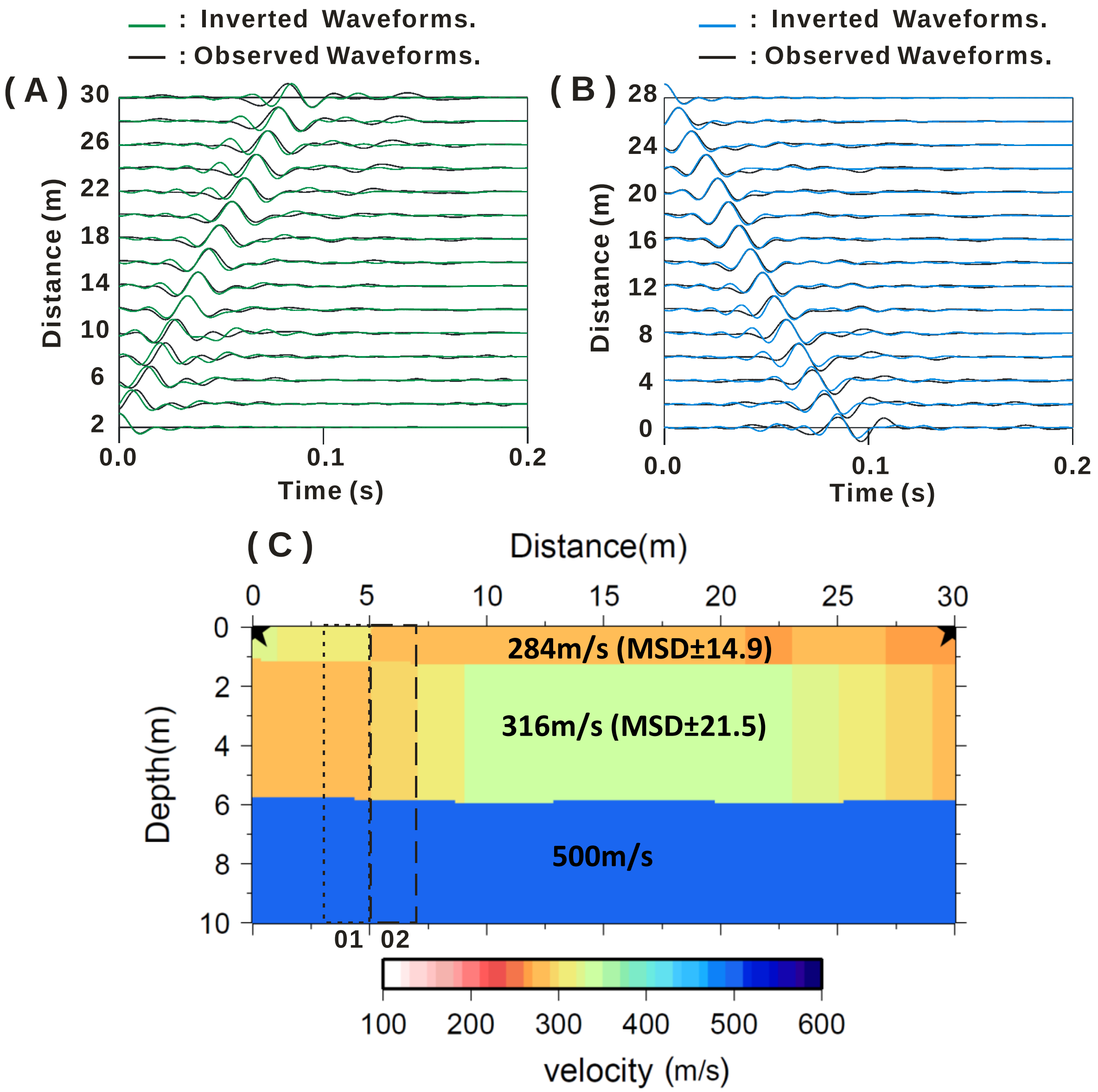

Figure 4.5: Inversion results of the real data.
(a): comparison of the observed and final inverted waveforms of the upstream shot.
(b): comparison of the observed and final inverted waveforms of the downstream shot.
(c): Averaged model from 10 inversions using multiple shot inversion materialized by the black star at 0m and 30m.

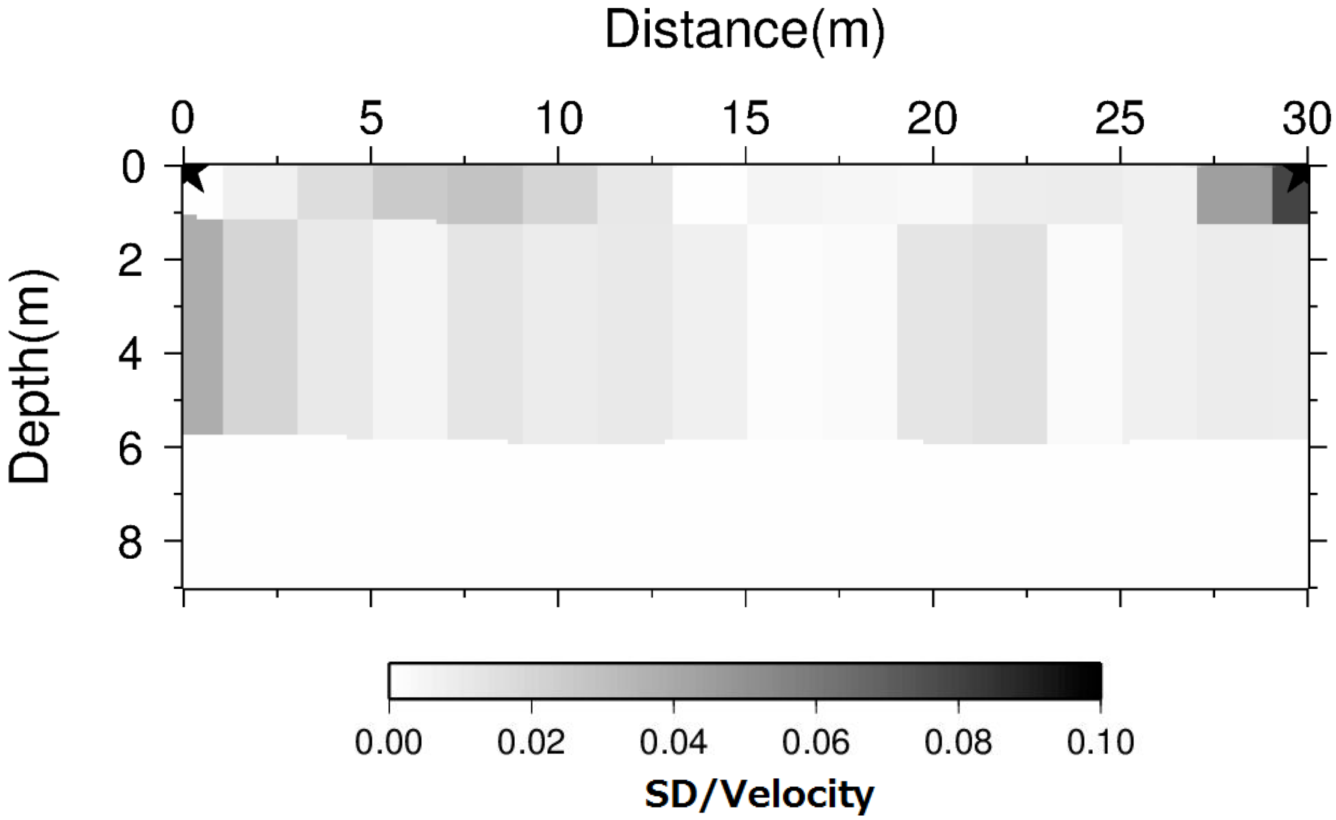

Figure 4.6: Standard deviation for block velocity inversion of real data.

4.4 Comparison to borehole and microtremor results:

In order to correlate the 2D inverted profile with the borehole data, we sampled one-dimensional profiles from the inverted soil model at distances of 3m and 7m. We compared our profiles at this range because it is the closest distance to the borehole in our survey line that contains information about the subsurface in its waveforms. The locations of two sampled 1D profiles (block 01 and block 02) are underlined by black dotted line and black dashed lines in Figure 4.5c. Since our inversion targets are the two first layers of the profile obtained from the borehole logging, layers deeper than 8m are out of discussion.

Figures 4.7a and 4.7b show the lithology and the velocity profiles obtained from borehole data. The comparison between the shear wave velocity approximating 300m/s on the block 01, and 290m/s on block 02, while the borehole gives the surface layer a velocity of 200m/s in the top layer. This over-estimation near the surface can be explained with the improvements of the surface layer carried out during the pavement construction, as shown in the picture taken during the pavement construction, identifying a clear additional layer to the original loam in Figure 4.8.

The thickness of the top layer in the inverted profiles is similar to the borehole profile, around 1m. The second layer velocity was better estimated than the first layer velocity with reference to the velocity and thickness and both profiles give relatively close velocities to the borehole profile around 300m/s.

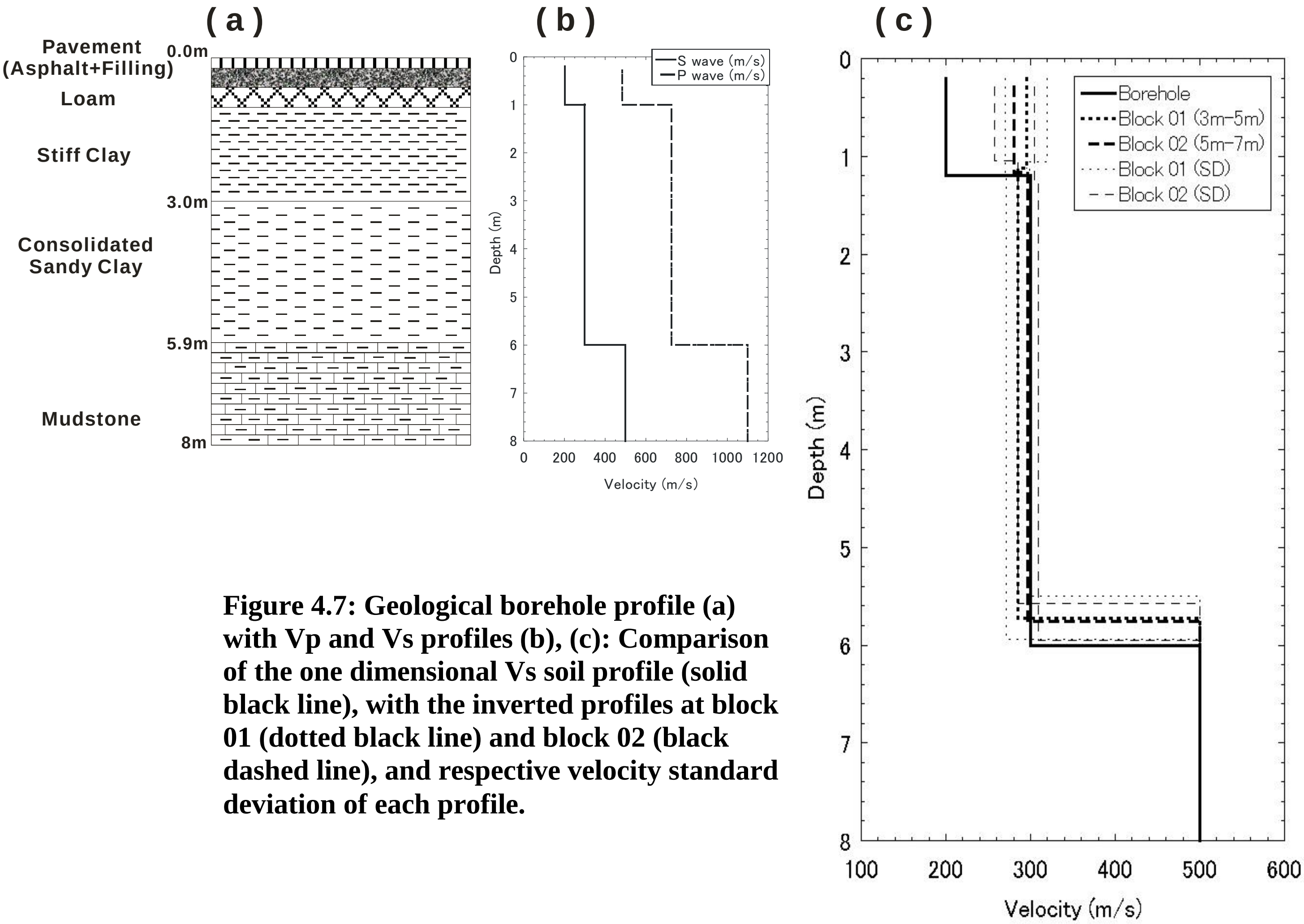

Figure 4.7: Geological borehole profile (a) with Vp and Vs profiles (b), (c): Comparison of the one dimensional Vs soil profile (solid black line), with the inverted profiles at block 01 (dotted black line) and block 02 (black dashed line), and respective velocity standard deviation of each profile.

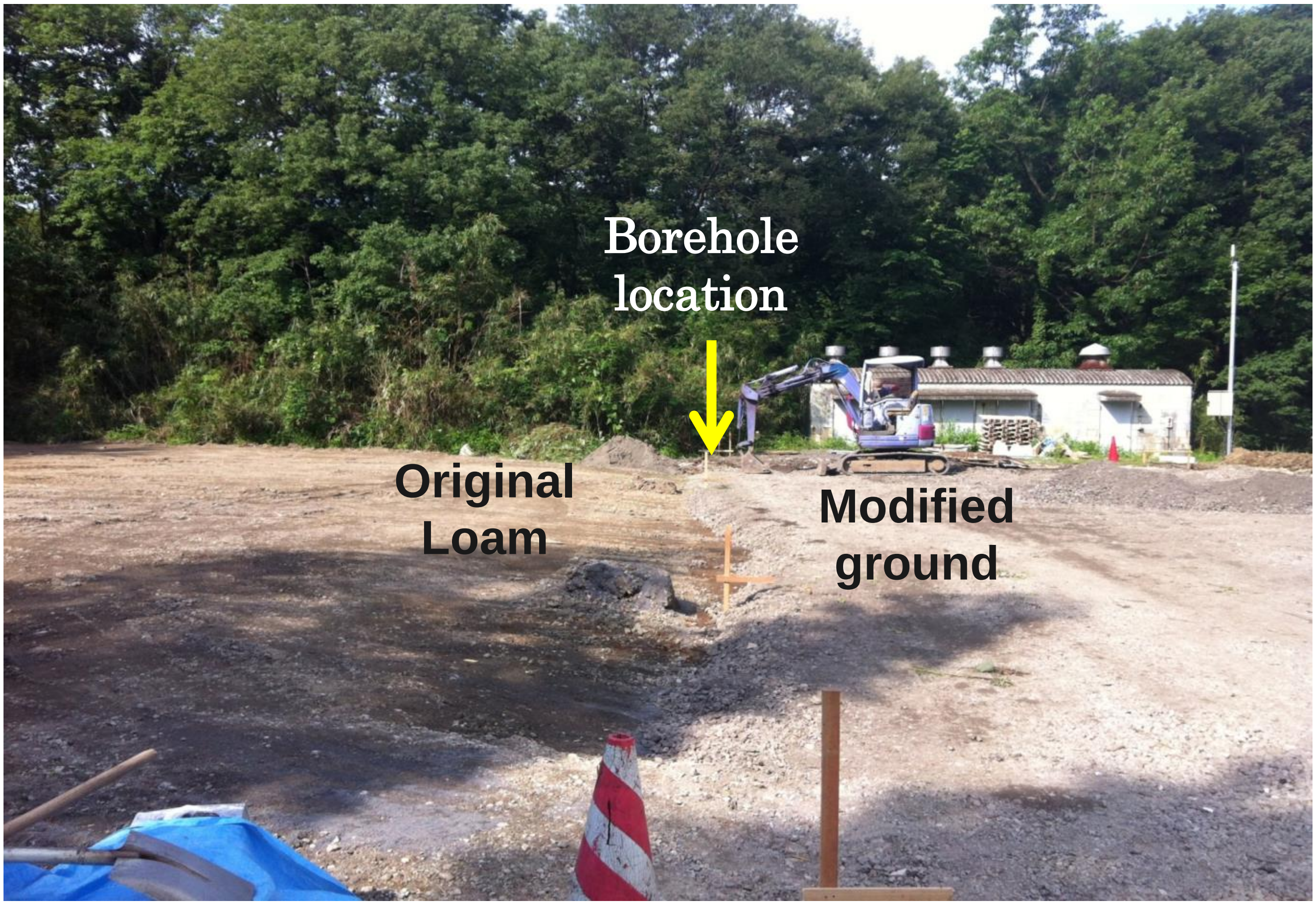

Figure 4.8: Photo taken during the pavement construction in the area of study.

In order to investigate the presence of the lateral velocity variation detected by our 2D inverted model along the second layer of the soil profile, we conducted H/V microtremor measurements along the seismic survey after the pavement construction.

The H/V spectral ratio method is an experimental technique to evaluate some characteristics of soft-sediments deposits. This method consists of dividing the Fourrier spectra of horizontal and vertical components of ambient vibrations (microtremor) to obtain the natural response of the soil, and it is routinely applied in seismic microzonation studies and local site analysis. In earthquake engineering, H/V spectral ratio is influenced by the impedance ratio between layer velocities, and velocity impedance between two different soil configurations could be easily identified by comparing their spectral ratios. We installed four H/V microtremor stations along our survey line at distances of 2m, 5m, 15m and 17m, shown respectively by blue, red, black and green circles in Figure 4.9a. These stations are chosen at locations where our inverted 2D model underlines a velocity difference on the second layer as in Figure 4.9b.

The observed H/V spectral ratio at each station are compared at Figure 4.9c. The four stations shows similar spectral feature up to 10Hz with a common fundamental peak at 6Hz, assuming similar soil structure to a certain depth. However clear difference in the high frequency content between 10Hz and 30Hz can be noticed between the two stations at 2m and 5m distance, and the two other stations located further at 15m and 17m. This sudden variation of the spectral ration at the high frequencies between 5m and 15m, indicates a difference of velocities impedance ratio between layers, generated by possible lateral velocity change along the shallow layer.

The microtremor results can be correlated with our 2D inverted model that underlines a clear velocity change among the second layer, explaining the difference between the H/V spectral ratios from 5m to 17m distances.

This abnormal velocity change within the second layer may be caused by differences in the local soil compaction carried out for construction purposes.

Theoretical Rayleigh wave elipticity calculated from the 1D profiles at 5m and 15m are plotted in dashed lines together with the H/V spectral ratio at Figure 4.9c. The calculated elipticity at 5m in red dashed line have more or less flat spectra, while the elipticity at 15m in black dashed line have different shape with a small peak at around 10Hz and trough at 25Hz. This different of the calculated elipticity can be correlated with the H/V spectral ratio, except for the peak 6Hz that cannot be seen on the calculated elipticities, which can probably due to deeper layers that we did not included in our calculated models.

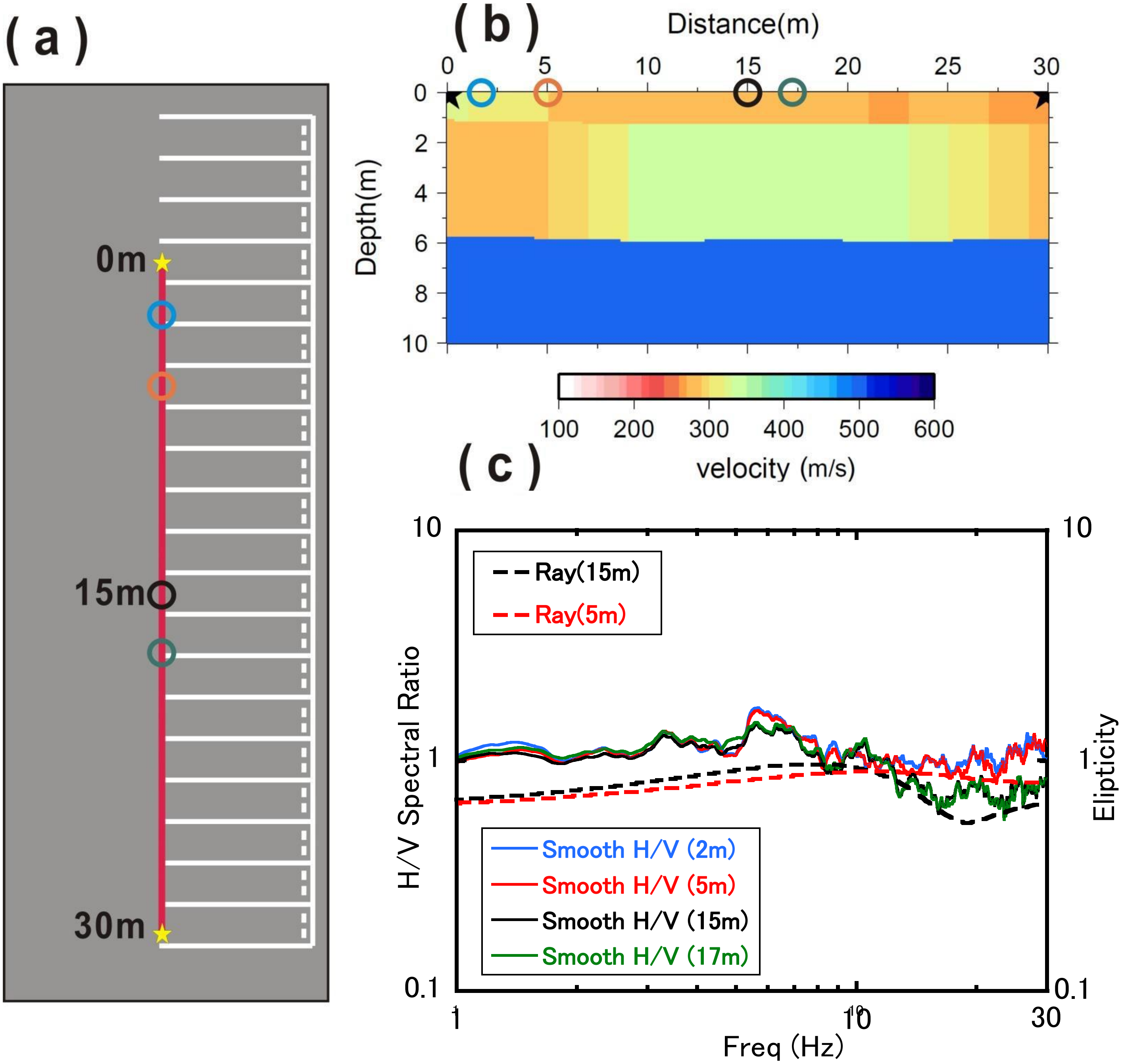

Figure 4.9: Microtremor exploration along the survey line.

(a): Schematic representation of the seismic survey line in red solid line, and the H/V microtremor stations.

(b): Position of the H/V microtremor station along the 2D inverted profile.

(c): H/V's spectral ratio at 2m, 5m, 15m and 17m distance along the survey line, with the calculated Rayleigh wave ellipticity at 5m and 15m distances.

Chapter 5

WAVEFORM INVERSION FOR EARTHQUAKE ENGINEERING PROBLEMS: A CASE STUDY

5.1 Problematic introduction:

On March 11, 2011, the eastern coast of Japan was jolted by a giant Mw9.0 earthquake. The Earthquake off the Pacific Coast of Tohoku was the largest earthquake to strike the Japanese archipelago in history, and it caused a huge tsunami that in turn caused considerable human and infrastructure damage. The seismic intensity at some sites reached the maximum value of 7 on the Japan Meteorological Agency (JMA) intensity scale. Peak values of 2700 cm/s^2 in the NS component and 1880 cm/s^2 in the UD component were observed at the K-NET Tsukidate (MYG004) located in Miyagi Prefecture, Japan, about 50km from the epicentral area, as illustrated in Figure 5.1a.

According to the JMA intensity scale, structures in areas subjected to shaking so strong that it reaches an intensity of 7 are susceptible to very heavy damage. However, it turned out that no major damage to the wooden houses located in the vicinity of the station was reported. Structures remaining undamaged in the wake of very high observed PGA are an enigma that has given rise to much debate in the scientific community. Motosaka (2011) explained the very high PGA by citing a partial uplifting of the base foundation of the strong motion instrument. Irikura and Kurahashi (2011), as well as Sakai et al. (2010) suggested that the very minor damage during this earthquake was due to the predominant period of the ground shaking, shorter than 0.5s, despite the high acceleration of the ground motion. Hayakawa et al. (2011) suggested the effects of deep soils on the high frequency amplification as one of the reasons. Other authors emphasized the role of the non- linear behavior of the shallow soil: Midorikawa et al. (2011) reported the nonlinearity of the soil at the K-NET MYG004 station by showing the response spectra dominant periods shifting to longer periods with the increasing PGA.

The non-linearity of the shallow soils surrounding the K-NET MYG004 station was quantified through microtremor studies presented by Matsushima et al. (2011), Hayakawa et al. (2012), and Nagashima et al. (2012). A series of studies by Yamanaka et al. (2011) and Yamanaka et al. (2012), revealed an amplification abnormality of the shallow soils near the strong motion station. A one-dimensional S-wave velocity profile obtained from microtremor array measurements showed that the near-surface layers were responsible for the local amplification at that site. They also reported the high amplification of the aftershocks recorded in the vicinity of the K-NET MYG004 using temporary accelerometers dispatched just after the earthquake, and the significant amplification at the site of our interest was interpreted as being due to local site effects of the shallow soils. A more recent study by Satoh (2013) reviewed all the previously suggested explanations for the large amplifications at MYG004 and identified their potential frequency occurrences. The uplifting of the strong motion station foundation proposed by Motosaka (2011) would occur at a frequency of 4Hz, and the soil non-linear behavior would be noticed between 4 Hz and 5 Hz, while the cliff sedimentary layer effect proposed by Yamanaka et al. (2012) would occur at 6 Hz or higher.

The objective of our study is to provide a 2D shallow soil structure in the vicinity of the K- NET Tsukidate station MYG004. This 2D profile will complete the one-dimensional studies conducted by Yamanaka et al. (2012) and will provide an understanding of the lateral structures of the shallow soil. We will also reassess the effect of the 2D soil structure on the local site amplification, and attempt to provide some clues that may help in the understanding of the very high PGA during the 2011 Earthquake off the Pacific Coast of Tohoku. To these ends, we conducted a seismic refraction survey near the strong motion station, and we tried to retrieve the two-dimensional shallow soil profiles using the wave-form inversion of the acquired seismic data together with the microtremor array exploration.

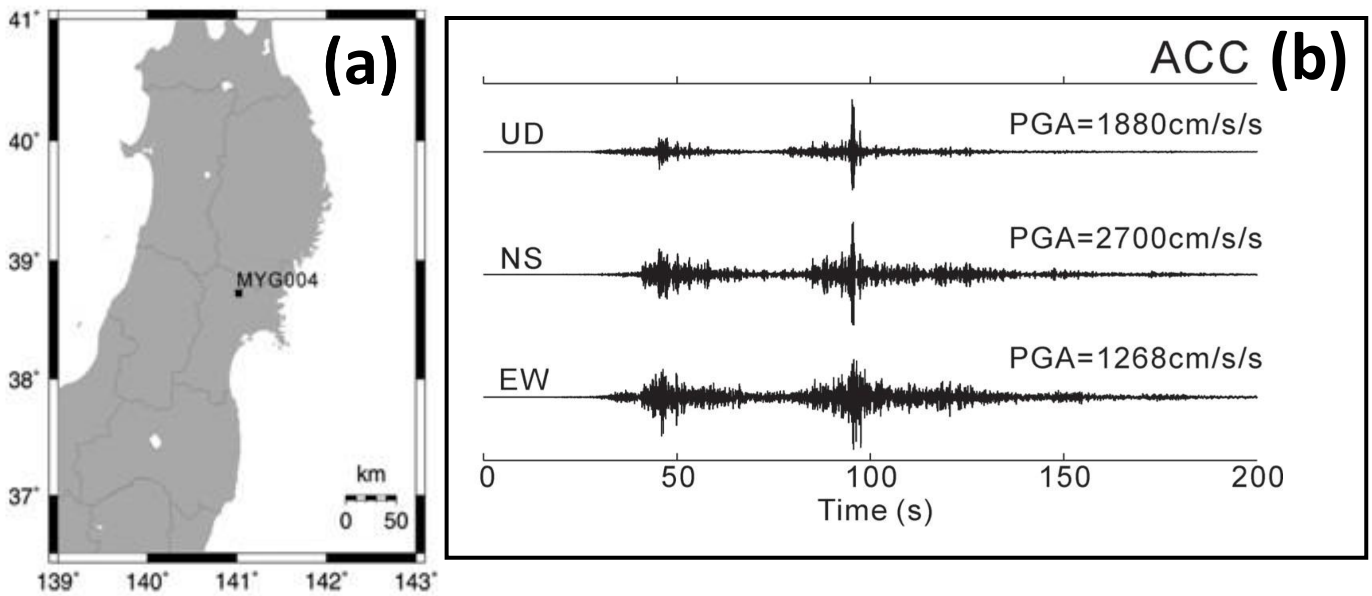

Figure 5.1: Recordings at the strong motion station MYG004.

(a) Location of the K-NET Tsukidate strong motion station (MYG004) in black circle.

(b) Ground accelerations at MYG004 during the main shock of the 2011 off the Pacific Tohoku Earthquake.

5.2 Geophysical studies:

The K-NET Tsukidate station (MYG004) in the northern part of Miyagi Prefecture is located just south of the parking lot of Kurihara Culture Hall, as illustrated in Figure 5.2a. The strong motion station at the top of a 5m-hight cliff became operational in 1996. That area of Tsukidate had garnered particular interest from the earthquake engineering community for the instability of its soils and the numerous landslides triggered after the 2003 Minamisanriku earthquake (Fukumoto et al. 2007), and the earthquake damage that occurred in the 2008 Iwate-Miyagi Nairiku earthquake (Sakai et al. 2010), where the MYG004 station recorded an intensity of 5.7 on the JMA scale. This same area underwent intensive geophysical studies after the 2011 Earthquake off the Pacific Coast of Tohoku by scientists attempting understand the abnormal PGA recorded during that event.

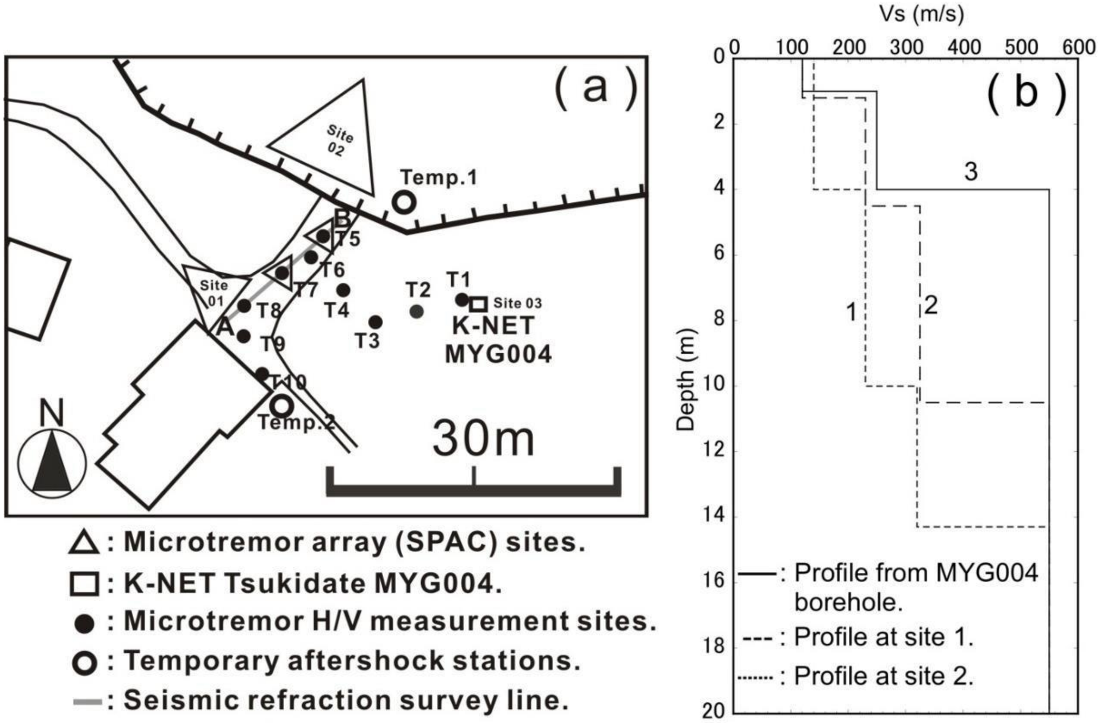

Figure 5.2: (a) Schematic map of the area.

(c) 1D S-wave velocity profiles at each site by Yamanaka et al. (2012).

5.2.1 Ground motion analysis at MYG004:

The accelerations of the ground motion records observed at MYG004 during the main shock are shown in Figure 5.1b. The PGA is significantly high as 2.7G. The response spectra for the ground motions observed at the site during the main shock and some of aftershocks with different magnitudes are shown in Figure 5.3a. The figure shows that the dominant frequencies of the response spectra become longer with decreasing the PGA's, indicating the effect of the non-linear site amplification suggested by Midorikawa et al. (2011). The fundamental frequencies of the linear amplification of soil can be identified from the ground motion response spectra at frequencies of 4Hz and 10Hz.

5.2.2 Aftershock observation:

Temporary aftershock observation was conducted by Yamanaka et al. (2012), around the MYG004 to determine the spatial variation in the ground motion features. Since the MYG004 station is located on a small cliff with a relative elevation of about 5 meters, two stations at a distance less than 30 meters from the strong motion station were placed. Positions of these sites including MYG004 are illustrated by open circles at the bottom and the top of the cliff in Figure 5.2a, labeled as 'Temp.1' and 'Temp.2'. Each station is made of a three-component accelerometer and a data logger. Ground acceleration was continuously recorded by the data logger throughout the observational period.

Aftershock data were recorded during three days in April, 2011. The high activity of aftershocks occurrence allowed obtaining sufficient data in spite of the short duration of the observation. An example of the observed ground motions at the temporary aftershock stations 'Temp.1' and 'Temp.2' are displayed in Figure 5.3b. Accelerations were filtered in a period range from 0.1 to 5 second. Amplitudes at the top of the cliff (Temp.2) are significantly larger than those at the bottom of the cliff (Temp.1), in spite of the small distances between the two stations.

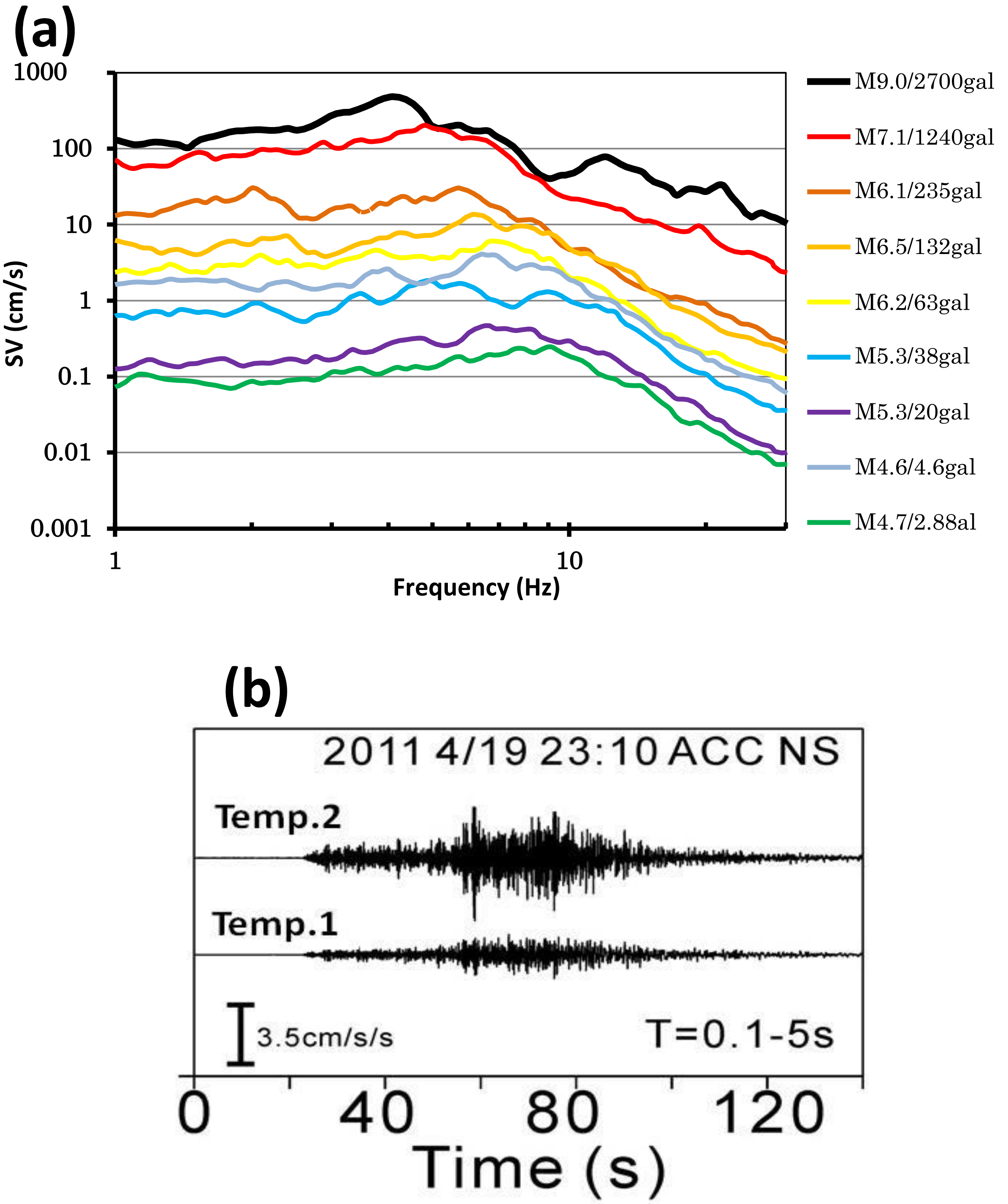

Figure 5.3: (a) Response spectra for ground motion in east-west direction during the main shock and aftershocks of the 2011 Earthquake off the Pacific Coast of Tohoku at MYG004. (b) Ground accelerations in north-south direction, obtained at the temporary aftershock observation sites during an after (Apr.19,2011,23:10) with a magnitude of 5.0 and a depth of 45km. (Yamanaka et al., 2012)

5.2.3 Microtremor exploration:

In order to provide details of the soil structure near the strong motion station MYG004, Yamanaka et al. (2012) conducted a microtremor array observation at the base and the top of the cliff where the station was built. Figure 5.2a is a schematic map of the area of interest. The locations of the microtremor array observation sites and the strong motion station MYG004 are indicated by large triangles as sites 1 and 2, and a small square as site 3.

The inverted S-wave velocity profiles from the microtremor measurements by Yamanaka et al. (2012) are compared in Figure 5.2b. The profiles show significant differences despite the proximity of the measurement sites: they are located within only 20 m of each other. The borehole data from the K-NET Tsukidate MYG004 in a solid black line show a three-layer soil model with a very thin surface layer while the microtremor's S-wave velocity profiles have a very different configuration of four layers.

This comparison also revealed a difference between the profiles obtained at the base and the top of the cliff in dashed and dotted lines respectively. Another dense microtremor H/V exploration was carried out at the top and the base of the cliff between the strong motion station MYG004 and the microtremor array site 1 by deploying 3 components measurements at single site (Yamanaka et al. 2012). The H/V sites considered in our study are located along the area of interest and plotted with solid black dots from T1 to T10 in Figure 5.2a. The H/V spectral ratio results at these sites will be discussed further in this chapter.

5.3 Waveform inversion of the seismic refraction data:

5.3.1 Seismic refraction survey:

We conducted a seismic refraction survey at the top of the cliff, near the microtremor measurement at site 1 and across the microtremor H/V observation points. As the exact position of MYG004 was occupied by trees and dense vegetation, it was almost impossible to perform a seismic survey very close to the strong motion station. We selected the closest accessible area to MYG004 and set up a seismic survey line of 14 m, indicated by the gray line AB in Figure 5.2a. A total of 14 vertical geophones with a natural frequency of 4.5 Hz laid out 1m apart recorded the vertical component of the seismic waves generated by sledge hammer blows at both ends of the survey line. For polarity distinction we will call the offset of our survey line at 0 m ‘side A’, and its tail at 14 m as ‘side B’. Ten impacts were generated at both ends of the survey line using a 5 kg hammer and the impact points were very close to the first station of our survey line. An auto triggering system allowed the waves to be acquired after the detection of the first motion from the nearest station to the source. Shots at each side were stacked and used for inversion.

5.3.2 Microtremor array survey:

Two small microtremor array measurements were conducted along the seismic survey line at the same position as the H/V microtremor points T5 and T7, indicated by small triangles in Figure 5.2a. These small arrays helped to provide more details on the shallow soil along the area of investigation, and could be used to compare our two dimensional inverted model. The small array was 3 m long for the large triangles and 1.5 m long for the small triangles. Seven instruments were arranged in equilateral segments for each triangle. The instruments used in our survey as well as the processing of the microtremor array data were the same as those used by Rhommel and Yamanaka (2012).

5.4 Numerical model and data Inversion:

For our 2D inversion, we referred to the one-dimensional S-wave velocity profile obtained near the seismic survey line AB at the top of the cliff, using the microtremor array explorations by Yamanaka et al. (2012). This profile would allow the determination of the number of layers to be considered for inversion and fix the velocity and depth search limits of each layer. Since we were interested in the 2D structure of the shallow layers, we attempted to retrieve the first two layers down to a depth of 10 m and fix the velocity of the third bottom layer to 330 m/s, in accordance with profile 01 of Figure 5.2b.

Although finite difference numerical grids of 26 m × 15 m with a buffer of 30 grids is generated using a grid meshing of 0.1 m, to invert the two-dimensional soil, only 14 m covered by the seismic survey line were considered, using 14 blocks and 14 depth parameters. Since we did not have complete information of the physical parameters of the soil, we assumed the P-wave velocities and the layer densities in advance. We chose reasonable Vp by multiplying the values of the inverted Vs by 1.7 for layers to be inverted and 2.0 for the third layer. We assume pure elastic and linear wave propagation, where absolute amplitudes of the waveforms were out of our consideration in this inversion. Detailed physical parameters as well as inversion parameters are summarized in Table 5.1. A point source Ricker wavelet with a central frequency of 50 Hz excited the medium near the surface to simulate the plank hammering at distances of 0 m and 14 m in our numerical model, and the vertical impact generated the elastic waves propagating in the numerical soil model.

Source deconvolution was applied to the acquired stacked waveforms in Figure 5.4a, and 5.4b, with a filtering rang of 10Hz-75Hz. The deconvolved waveforms with respect to the station nearest to the shot can be seen in Figure 5.4a' and 5.4b'.

Ten inversions with different random numbers were carried out using both deconvolved waveforms at both sides of the survey line simultaneously.

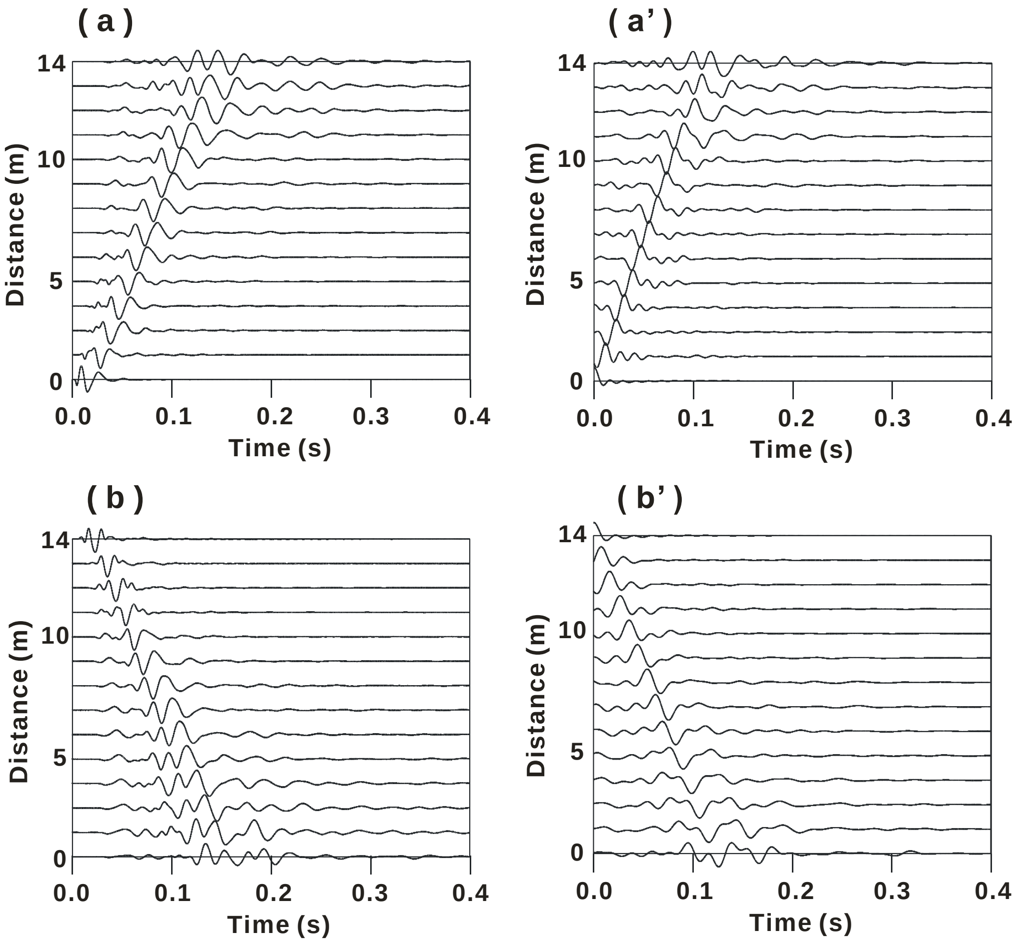

Figure 5.4: Waveforms of the seismic acquisition
(a) Stack waveforms obtained at 0m. (b) Stack waveforms obtained at 14m.
(a') Deconvolved waveforms obtained at 0m. (b') Deconvolved waveforms obtained at 14m.

Table 5.1 Physical proprieties of the soil and settings for acquired data inversion.

Layer	Inversion search limits		Assumed density *(kg/m^3)*	Assumed Vp/Vs	Inversion parameters
	VS (m/s)	*Depth (m)*			
1	100-200	2-6	1700	1.7	Genaration = 100 Population = 20 Mutation rate = 0.01 Crossover rate = 0.7 Initial temp. = 100
2	200-400	7-12	1800	1.7	
3	330 (fixed)	-	1900	2.0	

Inversion results of the seismic data are summarized in Figure 5.5. The target waveforms by solid black lines and the inverted waveforms in dashed lines for both sides of the survey line in Figures 5.5a and 5.5b show the main arrivals at each station fitting acceptably, resulting in a good waveform inversion. The information on the soil structure and shear wave velocity of the surface layer encrypted in the signal were then well reproduced through the inversion process. The final averaged model from the 10 inversions in Figure 5.5c represents the two-dimensional structure beneath the seismic survey line. The locations of the two shots are indicated with black stars at 0m and 14m. The 2D inverted soil profile shows that the shallow structure is quite similar to the one-dimensional soil profile obtained at site 1 in Figure 5.2a, where the layer interfaces are at depths of 4 m and 10 m. However, the top layer clearly reveals a lateral velocity gradient from higher velocity between distances of 0 m to 6 m to lower velocities beyond 6 m.

The block velocity standard deviation from 10 inversions is illustrated in Figure 5.6. This figure show high values of BSD at the surface layer, and low values of BSD at the second layer which means that the inverted model was more accurate to retrieve the second layer than the surface layer. These differences in inversion accuracy can be explained by the velocity inhomogeneity of the surface layer compared to the second layer.

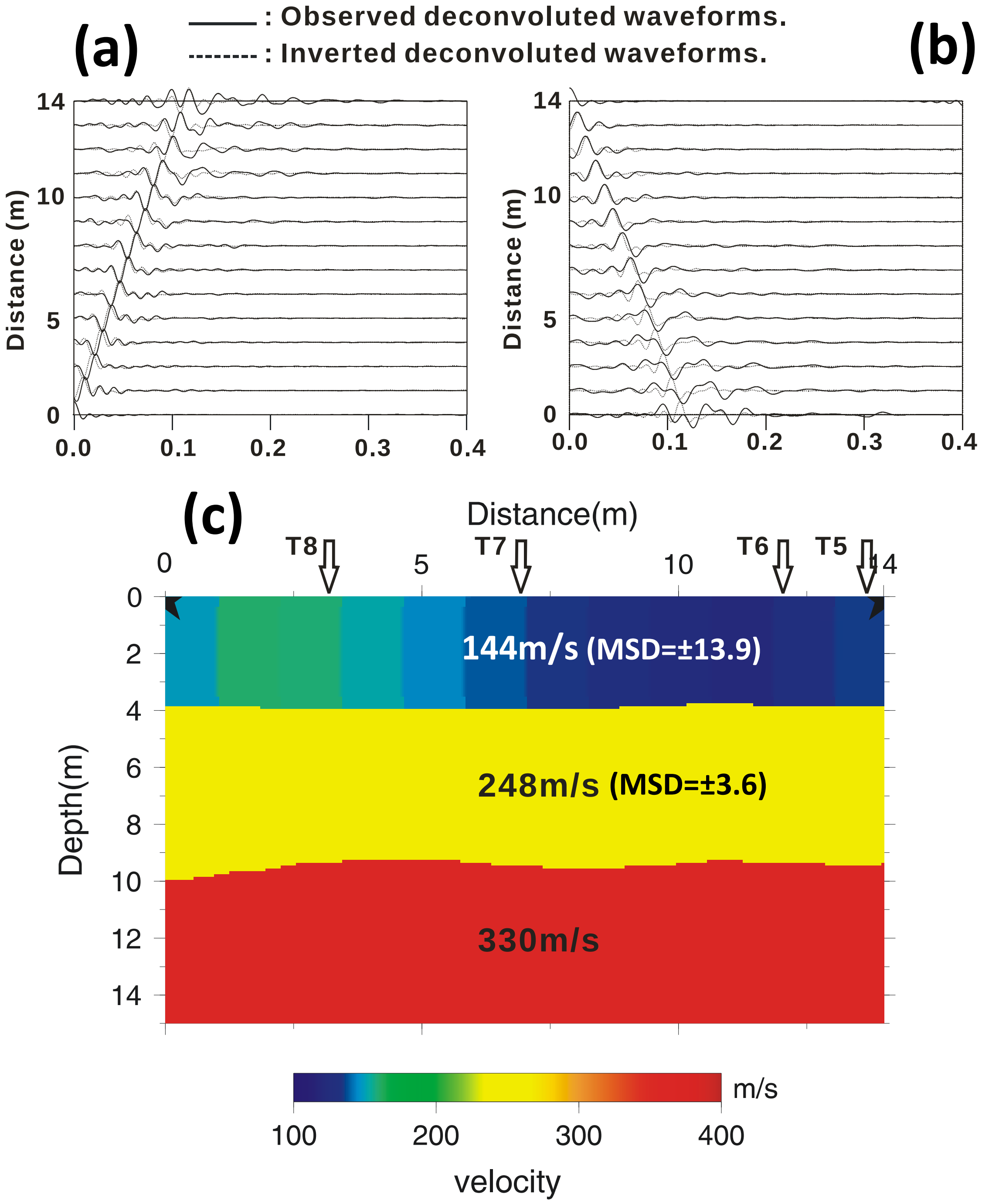

Figure 5.5: Results of the seismic data inversion

(a) Comparison of the observed waveforms (solid black lines) and the inverted waveforms (dotted lines) for the 0m shot.

(b) Comparison of the observed waveforms (solid black lines) and the inverted waveforms (dotted lines) for the 14m shot.

(c) Averaged soil model from 10 inversions.

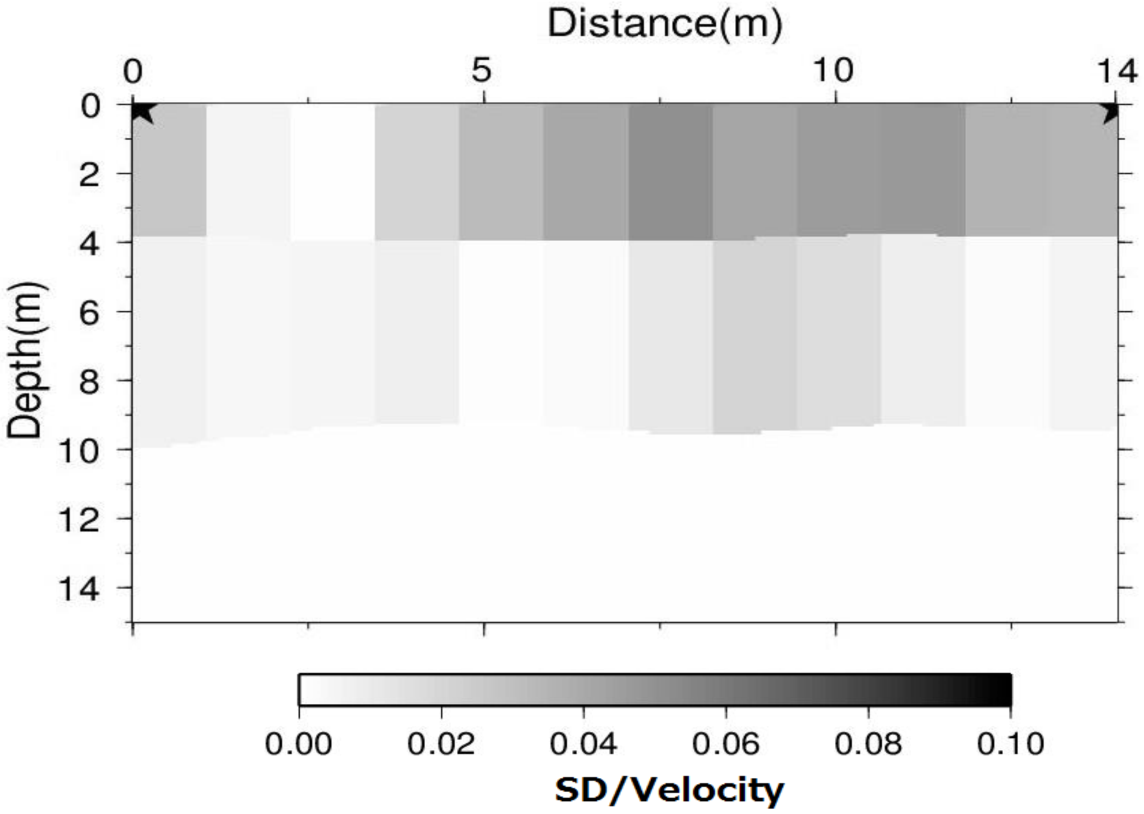

Figure 5.6: Block standard deviation (BSD) for inverted velocities in the averaged model.

5.4.1 Comparison to microtremor results:

To check the reliability of the two-dimensional soil model obtained through the waveform inversion, we correlated the 2D soil profile with the microtremor results conducted along the survey line. Four H/V microtremor stations at locations 3m (T8), 7m (T7), 12m (T6), and 14m (T5) from the shot at side A, as well as the two small microtemor arrays at T5 and T7, were compared to our two-dimensional profile in Figure 5.7d.

Figures 5.7a and 5.7b present the H/V spectral ratios of microtremors observed in the area from T1 to T10 (Yamanaka et al. 2012). All of the H/Vs have a common feature of a peak period at frequency of 5-6 Hz, and they have a similar spectral shape up to 10 Hz. However, additional spectral features are identified by peaks at periods of about 12-15 Hz at sites T1 to T6, located in the northen part of the strong motion station MYG004. Such peaks cannot be found in H/Vs at sites T7 to T10 in the southern part of our seismic survey line. This indicates the possibility of an important lateral variation in the S-wave velocity of shallow layers around MYG004.

The H/V stations located along our seismic survey line, from T5 to T8 in Figure 5.7b, also show different spectral ratio shapes in the high frequency content, from 10 Hz up to 30 Hz. In fact, sites T5 and T6, located at 12 m and 14 m where the surface layer velocity is 130 m/s, have a small peak at 15 Hz. However, station T8, located at 3 m and with a surface velocity of 160 m/s, and station T7 located in the velocity transition area, show a small trough at 15 Hz. This difference at the high frequencies can be explained by the difference in velocity impedance ratios generated between the first layer with inhomogeneous velocity and the second layer with constant velocity.

We applied the SPAC (Spatial Auto-Correlation) method to the small array data to retrieve the Rayleigh waves phase velocity dispersion curve. The 1D S-wave velocity models were then derived by inverting the fundamental mode of the dispersion curve using the hybrid heuristic search inversion of Yamanaka (2007). Details of this process can be seen in the work of Rhommel and Yamanaka (2011). Conditions similar to those in Yamanaka et al. (2012) data processing and the inversion of the phase velocity were assumed.

The Rayleigh wave dispersion curves obtained at T5 and T7 from the small microtremor array measurements are compared in Figure 5.7c. The dispersion curves show clear differences in the phase velocities at higher frequencies (from 20 Hz to 30 Hz), indicating the wave velocity differences between sites T7 and T5 in the shallow layer. The 1D profiles obtained through the inversion of the dispersion curves at sites T7 and T5 are indicated with a solid black line and a dashed black line, respectively in Figure 5.7d. The two profiles show the velocity difference of the first layer, from a low velocity of 136m/s at T5 to a high velocity of 157 m/s at T7.

These 1D S-wave models were then compared with the profiles sampled from our 2D inverted soil at the same locations of T7 and T5. The profiles sampled from the 2D soil model at T7 and T5, are plotted with a grey solid line and grey dashed line, respectively, in Figure 5.7d. Both profiles in 1D and 2D show a layer depth of 4 m for the surface layer. An observation similar to the 1D profile can be pointed out concerning the lateral velocity change in the surface layer, with a decrease in velocity between T7 and T5 in the 2D model. Comparing these 1D and 2D models at T7 and T5, we can confirm the existence of a lateral variation of the shear wave velocity within the surface layer from a high velocity area at T7 to a lower velocity area at T5.

We also calculated the theoretical Rayleigh wave ellipticity from the 1D profiles of Figure 5.7d including higher mode, and plotted results in Figure 5.7e. Theoretical Ralyleigh waves shows similar peaks to the H/V spectra at T7 and T5, with different ellepticity shape between the 1D and 2D models.

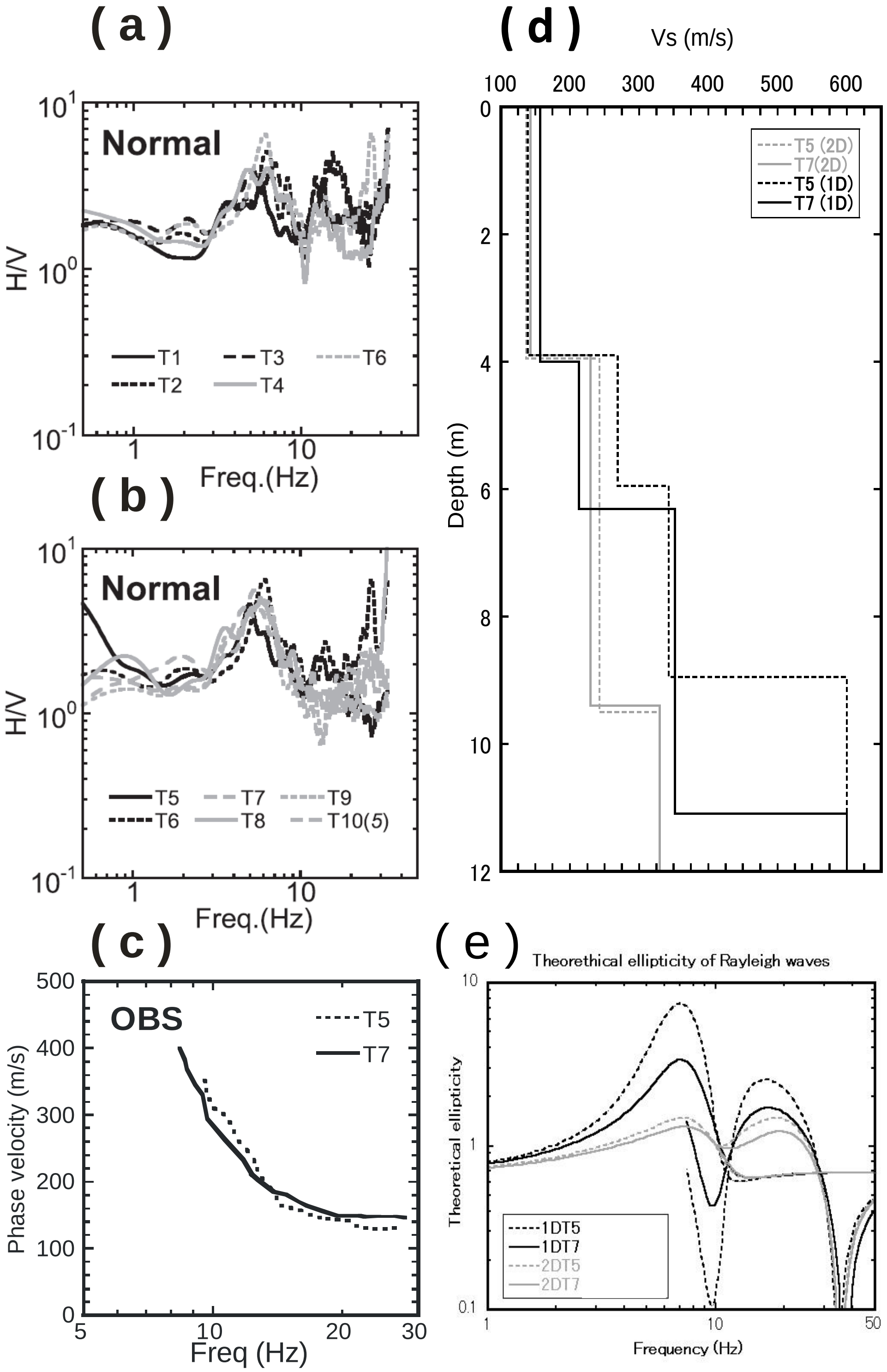

Figure 5.7: Microtremor analysis results along the seismic line.
(a), (b): H/V spectral ratio of microtremors observed at sites T1 to T10 (Yamanaka et al.2012).
(c): Rayleigh wave phase velocity dispersion curves observed at sites T5 and T7.
(d): Comparison of the 1D soil profiles inverted from phase velocity at T5 and T7 in black lines, and soil profiles sampled from the 2D inverted model in gray lines.
(e): Theoretical ellipticity at T5 and T7 for 1D and 2D soil models.

5.4.2 Comparison of the recorded waveforms with other soil profiles:

As shown in Figure 5.2b, our site of interest has very complex structures within a small perimeter. Three different soil configurations co-exist in the area between the strong motion station, the top, and the base of the cliff. The close geophysical exploration at the top of the cliff revealed a lateral velocity variation within the surface layer.

To compare each soil profile obtained in the area with the inverted soil model and determine the most adequate model to fit our seismic waveforms, we conducted 2D numerical simulations using the 1D soil profiles obtained by the microtremor array measurement at the bottom of the cliff, and the soil model provided by the Tsukidate strong motion stationMYG004, respectively, at sites 2 and 3 of Figure 5.2a.

Two numerical forward simulations of the profiles 2 and 3 from Figure 5.2b were performed using the same 2D finite difference grid for the P-SV waves utilized in our inversion program. The 2D structure was made by assuming a lateral extension of each 1D soil profile, with flat interfaces and constant velocities for each layer. 14 receivers recorded the vertical component of the surface waves generated by a point source shot of Ricker waveletwith a central frequency of 50 Hz near the surface, and both observed and simulated waveforms had the source deconvolution described previously.

The calculated waveforms from each simulation are compared to the seismic observed waveforms in Figure 5.8. The comparison between the observed waveforms in solid black lines and the simulated waveforms from the bottom cliff profile in small dashed lines in Figure 5.8a shows less compatibility than that of the profile obtained from the inversion in Figure 5.5c. This incompatibility reflects the difference in S-wave velocities observed between the top and bottom of the cliff.

The simulated waveforms of the borehole profile obtained at MYG004, indicated by large dashed lines in Figure 5.8b, show completely different waveforms from the observed ones in solid black lines, despite the borehole's location at the top of the cliff and its proximity to the survey line.

This significant differences in waveforms can be explained to a large extent by an important geological abnormality between the strong motion station and the investigated site, or by the inappropriateness of the soil profile provided by the K-NET MYG004 station.

Considering these experiments, we concluded that the 2D inverted soil model in Figure 5.5c had the most appropriate fit to the observed waveforms of the soil models in the area, it can be considered the best model to represent the geological structure at the top of the cliff, rather than the borehole profile at MYG004.

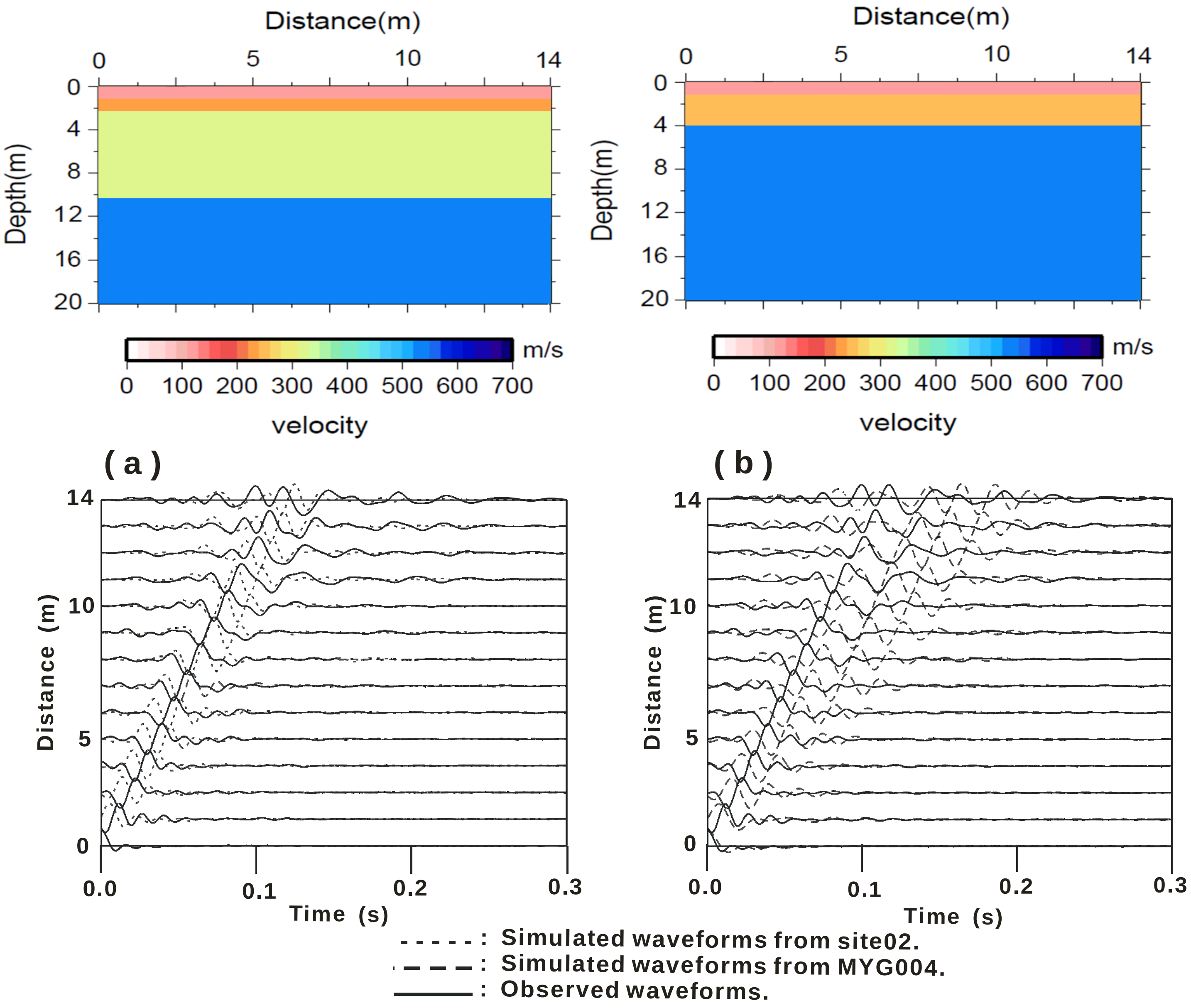

Figure 5.8: 2D simulation results with their input soil models.

(a) Comparison between the observed waveforms in solid black lines, and the simulated waveforms from the downhill profile in dotted lines.

(b) Comparison between the observed waveforms in solid black lines, and the simulated waveforms from MYG004 borehole profile in dotted lines.

5.5 Two-dimensional dynamic ground response:

5.5.1 Inverted model simulation:

Through the microtremor explorations and the seismic waveform inversion, we identified the spatial variation of the shear wave velocity in the surface layer suggested by Yamanaka et al (2012). According to the same authors, this velocity variation could be responsible for the difference in amplification between the strong motion station MYG004 and our investigated area. Satoh (2013), emphasized the fact that any amplification related to the local geology of the cliff effect would appear in the higher frequency content. Here, we try to investigate these assumptions and assess the effect of lateral velocity variation on the local site amplification with regard to the very high amplifications observed at MYG004 during the 2011 Earthquake off the Pacific Coast of Tohoku.

In order to determine the 2D ground response including that of the surface layer with heterogeneous velocity, we conducted a numerical simulation of earthquake ground motion in the soil obtained from our waveform inversion. The 2D soil structure in Figure 5.5c is modeled with a finite difference grid to simulate our numerical soil model in vertical incidence of SH wave field. In this experiment, the third layer of the soil extended down to a depth of 30m, illustrated in Figure 5.9a. Assumed constant Q-values are defined as one-fifth of the shear wave velocity at each layer, similar to Q-values in Yamanaka et al. (2012). Synthetic white noise was generated in the frequency domain and filtered up to 50 Hz (Figure 5.9b). This noise was then converted to the time domain and used as input. The white noise was diffused in our soil through a vertical plane wave incidence at depth of 20m, simulating an upward wave that travels vertically in the 2D soil parallel to the surface for 10 seconds and sweeps the two-dimensional soil structure from the bottom to the top.

Receivers record the ground motion generated by the noise excitation along the surface, as shown in Figure 5.9c. The recorded signal containing the two-dimensional amplification is then used to estimate the transfer function.

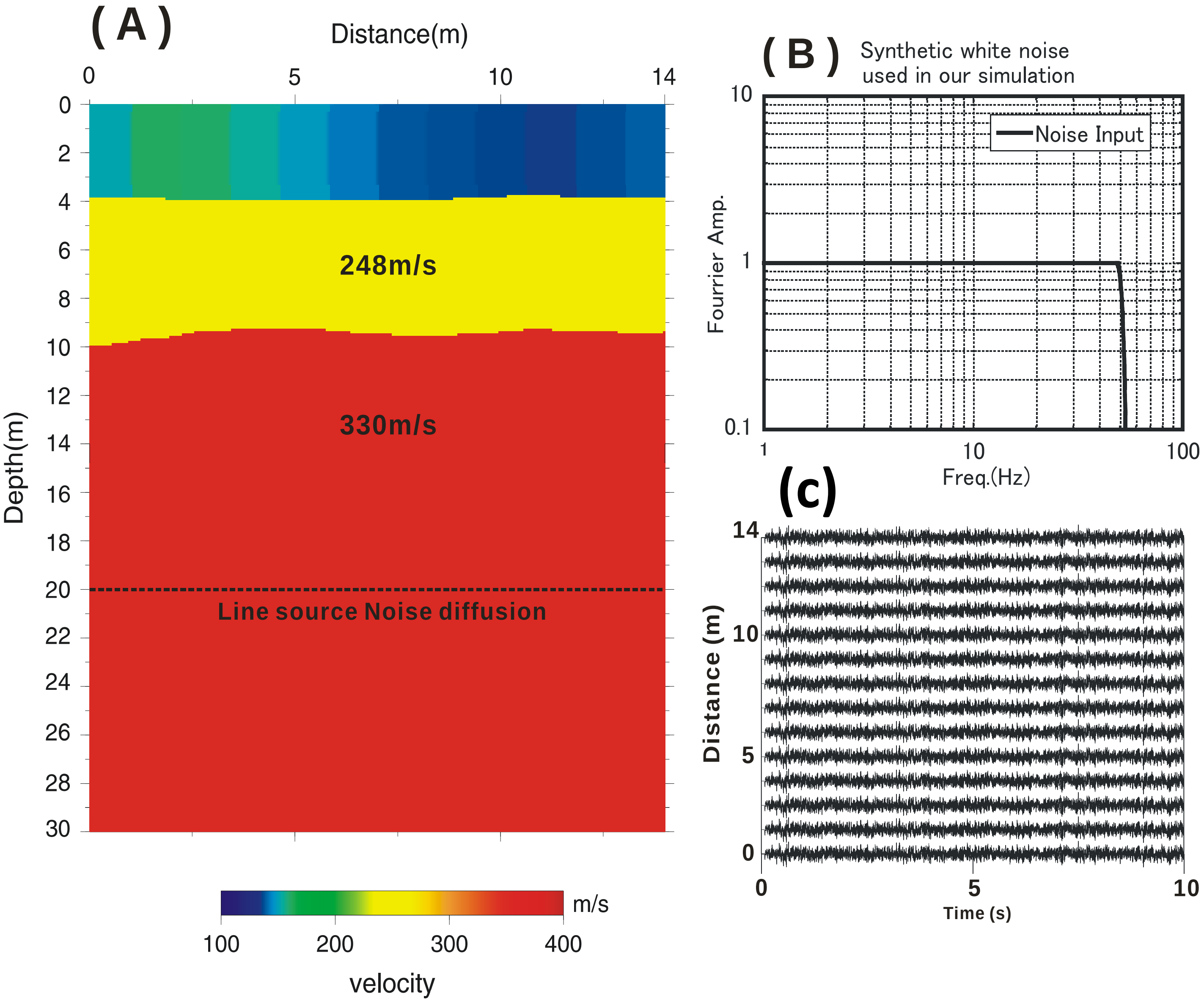

Figure 5.9: Two dimensional ground response analysis:

(a) Numerical simulation configuration.

(b) Synthetic white noise generated in the frequency domain.

(c) Noise signal recorded at the soil surface.

The transfer function is a mathematical representation in term of spatial or temporal frequency of the relation between the input and output of a geological systems, the 2D transfer function is calculated through a division in the frequency of the recorded signal at the free-surface by the input motion spectra of the half space. Since the K-NET strong motion station has an observation range limited to a frequency of 30 Hz (Fujiwara et al. 2004), we will limit our discussion to frequencies not higher than 30 Hz.

Figure 5.10a shows a comparison of the transfer function obtained in the high velocity area of our profile located at a distance of 2 m with a red solid line, and the transfer function of the low velocity area at a distance of 10 m with a blue solid line. Spectral ratio between the high and the low velocity zones shows similar features between 2 m and 10 m. A fundamental peak appears at 6 Hz with an amplification factor of 3. Another more significant peak appears at 20 Hz with an amplification factor of 5.

A difference between 2 m and 10 m can be seen on the small secondary peaks of the spectral ratios, where the high velocity zone has secondary peaks at 9 Hz and 12 Hz, and the low velocity zone shows more secondary spikes at 8Hz, 10Hz, 15Hz and 22Hz.

To evaluate the difference between the two-dimensional transfer function and the one-dimensional theoretical amplification, we calculated the theoretical amplification factors at the sites with different velocities in our 1D soil profiles, just beneath the locations at distances of 2 m and 10m. We assumed constant Q-values similar to those of Yamanaka et al. (2012), one-fifth of the inverted S-wave velocities for each calculation.

Figure 5.10b compares between the 2D transfer function of the high velocity area at 2 m, to the one-dimensional theoretical amplification factor calculated at the same location. The 1D amplification at 2 m has a dominant peak at a frequency of 6 Hz; other higher mode peak frequencies are identified at 15 Hz and 25 Hz. Comparing the 2D transfer function and the 1D amplification factor at 2m, we understand that the 2D simulation reveals more important amplifications than the 1D amplification. The peak at 6 Hz is amplified 2 times. The higher mode peaks at 15 Hz and 25 Hz of the 1D amplification disappear in the 2D simulation, becoming a common peak at 20 Hz with more signification amplification of factor 5.

The 1D amplification factor of the low velocity area at 10 m distance is compared to the 2D transfer function of the same location at Figure 5.10c. The 1D calculated amplification in a gray line shows a peak at 6 Hz, and a more significant peak of factor 3 at 23 Hz. The comparison to the two dimensional simulation shows a similar spectral feature, with more amplification in the 2D simulation of peaks at 6 Hz and 20 Hz, with the second peak shifting slightly to 20 Hz.

The results of this numerical experiment confirm the assumptions proposed by Yamanaka et al. (2012) and Satoh (2013) concerning the potential amplification of the high frequencies by the surface layers. Since these amplifications occur within the location of the K-NET strong motion station in a frequency range lower than 30 Hz, they may contribute to the amplification of the aftershocks recorded by the temporary strong motion station installed in the area.

If we assume that the soil structure beneath the strong motion station MYG004 is similar to the soil structure that we inverted along the seismic line AB, we can discuss the 2D and the 1D amplifications at MYG004. By projecting the position of the MYG004 in our survey line AB, the strong motion station will be located at a distance of 8 m, within the low velocity area of the surface layer.

Figure 5.10d compares the amplification factors calculated at the projection of the MYG004 in our 2D profile (8 m distance), shown as a dashed line, to the 2D transfer function obtained at the same position. Similar observation can be pointed out in this experiment, where the 2D simulation amplify at frequencies of 6Hz and 7Hz, and more considerable amplification of the higher frequencies content at 20 Hz. Amplification is of factor 3.5, and the 1D theoretical amplification have a small peak at 25 Hz. These differences show the significant contribution of the two-dimensional effect to the local site amplification and provide evidence of the role of the shallow soils in amplifying the high frequency content at 20 Hz.

If we compare the simulation results to the response spectra recorded during the main shock and aftershocks at MYG004 in Figure 5.3a, we can easily recognize the first peak between 0.1 s and 0.2 s (5 Hz-10 Hz), shifting from lower periods to longer periods with increasing PGA's due to the nonlinear effect. However since our discussion is limited to the linear amplification of soils in the area, further investigations of the nonlinear amplification in the 2D model will be needed for a better understanding of the strong motion behavior.

It is also noteworthy to mention that during the survey some of our sensors were placed nearby houses, and any effect due to building foundations at the high frequency content were neglected.

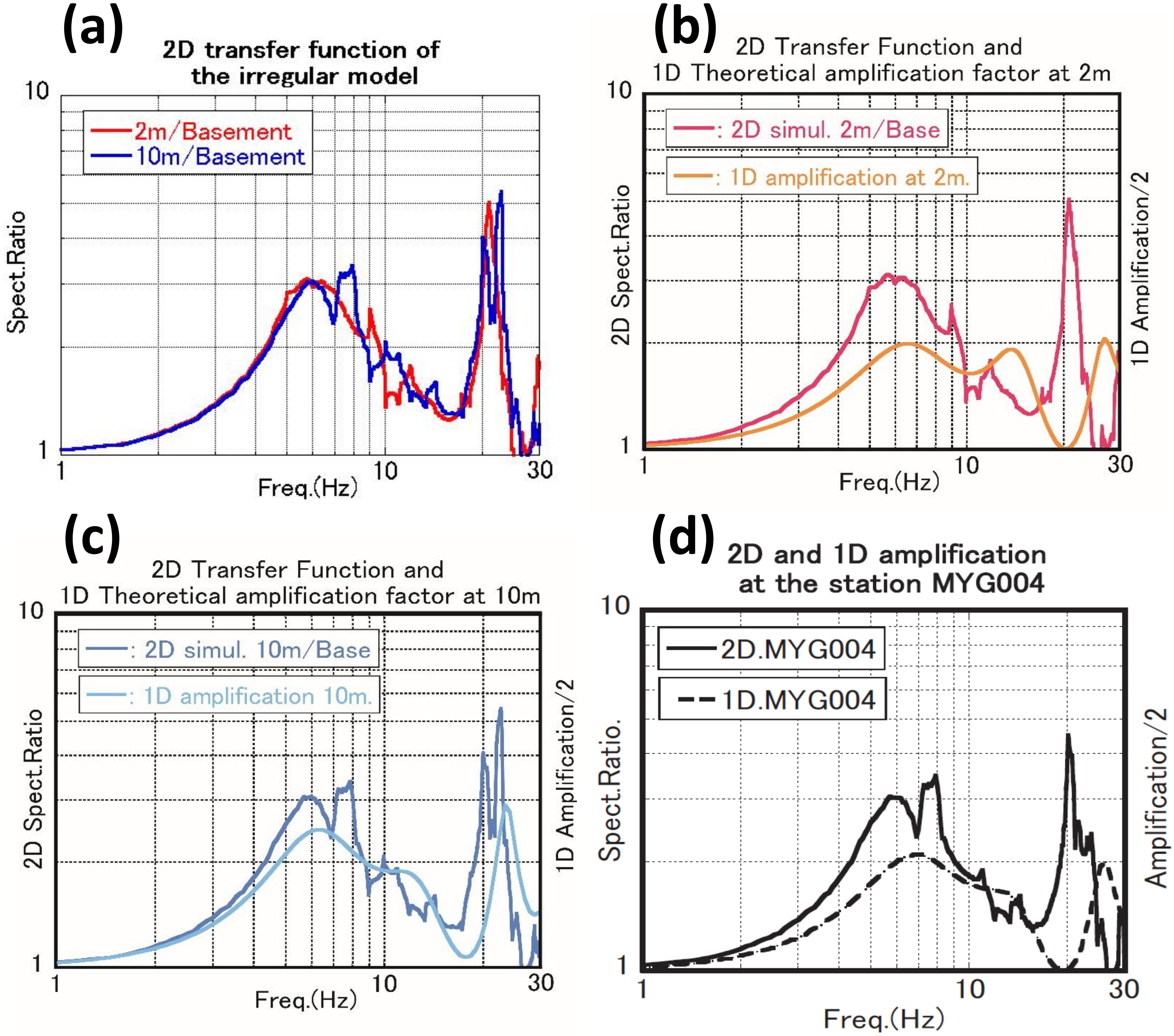

Figure 5.10: Comparison of the 2D and 1D amplification analysis between the high velocity zone at 2m and the low velocity zone at 10m.

(a) 2D transfer function at a distance of 2m in black line and 0m distance in gray line.

(b) 2D transfer function compared to the 1D amplification factor at 2m distance.

(c) 2D transfer function compared to the 1D amplification factor at 10m distance.

(d) Comparison of the assumed 2D to the theoretical 1D amplification at the projection of the strong motion station MYG004 in the 2D inverted soil model.

5.5.2 Effects of the cliff on simulation:

To provide better understanding about the 2D cliff effect on wave propagation, we conducted similar simulation using SH wavefield, where we included irregular free surface effects as a cliff edge as illustrated in Figure 5.11a. We assumed a 30m length model, including our inverted 2D soil with lateral velocity contrast at the first layer, and the cliff edge at a distance of 15m. We input a line source at 20m depth using a plane wave (Ricker wavelet type) with a central frequency of 25Hz, and record the waveforms at the free surface of the model.

The observed waveforms are illustrated in Figure 5.11b. The recordings show three main arrivals along the 2D profile, that we can distinguish major phases chronologically as '1', '2' and '3' in the same figure. The stations located at the bottom of the cliff recorded the first direct arrival phase at around 0.1s designated as '1', and then the stations at the top of the cliff recorded the wave arrival with a slight delay in '2', the amplification from 1 to 2 can be explained by the velocity contrast between the second layer and surface layer. These stations at the top also recorded a third significant wave distinguished as '3' that do not appears in the recordings at the bottom of the cliff. This third arrival underlines the topography effect of the cliff edge on the 2D wave propagation. In fact, the cliff edge scatters the up going wave generating another significant wave that propagates at the inner side of the cliff as Love wave.

To show the difference between the top and the bottom of the cliff, we compared the recordings of three stations at different locations along the soil profile. Two stations at the top of the cliff, in the high velocity zone at 5m distance and the low velocity zone at 10m distance, while the third station is located at the bottom of the cliff at 20m distance. The comparison of the recordings is illustrated in Figure 5.11c, where stations are designated with distinct colors.

The amplitude of the scattered wave ‘3’ appears to be more significant in the low velocity area (station 10), than the high velocity area (station 5), indicating that the low velocity amplifies even more the scatterings from the cliff.

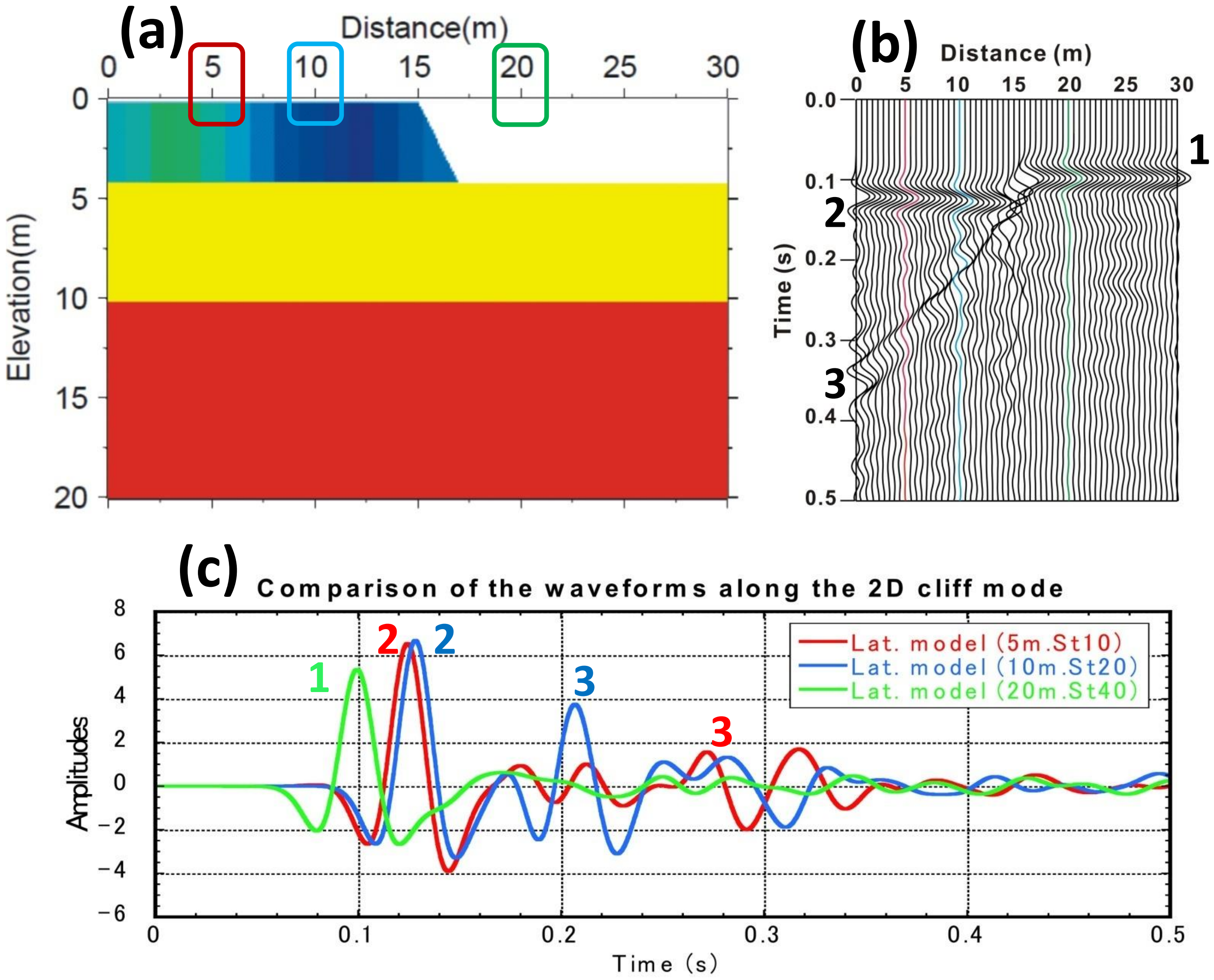

Figure 5.11: Two dimensional wave propagation of the cliff model.

(a) Cliff model used for simulation.

(b) Recorded waveforms along the irregular free surface.

(c) Comparison of the recorded waveforms at different distances.

To underline the effects of the cliff together with the lateral velocity variation, we calculated the 2D transfer function of the soil model at Figure 5.11a. The transfer function is calculated by division in the frequency of the recorded signal on the surface at distance of 10m, and compared it with transfer function

The comparison between the flat model transfer function, and the cliff model transfer function is illustrated in Figure 5.12. The transfer function including the cliff effects shows higher amplification and similar spectral shape to the flat surface model. However, the peaks at 6Hz and frequencies between 10Hz and 15Hz are more amplified with the existence of the cliff at the surface. These results show tha t the presence of irregular cliff at the surface enhance the amplification of some frequencies better than the flat surface model.

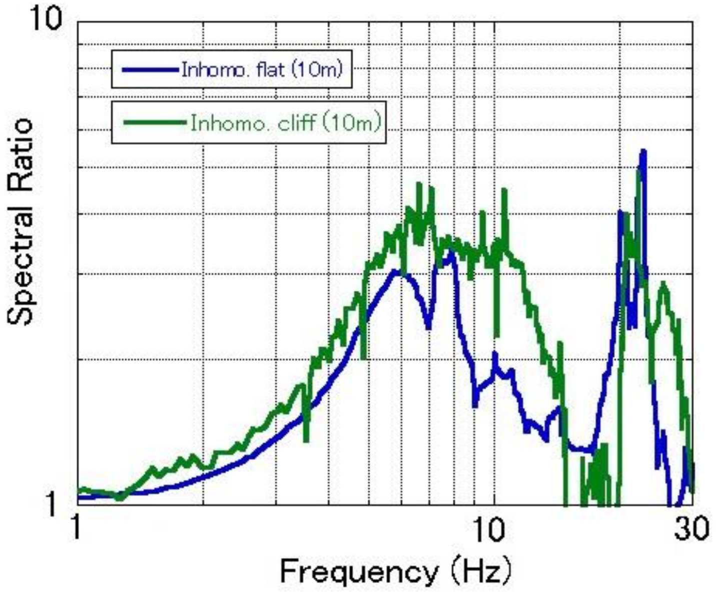

Figure 5.12: Comparison of the 2D transfer functions at 10m of the inhomogeneous velocity model with a flat surface, and the model including a cliff.

5.6 Contribution toward understanding strong motion at MYG004:

We demonstrated in the previous experiments that the lateral velocity variation combined with the surface cliff irregularity can play significant role at the local site amplification, and succeeded to quantify their frequencies of occurrence at the high frequencies content.

In Figure 5.3a, the response spectra of the ground motion during the main shock (M9.0/2700Gal) has a fundamental peak of 4Hz, while the aftershock have a fundamental peak at 5Hz. As reported earlier, this tilt of the fundamental peak from stronger to weaker motions was explained by the non-linearity behavior of the soil. In addition to the fundamental peak at 4Hz, the main shock shows two distinguishable peaks at 12Hz and 21Hz.

When we compare the 2D transfer function including the cliff with the main shock response spectra, we can correlate the high frequency peak at 21Hz of the response spectra with the high frequency peaks of the transfer function simulated from 2D inhomogeneous model with a cliff at 20Hz. These high frequency peaks can be interpreted as the 2D signature of the topography and velocity inhomogeneity in the waveforms recorded during the 2011 Tohoku earthquake.

Chapter 7

CONCLUSION

We have proposed an alternative method for two-dimensional shallow soil explorations based on inversion of waveforms acquired by conventional seismic refraction survey. This method allows the estimation of a two-dimensional S-wave profile of layered soils through a numerical soil reconstruction using a 2.5D finite difference computation to fit the observed waveforms through a heuristic inversion. In the method we included pre-processing of deconvolution for both the observed and the calculated data to eliminate the source signature from the waveforms. Numerical experiments were carried out to test the performance of our method to invert soil configurations which may be difficult to retrieve with conventional near surface methods. A two-layers model with an irregular interface was inverted successfully, and through this experiment we had proven the accuracy of our method in properly inverting a two-dimensional soil model with an irregular interface using recordings from a single shot. We also inverted a soil model with strong lateral velocity change and a soil model with blind layer in a noisy environment. Despite the complexity of the model and the noise perturbation, the inversion of a single shot data was able to reconstruct the 2D structure of the soil.

We also demonstrated the applicability of our technique to real data. The inversion of the field acquired data allowed us to retrieve the 2D shallow soil profile recorded from two shots of a survey line of 30 meters. The inverted model underlined a lateral velocity gradient in the second layer of the soil of several meters. Correlation of the inverted soil with an existing borehole profile showed acceptable agreement of the inverted soil structure to a depth of 8m, where improvements were carried out for construction purposes after the borehole drill.

We even succeeded to discuss a real earthquake engineering problem using our method, and successfully retrieved the 2D soil structure at the vicinity of the Tsukidate strong motion station MYG004, where abnormal amplifications were reported during the 2011 Earthquake off the Pacific Coast of Tohoku using our inversion method. We demonstrated the 2D effect of surface layer on the local site amplification, quantified the frequency of occurrences through numerical experiments, and showed that inhomogeneous shallow soils with complex topographies can play significant role on amplifying high frequencies.

The major advantage of our method compared with the other near surface inversion methods is that single shot from small number of data can be sufficient to profile a two-dimensional soil structure to a certain extend. The numerical experiments discussed in our research were all inverted using records from a single shot at no more than 20 receivers were used to obtain satisfactory results even in soil with blind layer. In real data inversion, only 16 stations and two shots were sufficient to invert the two-dimensional soil profile.

Since our method inverts the time series of the seismic waves, it is completely independent from the modal identification of Rayleigh waves. Most of active surface wave methods are based on surface wave phase velocity of the fundamental mode assuming that all the energy is contained in the fundamental mode. However, this assumption can be misleading in case of energy shifts from the fundamental mode to higher modes. Therefore, our inversion requiring no mode identification, can offer an alternative solution to invert soil where surface wave have multi-modal contributions.

Even though this method is successful with the inversion of a 2D shallow soil profile, it requires a priori information about the soil, in order to know the number of layers to be inverted and determine appropriate search limits for velocity and depth parameters. For example, this method should be combined with micro-tremor array exploration to prepare the one-dimensional profile up which we can build our 2D inversion.

The proposed method requires a very rudimentary acquisition setting, utilizing the whole information encrypted in the signal to retrieve the two-dimensional profile of shallow layered soil with free surface. It contains no modal identification of surface waves and a single shot with several geophones can be sufficient to achieve a 2D soil structure to a certain extent. It can be applied for routine geotechnical problems, investigating the effect of shallow soils for earthquake engineering purposes or monitoring soil stability.

This method can be upgraded for more complex soil configuration; ongoing research and further developments aims to improve our method for soils with tunnels, soils with irregular free-surface or soils including non-layered complex geological features. We also need to have many tests of the method by applying to actual data with various kind of geological conditions for geophysical practical use.

We also needs to have many test of the method by applying to actual data with various kinds of geological conditions for geophysical practical use.

REFRENCES.

Alder, D., 1993, Genetic Algorithms and Simulated Annealing: A marriage proposal: proceedings of the IEEE Neural Networks conference, 1104-1109.

Amrouche, M., and H. Yamanaka, 2012, Determination of 2D shallow S wave velocity profile using waveform inversion of P-SV refraction data: Proc. of the 15th World Conference on Earth Engineering-Lisbon, Paper 0231.

Amrouche, M., and H. Yamanaka, 2012, Two dimensional soil profiling using seismic refraction wave inversion: An application to actual data: Proc. Of the 127th conference of the society of exploration geophysicist of japan, pp. 9-12.

Aoi, S., T. Iwata, K. Irikura, 1995, Waveform inversion for determining the boundary shape of the basin structure: Bulletin of the Seismological Society of America,5, 1501-1506.

Bleibinhaus, F., and N.Rondenay, 2009, Effects of surface scattering in full-waveform inversion: Geophysics, 74, no.6, 69-77.

Boiero, D., and L.V. Socco, 2010, Retrieving lateral variations from surface wave dispersion curves: Geophysical Prospecting, 58, 977-996.

Bretaudeau, F., R. Brossier, D. Leparoux, O. Abraham and Virieux, J., 2013, 2D elastic fullwaveform imaging of the near-surface: application to synthetic and physical modelling data sets, Near Surface Geophysics, 11(3), 307–316.

Caserta, A., A. Rovelli, F. Marra, and Belluci, F., 1998, Strong diffraction effects at the edge of the Colfiorito, central Italy, basin: Proceedings of the second international symposium on the effects of surface geology on seismic motion, Yokohama, Balkema, Vol.2, 435-440.

Cerjan, C., D. Kosloff, and M. Reshef, 1985, A nonreflecting boundary condition for discrete acoustic and elastic wave equation: Geophysics, 50, 705-708.

Clayton, R., and B. Enquist, 1977, Absorbing boundary conditions for acoustic and elastic wave equations: Bull. Seis. Soc. Am., 67, 1529-1540.

Field, E.H., 1996, Spectral amplification in a sediment filled valley exhibiting clear basin-edge-induced waves: Bulletin of the Seismological Society of America, 86, 991-1005.

Goto, H., S. Sawada, N. Kobayashi, and Yamada, K., 2009, Characteristics of site response around K-NET Anamizu station, Journal of Japan Society of Civil Engineers, 65, 1-5.

Graves, R.W., 1996, Simulating seismic wave propagation in 3D elastic media using staggered-grid finite differences: Bulletin of Seismological Society of America, 86(4), 1091-110.

Guasch L., M.Warner, T. Nangoo, J. Morgan, A. Umpleby, I. Stekl, N. Shah, 2012, Elastic 3D full-waveform inversion: Proceedings of the SEG Annual Meeting, Las Vegas.

Hagiwara, T. and Omote, S., 1939, Land creep at Mt Tyausu-Yama (Determination of slip plane by seismic prospecting): Tokyo Univ. Earthqauke Res. Inst. Bull., v17, p. 118-137.

Hagedoorn, J. G., 1959, The plus-minus method of interpreting seismic refraction sections: Geophysical prospecting, 7, issue 2, 1529-1540..

Hayakawa, T., M. Oshima, T. Satoh, H. Kawase, S. Matsushima, M. Baoyintu, F. Nagashima, and K. Nakano, 2011, Estimation of surface layer at K-NET Tsukidate using microtremor array observation and site effects: Proc. of the 8th AnnualMeeting of Japan Association for Earthquake Engineering, pp. 444-445 (in Japanese).

Hayakawa, T., T. Satoh, M. Oshima, H. Kawase, S. Matsushima, Baoyintu, F. Nagashima and K. Nakano, 2012, Estimation of the nonlinearity of the structure of the surface soil at Tsukidate during the 2011 off the Pacific coast of Tohoku Earthquake: Proc. of the 15th World Conference on Earth Engineering-Lisbon, Paper 3749, 2012.

Hayashi, K., Taamura, M., Hirade, T., Yu, S., Muraoka, M., and Y. Kikuti, 2007, Site investigation by geophysical exploration and sounding around the K-NET Anamizu observation station: Program and abstracts of the seismological society of Japan, Fall meeting A 12-07, 11.

Fliender, M.M., S. Treitel, and L.M. Gregor, 2012, Full-waveform inversion of seismic data with the neighborhood algorithm: The Leading Edge, 31(5), 570-579.

Franklin, A.G, 1979, Use of shear waves in seismic refraction surveying: Geotechnical laboratpry, U.S. army engineer.

Fujiwara, H., S. Aoi, T. Kunugi, and S.Adachi, 2004, Strong-motion observation networks of NIED: K-NET and KiK-net: Proc. of COSMO workshop on archiving and web dissemination of geotechnical data.

Fukumoto S., T. Unno, N. Sento, R. Uzuoka, M. Kazama, 2007, Estimation of strong ground motions at Tsukidate landslide site during the 2003 Sanriku-Minami earthquake –realization of ground motion waveforms using the data of strong motion seismometers and seismic intensity and its fluidization mechanism using laboratory testing: J. of Japan Association for Earthquake Engineering, 7-2, pp. 160-179.

Irikura, K., and S. Kurahashi, 2011, Strong ground motions during the 2011 Pacific coast off Tohoku, Japan earthquake: Proc. of the International Symposium on Engineering Lessons Learned from the 2011 Great East Japan Earthquake, pp. 9-20.

Jaramillo, J.D., J.D. Gomez, D. Restrepo, and D. Restrepo, 2014, A novel simple procedure to consider seismic soil structure interaction effects in 2D models: Journal of earthquake engineering and engineering vibration, 13, 3, 535-543.

Kallivokas, L.F., A. Fathi, S. Kucukcoban, K.H. Stokoe, J. Bielak, and O. Ghattas, 2013, Site characterization using full waveform inversion: Journal of Soil Dynamics and Earthquake Engineering, 47, 62–82.

Kobayashi, N., H. Goto, K. Yamada and S. Sawada, 2009, Shallow S-wave seismic reflection survey around the K-NET Anamizu site, Safety, Reliability and Risk of Structures, Infrastructures and Engineering Systems, pp.2933-2939.

Levander, A.R., 1988, Fourth-order finite difference P-SV seismograms: Geophysics, 53, 1425-36.

Lee, K.H., and H.J. Kim, 2003, Source-independent full-waveform inversion of seismic data: Geophysics, 68, 2010-2015.

Li, W.D., S.K. Ong and A.Y. Nee (2002), Hybrid genetic algorithm and simulated annealing approach for the optimization of process plans for prismatic parts: Int. J. Production Research, 40, 1899-1922.

Lin, C., and C. Lin, 2007, Effect of lateral heterogeneity on surface wave testing: Numerical simulations and a countermeasure: Soil Dynamics and Earthquake Engineering, 27, 541-552.

Matsushima, S., F. Nagashima, H. Kawase, T. Hayakawa, M. Oshima, T. Satoh, Baoyintu, and K. Nakano, 2011, Aftershock observation of the 2011 off the Pacific Coast of Tohoku earthquake near K-NET Tsukidate: Proc. of the 8th Annual Meeting of Japan Association for Earthquake Engineering, pp. 446-447 (in Japanese).

Midorikawa, S and H. Miura, 2011, K-NET Tsukidate Strong Motion Record and Nearby Damage during the 2011 off the Pacific Coast of Tohoku Earthquake: Summary of Technical papers of Annual meeting of AIJ, B-2, pp. 37-38 (in Japanese).

Motosaka, M., and T. Tsamba, 2011, Investigation of high acceleration records at K-NET Tsukidate station during the 2011 off the Pacific coast Tohoku Earthquake: Proc. of the 8th Annual Meeting of Japan Association for Earthquake Engineering, pp. 24-25 (in Japanese).

Nagashima, F., H. Kawase, S. Matsushima, F.J. Sánchez-Sesma, T. Hayakawa, T. Satoh and M. Oshima, 2012, Application of the H/V spectral ratios for earthquake ground motions and microtremors at K-NET sites in Tohoku region, Japan to delineate soil nonlinearity: Proc. of the 15th World Conference on Earth Engineering-Lisbon, Paper 2190.

National Research Institute for Earth Science and Disaster Prevention, Strong motion seismograph networks K-NET, KiK-net, http://www.kyoshin.bosai.go.jp/kyoshin/ [accessed Feb. 25, 2014].

Narayan, J., 1998, 2.5D numerical simulation of acoustic wave propagation: Pure applied Geophysics,151, 47-61.

Nazaran, S., and K. H. Stokoe, II 1984, In situ shear wave velocity from spectral analysis of surface waves: Proceedings, 8th World Conference on Earthquake Engineering, 3, 31-38.

O'Neil, A., and T. Matsuoka., 2005, Dominant higher surface-wave modes and possible inversion pitfalls: Journal of Environmental and Engineering Geophysics, 10, Issue2, 185-201.

Pan, G. S., R. A. Phinney, and R. I. Odom, 1988, Full-waveform inversion of plane-wave seismograms in stratified acoustic media: Theory and feasibility. Geophysics 53, 21-31.

Palmer,.D., 1980, The generalized reciprocal method of seismic refraction interpretation: Society of Exploration Geophysics 37-39.

Park, C. B., R. D. Miller, and J. Xia, 1999a, Multichannel analysis of surface waves: Geophysics, 64, 800–808.

Park, C. B., R. D. Miller, and J. Xia, 1999b, Multimodal analysis of high frequency surface waves: 12th Symposium on the Application of Geophysics Engineering and Environmental Problems (SAGEEP), 115-122, doi:10.4133/1.2922596.

Pratt, R.G., 1999, Seismic waveform inversion in the frequency domain, Part 1: Theory and verification in a physical scale model: Geophysics, 64, no.3, 888-901.

Razin. A.V., 2010, Scattering of a Rayleigh surface acoustic wave by a small-size inhomogeneity in a solid half-space: Radiophysics and Quantum Electronics, 53, no. 7.

Romdhane, A., G. Grandjeany, R. Brossier, F. Rejiba, S. Operto, and J. Virieux, 2011, Shallow-structure characterization by 2D elastic full-waveform inversion: Geophysics, 76, no.3, 81-93.

Rhommel, G., and H.Yamanaka, 2012, Shallow shear-wave velocity profiles and site response characteristics from microtremor array measurements in Metro Manila, the Philippines: J. of Exploration Geophysics, 43, pp. 255-266.

Sambridge, M., and G.Drijkoningen, 1992, Genetic algorithms in seismic waveform inversion: Geophysical Journal International, 109, 323-342.

Sakai .Y, A. Aoi., K. Arai., and T. Suzuki, 2010, Damage investigation of surroundings of the seismic stations in the 2008 Iwate-Miyagi Nairiku earthquake and correspondence of damage to buildings with strong ground motions: J. of Japan Association for Earthquake Engineering, 10-4, pp. 14-53.

Satoh .T, 2013, Interpretation of the cause of high acceleration ground motions during the 2011 Tohoku earthquake: Proc. of the International Workshop of Japan Association for Earthquake Engineering on the Effects of Surface Geology on Strong Ground Motion, pp. 25-39.

Sears, T.J., S.C. Singh and P.J. Barton, 2008, Elastic full waveform inversion of multi-component OBC seismic data: Geophysical prospecting, 56, 843-862.

Semblat, J.F., A. Kham, E.Parara, P.Y. Bard, K. Pitilakis, K. Makra, and D. Raptakis, 2005, Seismic wave amplification: Basin geometry vs. soil layering: Soil dyamics and earthquake engineering, 25(7-10) Special Iss., 529-538.

Sen, M.K., and P.L. Stoffa., 1991, Nonlinear one-dimensional seismic waveform inversion using simulated annealing: Geophysics, 56, no.10, 1624-1638.

Song Z.-M., P.R. Williamson, and R.G. Pratt, 1995, Frequency domain acoustic-wave modeling and inversion of crosshole data: Part II-Inversion method, synthetic experiments and real-data results: Geophysics, 60, no.3, 796-809.

Sheehan, J.R., et al.,2005, An evaluation of methods and available software for seismic refraction tomography analysis: Journal of Environmental and Engineering Geophysics, 10, Issue1, 21-34.

Shitvelman, V., 2003, Improving the resolution of shallow seismic sections using eigenimage analysis: Near Surface Geophysics, 1, 149-154.

Socco, L.V., S.Foti, and D.Boiero, 2010, Surface wave analysis for building near surface velocity models – Established approaches and new perspectives: Geophysics, 75, no.5, A83–A102.

Socco, L.V., and C. Strobbia, 2004, Surface-wave method for near-surface characterization: a tutorial: Near Surface Geophysics, 2, 165-185.

Strobbia, C., and S.Foti, 2006, Multi-offset phase analysis of surface wave data (MOPA): Journal of applied geophysics, 59, 300-3013.

Takekoshi, M., and H.Yamanaka, 2009, Waveform inversion of shallow seismic refraction data using hybrid heuristic search method: Exploration Geophysics, 40, 99-104.

Tarantola, A., 1984, Inversion of seismic reflection data in the acoustic approximation: Geophysics, 49, 1259-1266.

Thierry, P., S. Operto, and G. Lambre, 1999, Fast 2D ray-Born inversion/migration in complex media: Geophysics, 64, 162-181.

Tran, K. T., and M. McVay, 2012, Site characterization using Gauss-Newton inversion of 2-D full seismic waveform in the time domain, Soil Dyn. Earthq. Eng., 43, 16–24.

Virieux, J.,1986, P-SV wave propagation in heterogeneous media: Velocity-stress finite difference method: Geophysics, 49, 11, 1933-1957.

Virieux, J., and S. Operto, 2009, An overview of full-waveform inversion in exploration geophysics: Geophysics, 74, no.6, 127-152.

Xia, J., R. D. Miller, and C. B. Park, 1999, Estimation of near-surface shear wave velocity by inversion of Rayleighwave: Geophysics, 64, no. 3, 691–700.

Xu, Y., J.Xia and R.D. Miller,2006, Quantitative estimation of minimum offset for multichannel surface-wave survey with actively exciting source: Journal of Applied Geophysics,59, 117-125.

Yamanaka, H. and H. Ishida,1999, Application of Genetic Algorithms to an Inversion of Surface-Wave Dispersion Data: Bulletin of the Seismological Society of America, Vol. 86, no.2, 436-444.

Yamanaka, H., 2005, Comparison of performance of heuristic search methods for phase velocity inversion in shallow surface methods: Journal of Environmental and Engineering Geophysics., 10, 163-173.

Yamanaka, H., 2007. Inversion of surface-wave phase velocity using hybrid heuristic search method:Butsuri-Tansa/Geophysical Exploration,60, 3, 265-275. (In Japanese)

Yamanaka, H. and H. Yamauchi, 2010, Waveform inversion of SH waves in seismic refraction exploration for 2D shallow S-wave velocity profile: numerical experiments and application to actual data. Butsuri-Tansa/Geophysical Exploration, 63, 4, 321-332. (In Japanese)

Yamanaka, H., S. Tsuno, K. Chimoto, N. Yamada, S. Fukumoto, and K. Eto, 2011, Estimation of site amplification from observation of aftershocks of the 2011 off the Pacific Coast of Tohoku earthquake and microtremor explorations in the vicinity of K-NET Tsukidate station, Miyagi prefecture, Japan: Geophysical Exploration (Butsuri Tansa), Vol.64, pp. 389-399 (in Japanese).

Yamanaka, H., K. Chimoto, S. Tsuno, P.Y. Dhakal, M. Amrouche, N. Yamada, S. Fukumoto and K. Eto, 2012, Estimation of S-wave velocity profiles and site amplification around the K-NET Tsukidate station, Miyagi Prefecture, with reference to large PGA during the 2011 off Pacific coast of Tohoku earthquake, Japan," j. of Disaster Research, 7, 6,682-692.

Zhang, J., and Toksöz, M. N., 1998, Nonlinear refraction traveltime tomography: Geophysics 63, 1726-1737.

Zaineh, H.E., H. Yamanaka, R. Dakkak, A. Khalil, M. Daoud,2012, Estimation of Shallow S-Wave Velocity Structure in Damascus City Syria, Using Microtremor Exploration: Journal of Soil Dynamics and Earthquake Engineering, 39, 88–99

Zeng, C., Xia, J., R.D. Miller, G.P. Tsoflias, 2011, Feasibility of waveform inversion of Rayleigh waves for shallow shear-wave velocity using a genetic algorithm: Journal of Applied Geophysics, 75, 648-655.